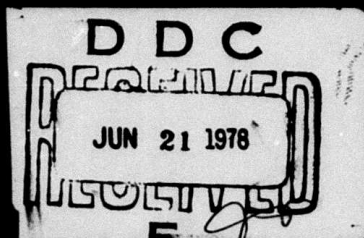
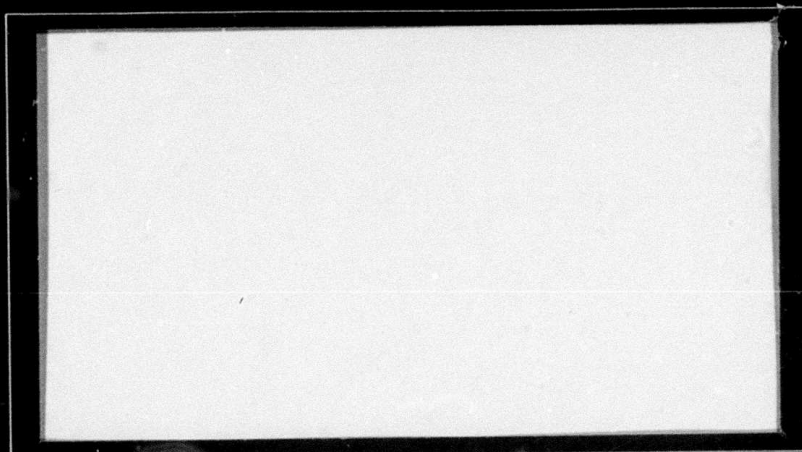


AD A 055485



12



This document has been approved  
for public release and sale; its  
distribution is unlimited.

AD No. \_\_\_\_\_  
DDC FILE COPY

# *Edward L. Ginzton Laboratory*

OF THE

W. W. HANSEN LABORATORIES OF PHYSICS

STANFORD UNIVERSITY · STANFORD, CALIFORNIA 94305



FOR FURTHER TRAN ~~SLIT~~

AD A 055485

AD No. \_\_\_\_\_  
DDC FILE COPY

DDC FOR FURTHER TRAN  
JUN 21 1978  
FAP

12

11

12 175 p.

Apr 1978

6

THE STORAGE CORRELATOR: THEORY AND SIGNAL  
PROCESSING APPLICATIONS

9 Technical Report

Contract No. N00014-76-C-0129

WARPA Order-2778

Order No. 2778-5

Project No. 8D10

10 Peter G. Borden

14 GL-2800

Sponsored by

Advanced Research Projects Agency (DOD)  
ARPA Order No. 2778-5

Monitored by ONR Under Contract No. N00014-76-C-0129

*G. S. Kino*

G. S. Kino  
Principal Investigator

This document has been approved  
for public release and sale; its  
distribution is unlimited.

The views and conclusions contained in this document are those of the author and should not be interpreted as necessarily representing the official policies, either expressed or implied, of the Defense Advanced Research Projects Agency or the U.S. Government.

78 06 15 061

409 640

JOB



SECURITY CLASSIFICATION OF THIS PAGE (When Data Entered)

DD FORM 1473  
1 JAN 73

EDITION OF 1 NOV 65 IS OBSOLETE 11

UNCLASSIFIED

SECURITY CLASSIFICATION OF THIS PAGE (When Data Entered)

UNCLASSIFIED

SECURITY CLASSIFICATION OF THIS PAGE(When Data Entered)

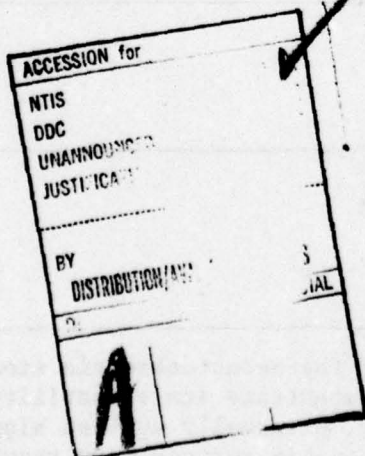
20. (continued)

A number of modes of both storing the charge pattern and reading it have been reported. The theory provides analytic predictions of the device performance for most of these modes of operation and most reported device structures. Experimental confirmation of the theory is given.

Particular attention is paid to the transient characteristics of  $p^+n$  diodes. It is shown both theoretically and experimentally that their response is nearly equivalent to that of fast diodes (e.g., Schottky diodes) in this application. As a consequence, they may be charge quickly (in nanoseconds) and can retain their charge for long times (seconds).

A working device has been demonstrated. Key details of its construction are discussed. Particular attention is paid to methods for reducing spurious signal generation and to an evaluation of alternate diode array structures.

A variety of signal processing results are presented to demonstrate the stored correlator's versatility as a signal processor. Correlations performed with various phase coded sequences indicate the device's capabilities and limitations. A system application is shown, in which it is used as a phase distortion filter to enhance the resolution of an acoustic pulse-echo system. Novel applications, such as an electronically variable tapped delay line and a variable pulse expander are described. Finally, the device is used to correlate input signals. In many applications, this technique increases the effective time-bandwidth product severalfold.





## ABSTRACT

This report presents a complete analytic theory of the acousto-electric storage correlator, and experimental applications which demonstrate its versatility as a signal processor. Within the storage correlator, externally applied signals interact with the potentials associated with an acoustic surface wave traveling on a piezoelectric substrate. A spatially varying charge pattern is thereby stored in a linear array of semiconductor diodes. Application of a later reading signal yields the convolution or correlation of the reading signal and the stored charge pattern.

A number of modes of both storing the charge pattern and reading it have been reported. The theory provides analytic predictions of the device performance for most of these modes of operation and most reported device structures. Experimental confirmation of the theory is given.

Particular attention is paid to the transient characteristics of  $p^{(+)}n$  diodes. It is shown both theoretically and experimentally that their response is nearly equivalent to that of fast diodes (e.g., Schottky diodes) in this application. As a consequence, they may be charged quickly (in nanoseconds) and can retain their charge for long times (seconds).

A working device has been demonstrated. Key details of its construction are discussed. Particular attention is paid to methods for reducing spurious signal generation and to an evaluation of alternate diode array structures.



A variety of signal processing results are presented to demonstrate the storage correlator's versatility as a signal processor. Correlations performed with various phase coded sequences indicate the device's capabilities and limitations. A system application is shown, in which it is used as a phase distortion filter to enhance the resolution of an acoustic pulse-echo system. Novel applications, such as an electronically variable tapped delay line and a variable pulse expander are described. Finally, the device is used to correlate input signals. In many applications, this technique increases the effective time-bandwidth product severalfold.

# TABLE OF CONTENTS

	<u>Page</u>
ABSTRACT . . . . .	iv
LIST OF FIGURES . . . . .	x
LIST OF TABLES . . . . .	xiif
LIST OF VARIABLES . . . . .	xiv
I. INTRODUCTION . . . . .	1
II. AN ANALYTIC THEORY OF THE DIODE STORAGE CORRELATOR . . .	5
1. Introduction . . . . .	5
2. Principle of Operation of the Storage Correlator . .	8
3. Analysis of Writing Modes . . . . .	14
(a) Charging Fast Diodes with a Single Pulse . . . .	14
(b) Fast Charging of pn Diodes . . . . .	18
(c) Writing into Fast Diodes with Low Level RF Signals . . . . .	20
(d) Writing into p-n Diodes with Low Level RF Signals . . . . .	22
(e) The Effect of Conductive Overlays . . . . .	24
4. Reading . . . . .	24
(a) Acoustic-to-Plate Reading . . . . .	25
(b) Plate-to-Acoustic Reading . . . . .	28
(c) Reading with Overlay Diodes . . . . .	32
5. Comparison to Experiment . . . . .	33
(a) $p^+n$ Junction Diodes, Acoustic-Plate Writing with a Single Pulse, Plate-to-Acousting Reading .	34
(b) Overlay PtSi Schottky Diodes, Acoustic-Plate Writ- ing with a Single Pulse, Acoustic-to-Plate Reading	39

# TABLE OF CONTENTS (Cont'd)

## Page

(c) $p^+n$ Diodes, Acoustic-Plate Writing with rf Signals, Plate-to-Acoustic Reading . . . . .	43
6. Conclusions . . . . .	46
III. DESIGN AND FABRICATION . . . . .	50
1. Introduction . . . . .	50
2. Diode Arrays . . . . .	53
(a) Array Design Criteria . . . . .	54
i. Density . . . . .	54
ii. Isolation . . . . .	54
iii. Uniformity . . . . .	54
iv. Storage Time . . . . .	54
(b) Summary of Structures . . . . .	54
i. Schottky Diodes . . . . .	56
ii. Planar $p^+n$ Diodes . . . . .	59
iii. V-Groove Isolated Diodes . . . . .	59
iv. Conductive Overlay Diodes . . . . .	60
(c) Comparative Evaluation of the Array Structure . .	60
(d) Summary . . . . .	63
3. Packaging . . . . .	64
(a) RF Feedthrough Suppression . . . . .	64
(b) Acoustic Feedthrough Suppression . . . . .	64
i. Phase Coded Transducers . . . . .	64
ii. Edge Effect Reduction . . . . .	67
iii. Epoxy Ringed Line . . . . .	69



# TABLE OF CONTENTS (Cont'd)

	<u>Page</u>
(c) Suppression Techniques for Spurious Bulk Waves . .	69
i. Alternate Cuts of $\text{LiNbO}_3$ . . . . .	69
ii. Top Grounds . . . . .	70
iii. Deep Slots . . . . .	70
iv. Transducers with a Large Number of Finger Pairs . . . . .	72
v. Continuous Grounds . . . . .	73
vi. Backside Roughening and Conductive Epoxy Loading . . . . .	73
(d) Actual Configuration . . . . .	74
(e) Comments on the Spacer Rails . . . . .	76
4. Electrical Design . . . . .	76
IV. SIGNAL PROCESSING APPLICATIONS . . . . .	80
1. Introduction . . . . .	80
2. General Description . . . . .	81
(a) Signal Processing Functions: Convolution and Correlation . . . . .	81
(b) Dynamic Range . . . . .	87
3. Special Cases and Experimental Results . . . . .	88
(a) Delta Function Readout . . . . .	88
i. Reproduction and Time Reversal of a Stored Signal . . . . .	88
ii. A Programmable Tapped Delay Line . . . . .	88
(b) Coded Sequences, Pulse Compression . . . . .	93
i. Barker Code Autocorrelation . . . . .	93

# TABLE OF CONTENTS (Cont'd)

	<u>Page</u>
ii. Linear FM Chirp Autocorrelation . . . . .	97
iii. Correlation of Phase Distorted Chirps . . . . .	101
iv. Transform Processing. . . . .	107
4. Input Correlation. . . . .	112
5. Limitations Due to the Device Structure. . . . .	119
(a) Charging and Storage Time Limitations . . . . .	119
(b) Degrading Factors . . . . .	123
V. CONCLUSIONS. . . . .	126
APPENDICES:	
A. Circuit Model Development. . . . .	130
B. Diffusion Equation Solutions . . . . .	135
C. Output Reduction Due to Phase Mismatching. . . . .	137
D. Processing of Diode Arrays . . . . .	141
E. ZnO/Si Schottky Diode Correlator . . . . .	144
F. The Phase Coded Transducer . . . . .	148
REFERENCES . . . . .	152

# LIST OF FIGURES

	<u>Page</u>
II-1 Device Structure . . . . .	6
II-2 Charging Circuit Model for a Fast Diode . . . . .	9
II-3 Plate-to-Acoustic Reading Circuit Model . . . . .	13
II-4 Acoustic-to-Plate Reading Circuit Model . . . . .	27
II-5 Diode Array Structures . . . . .	35
II-6 Device Output vs. Plate Pulse Height for $p^+n$ Mesa Diode Structure, Experiment and Theory . . . . .	37
II-7 Device Output vs. Plate Reading Signal Amplitude for the $p^+n$ Mesa Diode Structure with Pulse Writing, Experiment and Theory . . . . .	40
II-8 Device Output vs. Writing Power for the Overlay Schottky Diode Structure, Theory and Experiment . . . . .	41
II-9 Device Output vs. Reading Power for the Overlay Schottky Diode Structure, Theory and Experiment. . . . .	42
II-10 Device Output vs. Charging Time for Unpassivated $p^+n$ Mesa Diodes, Theory and Experiment . . . . .	44
II-11 Device Output vs. Charging Time for Passivated $p^+n$ Mesa Diodes, Theory and Experiment . . . . .	45
III-1 Correlator Packaging . . . . .	51
III-2 Device Mounted in Carrier Box with Matching Networks . . . . .	52
III-3 Diode Array Structures . . . . .	55
III-4 Experimentally Obtained Forward and Reverse Schottky Diode I-V Characteristics for Al, Au; and PtSi Diodes . . . . .	58a
III-5 V-Groove and Planar $p^+n$ Diode Comparison Experiment . .	61
III-6 Modifications of the Joly Structure to Suppress rf Feedthrough . . . . .	65



	<u>Page</u>
III-7    The Phase Coded Transducer and its Use in the Storage Correlator . . . . .	66
III-8    The Peak Spurious Signal Response vs. Frequency for Unmodified, Coded Transducer and Epoxy Devices . . .	68
III-9    The Top Ground System and its Equivalent Circuit Model .	71
III-10   Device Assembly for Reduced Spurious Acoustic Responses . . . . .	75
III-11   The Plate Matching Network and its Calculated Input Impedance and Transfer Characteristics . . . . .	77
III-12   The High Voltage Pulser Circuit and a Typical Output Pulse . . . . .	79
IV-1    Electronically Variable Delay with the Storage Correlator . . . . .	90
IV-2    The Phase Reversal (Barker) Code . . . . .	94
IV-3    Biphase Barker Code Correlation Experimental Results . .	96
IV-4    FM Chirp Autocorrelation and Experimental Result . . . .	100
IV-5    Ideal Representations of Radar and Sonar Pulse-Echo Systems . . . . .	103
IV-6    Schematic of the Acoustic Pulse-Echo System . . . . .	105
IV-7    Pulse-Echo Experiment Results with Both Good and Poor Transducers . . . . .	106
IV-8    Pulse-Echo Experiment Results Showing S/N Gain of the System . . . . .	108
IV-9    The Analog Pulse Expander System and an Experimental Result . . . . .	110
IV-10   Input Correlation Setup and an Experimental Result . . .	117
IV-11   Device Output as a Function of the Charging Pulse Amplitude for Various Temperatures . . . . .	121

	<u>Page</u>
A-1 The Acoustic Circuit (from July <sup>27</sup> ) . . . . .	131
A-2 The plate Circuit, (a) Physical Situation and (b) Circuit Model for a Single Diode . . . . .	131
A-3 The Complete Device Equivalent Circuit Model . . . . .	134
A-4 Reduced Equivalent Circuit Model . . . . .	134
C-1 Output Reduction due to the Phase Mismatch of the Writing and Reading Signals, Experiment and Theory . . .	140
E-1 The ZnO/Si Convolver with Schottky Diode Storage . . .	145
E-2 Schottky Barrier Diode ZnO Convolver . . . . .	146
F-1 The Phase Coded Transducer Output vs. Angle of Incidence . . . . .	151

## LIST OF TABLES

	<u>Page</u>
II-1    Experimental Device Parameters . . . . .	36
III-1   Diode Array Dimensions . . . . .	56
III-2   Theoretical Leakage Currents and Storage Times . . . . .	57
III-3   Experimental Schottky Diode Characteristics . . . . .	58
IV-1    Storage Correlator Output Functions . . . . .	83
IV-2    Barker Code Correlations . . . . .	97



# LIST OF VARIABLES

- ( ) Equation number where variable is defined or first used.
- a: Spatial dependence of fundamental acoustic mode (II-42).
- C: Reduced model coupling capacitance,  $= C_a + C_p$  (II-1).
- $C_a$ : Acoustic coupling capacitance (II-1)
- $C_D$ : Diode capacitance (II-5).
- $C_{D0}$ : Diode capacitance for  $V_D = 0$  (II-5).
- $C_{Dp}$ : Peak diode capacitance for pulse writing (II-14).
- $C_{ov}$ : Overlay capacity (II-54).
- $C_p$ : Plate circuit coupling capacitor (II-1).
- $C_T$ : Total capacity  $= C + C_D$  (II-16).
- $C_{Tp}$ : Peak total capacity,  $= C + C_{Dp}$  (II-14)
- d: Piezoelectric substrate thickness (A-4).
- $D_p$ : Minority carrier diffusion constant (II-19).
- $E_g$ : Semiconductor bandgap energy (Sec. 2.5(a)).
- f: Filling factor (C-1).
- h: Airgap thickness (A-2).

$I_a$ : Current in acoustic circuit (Fig. A-3).  
 $I_D$ : Total diode current (A-5).  
 $I_n$ : Readout current through  $n^{\text{th}}$  diode element (II-38).  
 $I_p$ : Current in plate circuit (Fig. A-3).  
 $I_s$ : Diode reverse saturation current (II-14).  
 $k$ : Boltzmann's constant (II-10).  
 $\ell$ : Diode array periodicity (II-50).  
 $L$ : Length of interaction region (II-40).  
 $\mathcal{M}_c$ : Efficiency of acoustoelectric convolver (II-61).  
 $\mathcal{M}_{sc}$ : Efficiency of storage correlator (II-60).  
 $M(\beta h)$ : Space charge coupling factor (C-3).  
 $n_i$ : Intrinsic carrier density (Sec. 2.5(a))  
 $N$ : Number of diode elements per unit length (II-39).  
 $N_D$ : Semiconductor doping density (II-5).  
 $p_n(x,t)$ : Minority carrier density in neutral region (II-19)  
 $p_{n0}$ : Equilibrium minority carrier density (II-19).  
 $P_a$ : Acoustic signal power (A-1)

- $P_0$ : Output power (reading) (II-40).
- $q$ : Electron charge (II-5).
- $Q_R$ : Readout charge (II-4).
- $Q_{RD}$ : Component of  $Q_R$  stored in the diode capacitor,  $C_D$  (II-55).
- $Q_D$ : Total charge in the diode capacitor,  $C_D$  (II-5).
- $Q_0$ : Component of stored charge without spatial phase  $\beta z$  (II-4).
- $Q_p$ : Excess minority carrier charge in neutral region (B-4).
- $Q_s$ : Total stored charge,  $Q_s = Q_0 + Q_R$  (II-11).
- $R_L$ : Output load resistance (II-39).
- $R_p$ : Series resistance in plate circuit (Fig. A-2).
- $t$ : Time (II-3).
- $t_p$ : Time of peak of writing pulse (II-4).
- $T$ : Temperature (II-10).
- $T_p$ : Minority carrier recombination time constant (B-1).
- $v_a$ : Acoustic propagation velocity (A-2).
- $V_{a0}$ : Modulation of acoustic signal (II-13).
- $V_{a1}, V_{a2}$ : Acoustic writing potential (acoustic-acoustic mode) (below Eq. II-28).



- $V_B$ : Built-in diode junction voltage (II-5).
- $V_D$ : Diode voltage (II-5).
- $V_{Dp}$ : Peak diode voltage during pulse writing (II-17).
- $V_{DR}$ : Diode voltage component exciting readout (acoustic-to-plate mode) (II-37).
- $V_{Dr}^+$ : Diode voltage component exciting readout (plate-to-acoustic mode) (II-41).
- $V_{Dr0}$ : Coefficient of spaceharmonic expansion of  $V_{Dr}^+$  (II-50).
- $V_L$ : Voltage developed across output load resistor,  $R_L$  (II-39).
- $V_{on}$ : Turn-on voltage (II-18).
- $V_{po}$ : Peak amplitude of plate writing signal (II-13).
- $V_s$ : Reduced model source voltage (II-24).
- $w$ : Acoustic beam width (A-2).
- $z$ : Position along diode array (II-3).
- $z_n$ : Position of  $n^{th}$  diode array element (II-39).
- $Z_a$ : Acoustic impedance (A-1).
- $\beta$ : Acoustic propagation constant (II-3).
- $\delta$ : Diode array element width (II-39)
- $\epsilon_0$ : Dielectric constant of air (A-2).

- $\epsilon_p$ : Dielectric constant of piezoelectric (rf) (A-4).
- $\epsilon_{pa}$ : Dielectric constant of piezoelectric (acoustic) (A-2).
- $\epsilon_s$ : Dielectric constant of semiconductor (II-5).
- $\gamma$ : Perturbation in  $\beta$  due to presence of semiconductor (II-44).
- $\omega$ : Radial frequency (II-3).
- $\phi$ : Total acoustic potential seen in space above piezoelectric,  
 $= \phi_a + \phi_s$  (II-44).
- $\phi_1$ : Fundamental term in harmonic expansion of acoustic potential (II-42).
- $\phi_a$ : Potential due to fundamental propagating acoustic mode (II-44).
- $\phi_s$ : Potential due to all other acoustic modes (II-43).
- $\phi_{ar}$ : Readout surface wave potential (II-34).
- $\phi_{pr}$ : Plate reading potential (II-8).
- $\rho_s$ : Semiconductor surface charge density due to  $\phi_s$  (II-42).
- $|\Delta v/v_a|$ : Measure of coupling to piezoelectric substrate (A-2).

## CHAPTER I

### INTRODUCTION

This report describes the theory, construction, and signal processing applications of the diode acoustoelectric storage correlator. This device can, in real time, correlate or convolve a broadband reading signal with a stored reference signal.

The storage correlator structure is nearly identical to that of the diode acoustoelectric convolver, which has been described in detail elsewhere.<sup>27</sup> The device consists of a semiconductor diode array spaced a few hundred nanometers above a piezoelectric acoustic surface wave delay line.

We are here concerned with a new mode of convolver operation, in which signals are stored as a charge pattern in the diode array. This storage is accomplished through the interaction of rf potential applied across the device and the diode potentials due to acoustic surface waves traveling underneath the diode array.

As will be seen, the ability to real time correlate or convolve a stored signal with a later input provides advantages not realized in earlier acoustoelectric devices. In many modes the storage correlator operates entirely at baseband. Real time signal processing is achieved with no synchronization problems. Finally, an integrating mode of storage allows the correlation of extremely long signals.

The first storage correlators were demonstrated in 1974 by Hayakawa and Kino,<sup>6</sup> and by Cafarella and Bers.<sup>5</sup> These devices employed silicon surface state storage. In 1975 Ingebrigtsen demonstrated the first device employing storage in an internal array of semiconductor



diodes.<sup>7</sup> This sort of storage mechanism has proven far superior, yielding more controllable and reproducible characteristics. Here, we shall be concerned solely with devices employing diode storage.

Diode storage correlators have been demonstrated with either Schottky diode<sup>7</sup> or pn junction diode storage.<sup>9</sup> These have been developed for both signal processing<sup>14</sup> and imaging applications.<sup>26</sup> Auld,<sup>48</sup> Grudkowski,<sup>64</sup> Reeder,<sup>65</sup> and, Menager and Desormier,<sup>62</sup> and others<sup>49</sup> have demonstrated devices with tapped delay lines and external diodes. These exhibit good performance, although large numbers of taps and considerable external circuitry are required.

The work described here was initiated contemporary to Ingebrigtsen's original demonstration of the diode storage correlator. It since has yielded a number of unique contributions. These include the first complete theory of the storage correlator, the first application of the device to a real pulse-echo system, and one of the first demonstrations of high gain correlation during the charging process.

Four chapters follow this introduction. Chapter II presents a complete theoretical description of the storage correlator. This theory is completely analytic, and is valid for most reported device structures and modes of operation. The discussion begins with a qualitative description of the various modes of operation considered, and then proceeds to an analytic description. Experimental results are presented to confirm the various aspects of the theory. Finally, the relative efficiency of the various modes of operation and device structures are theoretically compared. A comparison of the relative efficiencies

of the storage correlator and acoustoelectric convolver is also provided.

Chapter III discusses device construction. First, the basic structure and problems are described. The diode array is then considered in detail. The fabrication criteria are listed, followed by a summary of the various diode structures considered and a discussion of their relative performance. The suppression of both electrical and acoustic feedthrough is discussed. A number of techniques are listed, along with their relative virtues and disadvantages. Finally, various useful electrical circuits are presented. These include plate matching network and high voltage pulser designs.

Chapter IV discusses signal processing applications. First, the theoretical results of Chapter II are used to find the device output functions for various modes of operation. It is thus shown that the device always provides either a convolution or correlation at the output. Various experimental results are given. These show how the device may be employed as an electronically variable tapped delay line for long analog signals, as a matched filter to reduce phase distortions in a pulse-echo system, and as a transform processor with a novel application as an analog pulse expander. Finally, the technique of input correlation is considered in detail. Here, the diode array is used to integrate during the charging process, so that extremely long signals may be correlated. This process yields extremely high time-bandwidth product phase correlations. A discussion of the independence of the writing and storage time is also included. It is experimentally

demonstrated that the writing and storage times are essentially independent, so that even very long storage time diodes may be charged extremely quickly.

Chapter V is a conclusion, summarizing the salient features of the earlier chapters. Future directions of the storage correlator are also discussed, such as imaging applications, monolithic devices, and two-dimensional storage. Remaining problems are also discussed.



## CHAPTER II

### AN ANALYTIC THEORY OF THE DIODE STORAGE CORRELATOR

#### 1. Introduction

The acoustoelectric surface wave storage correlator is a device capable of storing and correlating broad bandwidth signals in real time. Considerable development has occurred since the first demonstration of principle, and a number of device structures and modes of operation have evolved. Here, we derive an analytic theory broad enough in scope to elucidate the physics and accurately predict the performance of most of the reported structures and modes of operation.

The device considered consists of a silicon diode array situated a few hundred nanometers above an acoustic surface wave delay line, as shown in Fig. II-1. It has three ports: two connected to acoustic surface wave transducers, (L,R), and a third, called the plate (P), connected to the back of the diode array. The interaction of inputs from any two of the ports writes a signal into the diode array in the form of a spatially varying charge pattern. A later input, called the readout signal, causes a readout to appear at one of the three ports in the form of a correlation or convolution of the readout signal and the stored charge pattern.

The first version of the storage correlator, reported in 1974 by Cafarella and Bers,<sup>5</sup> and also by Hayakawa and Kino,<sup>6</sup> employed surface state storage in silicon. In 1975, Ingebritsen<sup>7</sup> demonstrated the first device with storage in Schottky diodes. Soon afterward, Maerfeld and Tournois,<sup>19</sup> and also Borden and Kino,<sup>14</sup> reported results with devices

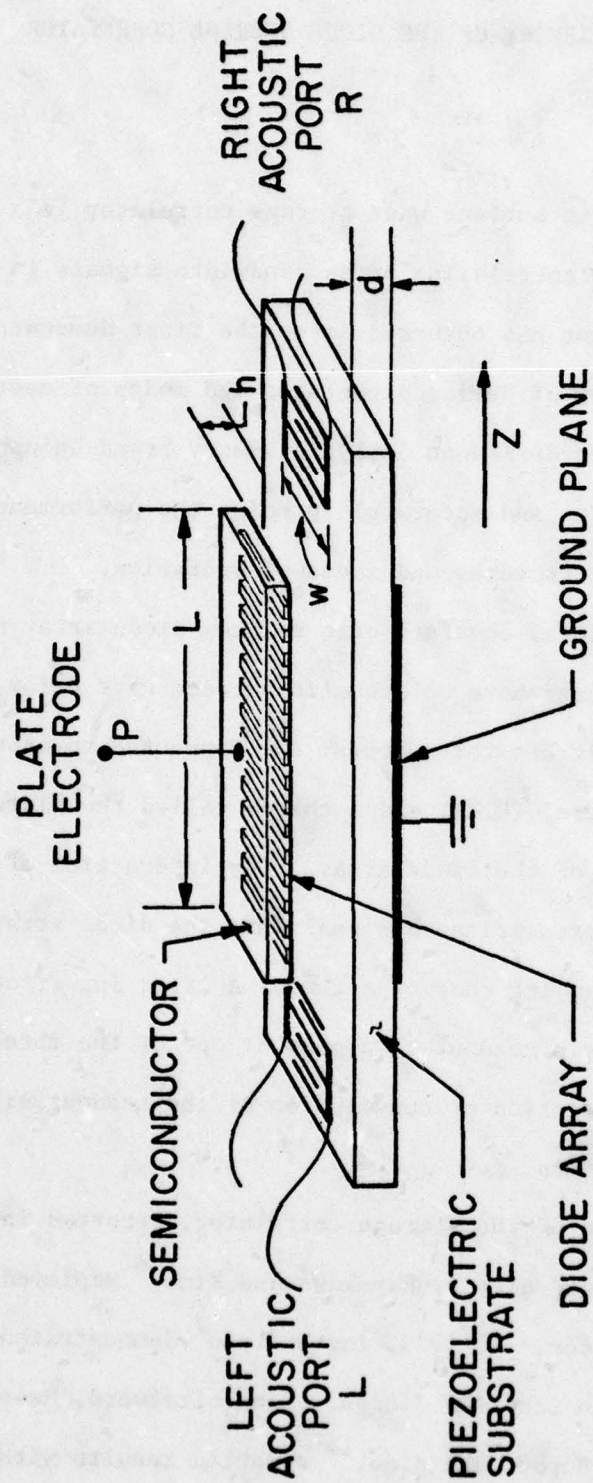


FIG. II-1 Device Structure.

employing storage in arrays of p-n junction diodes. In general, diode storage has proven far superior to surface state storage with respect to reproducibility, storage time, efficiency and uniformity. This motivates restricting the scope of this paper to the diode correlator; indeed, most current devices employ arrays of either Schottky or p-n junction diodes as the storage medium.

Past theoretical treatments have considered the storage of signals in surface states,<sup>5</sup> or of low level input signals in diodes.<sup>19,61</sup> Here, we give a general theory with results in analytic form. The performance of a diode correlator is predicted when any reported method of writing a signal into the diode array is coupled with any reported readout technique. The assumptions thus required in most cases minimally affect the final accuracy; we will note when this is not the case.

We shall consider two methods of writing a signal into the diode array. In the first, a very short high amplitude plate pulse is used to strongly forward bias the entire diode array. In this manner, it is possible to sample the diode potentials due to a traveling surface wave present under the diode array. The surface wave's amplitude and phase information is thereby stored in the diode array as a spatially varying charge pattern, which is manifested as a spatial variation of diode capacity. The second method employs a large number of weak sampling pulses, each insufficient in amplitude to strongly forward bias the diodes. Here, the writing process occurs over a long period of time. A nearly identical process is to employ two oppositely traveling surface acoustic waves to write a charge pattern into the diodes over a long period of time.

We also consider two methods of reading the diode capacities. The first, called *acoustic-to-plate reading*, employs an acoustic surface wave traveling under the diode array to excite individual diodes; the potential



developed across a diode depending on its capacity and the amplitude of the surface acoustic wave. An rf output is obtained at the plate terminal, P. In the second, called *plate-to-acoustic reading*, the excitation of the diodes by a reading signal at the plate terminal gives rise to an output acoustic surface wave.

The analysis is performed for both fast (such as Schottky) and p-n junction diodes. A fast diode is defined as a device whose conduction current is of the form  $I_s (e^{qV_D/nkT} - 1)$ , regardless of the rise time of the diode voltage. This is seldom true for p-n diodes in this application. Hence, the p-n diode analysis will account for their transient response. The theory is also adapted for either type of diode with conductive overlays.

Following the analysis, we present experimental results that verify most aspects of the theory. Finally, we compare the performance of the various device structures and modes of operation, and the storage correlator's efficiency as opposed to that of other existing acousto-electric signal processing devices.

## 2. Principle of Operation of the Storage Correlator

The process of writing a charge pattern into the diode array may be understood with the aid of the circuit model of Fig. II-2. In Appendix A, we show that this model suitably represents the charging process. There, the effective coupling capacity  $C$  of this circuit is shown to be

$$C = C_a + C_p \quad (\text{II-1})$$

where  $C_a$  is associated with excitation of the diode by the acoustic wave, and  $C_p$  with excitation at the plate electrode.

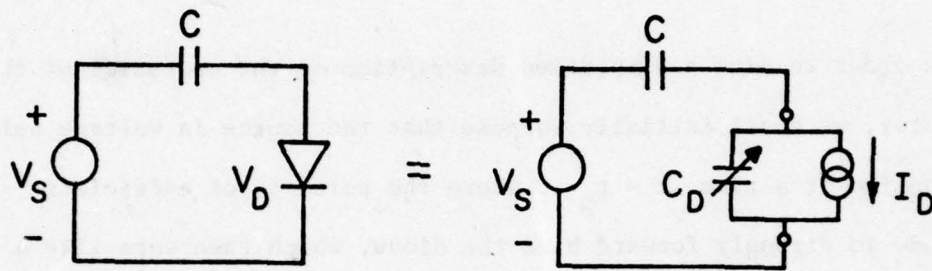


FIG. II-2 Charging Circuit Model for a Fast Diode.

The effective source voltage  $V_s$  is related to the potentials  $V_a$  at the surface of the piezoelectric substrate and  $V_p$  at the plate as follows:

$$V_s = \frac{C_a}{C} V_a + \frac{C_p}{C} V_p \quad . \quad (\text{II-2})$$

In order to give a simplified description of the operation of the correlator, we shall initially suppose that the source is voltage pulse  $V_{p0}$  applied at a time  $t = t_p$ , where the pulse is of sufficient amplitude to strongly forward bias the diode, which then acts like a closed switch. The operation is that of sample and hold circuit, which samples the relatively weak acoustic wave signal passing underneath the diode at the time  $t_p$ . Suppose the voltage applied by the acoustic wave is of the form

$$V_a = V_{a0} \sin(\omega t - \beta z) \quad (\text{II-3})$$

where  $\beta$  is the propagation constant of the acoustic wave.

After the pulse voltage drops to zero, the capacitors retain a charge due to the acoustic wave of the form

$$Q = CV_s = C_p V_{p0} + C_a V_{a0} \sin(\omega t_p - \beta z) \quad (\text{II-4})$$

$$= Q_0 + Q_R$$

where  $Q_R$  is the spatially varying component of  $Q$ .



Once the pulse voltage drops to zero, the diode is reverse biased and acts like a varactor, whose capacity is determined by the storage charge  $Q$ .  $Q$  decreases slowly in time due to the leakage current of the diode.

If we suppose that  $C_p \ll C_D$ , the capacitance of the diode, we can write in general, that  $Q \approx Q_D$ , where  $Q_D$  is the diode charge, given by the relation

$$\begin{aligned} Q_D &= \sqrt{2qN_D \epsilon_s V_B} - \sqrt{2qN_D \epsilon_s (V_B - V_D)} \\ &= C_{D0} V_B - C_D (V_B - V_D) \end{aligned} \quad (\text{II-5})$$

with

$$C_D = \left[ 2qN_D \epsilon_s / (V_B - V_D) \right]^{1/2} \quad (\text{II-6})$$

where  $V_B$  is the built-in voltage of the diode,  $N_D$  its doping,  $\epsilon_s$  its dielectric constant,  $C_D$  its large signal capacity and  $C_{D0}$  its capacity when  $V_D = 0$ , with  $Q_{D0} = C_{D0} V_B$ . We note that the definition of  $C_D$  differs from the usual small signal definition by a factor of 2.

Under reverse biased conditions, where  $V_D$  is negative, we can write

$$\frac{1}{C_D} = \frac{1}{C_{D0}} \times \frac{Q_{D0} - Q_D}{Q_{D0}} \quad (\text{II-7})$$

so the spatially varying component of  $1/C_D$  is  $Q_R/Q_{D0}C_{D0}$ .

On readout in the plate-to-acoustic mode, a voltage  $\phi_{pr} \sin \omega t$  is applied to the plate as shown in Fig. II-3. This in turn develops a voltage across the diode capacitance of value

$$V_D \approx \frac{C_p \phi_{pr} \sin \omega t}{C_D} \quad (II-8)$$

So, from Eqs. (II-7) and (II-8), the spatially varying voltage component developed at the diodes is of the form

$$V_{Dr} = \frac{C_p C_a V_{a0} \phi_{pr} \sin(\omega t_p - \beta z) \sin \omega t}{C_{D0}^2 V_B} \quad (II-9)$$

We note that this voltage is independent of the original pulse voltage applied, but is linearly proportional to the acoustic signal read into the device as well as the readout signal  $\phi_{pr}$ . It has the same frequency variation as the input signal and two components of spatial variation  $\pm \beta z$ . These correspond to both forward and backward propagating acoustic surface waves.

Thus, the principle of operation on writing is to use the diodes as sample and hold circuits which retain charge. On readout the spatial variation of the capacitances of the diodes due to the retained charge is such that a readout voltage applied to the plate excites the diodes with the same spatial variation of potential. This, in turn, excites

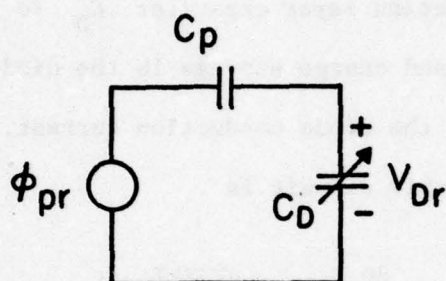


FIG. II-3 Plate-to-Acoustic Reading  
Circuit Model.



forward and backward propagating modes whose amplitudes can be determined by normal mode theory.

### 3. Analysis of Writing Modes

#### (a) Charging Fast Diodes with a Single Pulse.

The charging circuit model for fast diodes is shown in Fig. II-1. Here, we include a depletion layer capacitor  $C_D$  to account for the displacement current flow and charge storage in the diode. The current generator accounts for the diode conduction current.

The current equation for this circuit is

$$C \frac{d}{dt} (V_s - V_D) = \frac{dQ_D}{dt} + I_s \left( e^{qV_D/kT} - 1 \right) \quad (\text{II-10})$$

where  $Q_D$  is the charge diode depletion layer capacitor  $C_D$ , as defined in Eq. (II-5). We define the stored charge  $Q_S(t)$  as the change due to the flow of conduction current, as follows:

$$Q_D(t) = C(V_s - V_D) - Q_S(t) \quad (\text{II-11})$$

Substitution of Eq. (II-11) in Eq. (II-10) yields the stored charge  $Q_S$  in the form

$$\frac{dQ_S}{dt} = I_s \left( e^{qV_D/kT} - 1 \right) \quad (\text{II-12})$$

If  $V_D = 0$  initially,  $Q_S = 0$ . While the conduction current is small, the RHS of Eq. (II-12) makes no contribution as  $V_s$  changes and  $Q_S = 0$  with  $Q_D = C(V_s - V_D)$ . When the diode is forward biased,  $V_D > 0$ ,

and the charge  $Q_S$  increases rapidly in time. Then, after the diode is again reverse biased ( $V_D \lesssim 0$ ),  $Q_S$  remains essentially constant over time periods of the order of tens of microseconds, and decreases linearly with time over much longer periods, due to the diode reverse saturation current  $I_S$ . Thus, we identify  $Q_S$  with the stored charge. Note that changes in the amount of stored charge are due solely to the flow of diode conduction current.

Eq. (II-12) can be solved analytically only with certain assumptions about the diode capacity  $C_D$ . For our purpose,  $C_D$  is defined in terms of  $Q_D$ , the net charge in the diode, given in the abrupt depletion approximation by Eqs. (II-5) and (II-6).

To retain analytic forms, we shall assume the diode capacity  $C_D$  to be constant and of value  $C_{Dp}$  during the time when the diode is strongly forward biased at an essentially constant voltage  $V_{Dp}$ . It is during this time that the bulk of the charging current flows. For writing with small signals, the zero bias diode capacitance  $C_{D0}$  is used. During storage and reading, the diode reverse bias voltage is used to evaluate  $C_D$ .

Equation (II-12) can be integrated with the aid of Eqs. (II-11) and (II-5) to find the net stored charge  $Q_S$ . We assume a source voltage  $V_s$  of the form

$$V_s = \frac{C_a}{C} V_{a0} \sin(\omega t - \beta z) + \frac{C_p}{C} V_{p0} \left[ 1 - \left( \frac{t - t_p}{t_p} \right)^2 \right]. \quad (\text{II-13})$$

The first term on the right is due to the acoustic surface wave. The second term is due to the much larger applied plate pulse, which is assumed to be parabolic in shape, with a peak amplitude  $V_{p0}$ , occurring at time  $t_p$ . Such a pulse shape models a short voltage spike in an easily integrable form. After integration and the use of asymptotic approximations near  $t = t_p$ , the stored charge is found to be

$$Q_S = \frac{kT}{q} C_{Tp} \left[ \ln \sqrt{\frac{\pi q}{kTC_{Tp} C_p V_{p0}}} I_s t_p e^{q/kTC_{Tp} [CV_s(t_p) + V_B(C_{Dp} - C_{D0})]} + 1 \right] \quad (II-14)$$

with  $C_{Tp} = C_{Dp} + C$ . For most cases of interest, the argument of the logarithm is much greater than unity. Thus, we can write  $Q_S$  in the form

$$Q_S \approx CV_s(t_p) + V_B(C_{Dp} - C_{D0}) + \frac{kT}{q} C_{Tp} \ln \left[ I_s t_p \sqrt{\frac{\pi q}{kTC_{Tp} C_p V_{p0}}} \right] \quad (II-15)$$

where  $CV_s(t_p)$  is given precisely by the simplified form of Eq. (II-4), in which the diode was regarded as a perfect switch. The rest of the terms in Eq. (II-15) account for the fact that a finite voltage is required to "turn on" the diode.

It follows from Eqs. (II-5), (II-6), (II-11) and (II-15) that the diode voltage is



$$V_D(t) = \frac{C}{C_T} [V_s(t) - V_s(t_p)] + \frac{V_B(C_D - C_{Dp})}{C_T} - \frac{kT}{q} \frac{C_{Tp}}{C_T} \ln \left[ I_s t_p \sqrt{\frac{\pi q}{kTC_{Tp} C_p V_{p0}}} \right] \quad (II-16)$$

where  $C_D$  and  $C_T = C_D + C$  are evaluated with a value of diode voltage  $V_D$  self-consistent with Eqs. (II-5) and (II-6). The last term on the RHS of Eq. (II-16) gives the peak diode voltage,  $V_{Dp}$ , when  $C_D = C_{Dp}$  and  $V_s = V_s(t_p)$ , as

$$V_{Dp} = - \frac{kT}{q} \ln \left[ I_s t_p \sqrt{\frac{\pi q}{kTC_{Tp} C_p V_{p0}}} \right]. \quad (II-17)$$

The diode reverse voltage after charging can be found from Eq. (II-16) by setting the source voltage  $V_s(t) = 0$ .

Finally, we determine the turn-on voltage  $V_{on}$ , the minimum plate pulse amplitude  $V_{p0}$  required to sufficiently forward bias the diode for complete charging. The turn-on voltage  $V_s = V_{on}$  is defined to be the plate potential when the charge  $Q_{Dp}$  stored in the depletion layer capacity  $C_{Dp}$  equals the stored charge  $Q_s$  due to the flow of conduction current when the diode reaches its saturation voltage  $V_{Dp}$ . It can be seen from Eq. (II-11) that this occurs when  $Q_s = C(V_s - V_{Dp})/2$ . Thus, it follows from Eqs. (II-2), (II-5) and (II-11) that

$$V_{on} = V_{Dp} \frac{(2C_{Dp} + C)}{C_p} - \frac{C_a V_{a0}}{C_{Tp}} + \frac{2V_B}{C_p} (C_{D0} - C_{Dp}) \quad (II-18)$$

In most cases, the first term on the RHS dominates; this is seen to be  $V_{Dp}(2C_{Tp} - C)/C_p$ . We note, however, that some charge is stored

as soon as  $Q_S$  is finite, a condition closer to  $V_{on} \approx C_{Tp} V_{Dp} / C_p$ , where it is assumed that finite conduction current only flows as  $V_D$  approaches  $V_{Dp}$ .

(b) Fast Charging of pn Diodes.

In Appendix B, the excess minority carrier charge density at the edge of the neutral region,  $p_n(0,t)$ , for times much shorter than the minority carrier lifetime was shown to be

$$p_n(0,t) = p_{n0} \left( e^{qV_D/kT} - 1 \right) = \frac{1}{q\sqrt{\pi D_p}} \int_0^t \frac{I_D(\tau)}{(t-\tau)^{1/2}} d\tau. \quad (II-19)$$

The analysis here is parallel to the fast diode case. The source voltage  $V_s$  is again given by Eq. (II-13), where the dominant signal is a parabolic plate pulse peaking at a time  $t_p$ . We are here interested in the transient diode characteristics, in response to the sharply peaked plate pulse rather than the weaker acoustic signal.

Since most of the source voltage drops across the coupling capacitor  $C$ , the diode is driven by a current varying linearly with time:

$$I_D = C \frac{dV_s}{dt} \approx \frac{2CV_p}{t_p} \left( 1 - \frac{t}{t_p} \right). \quad (II-20)$$

For this case, it will be seen from Eq. (II-20) that the forward diode voltage  $V_D$  during charging is given by the relation

$$V_D(t) = \frac{kT}{q} \ln \left[ 1 + \frac{4CV_{p0}}{q p_{n0} t_p} \sqrt{\frac{t}{\pi D_p}} \left( 1 - \frac{2t}{3t_p} \right) \right]. \quad (II-21)$$

The diode voltage  $V_D$  climbs rapidly to saturation (typically 0.5 to 0.6 volts) and remains constant until a time  $t \approx 3t_p/2$ , when  $V_D$  rapidly drops to zero. At this time, the source voltage is  $V_s = 3V_{p0}/4$ . For  $t > 3t_p/2$ ,  $V_D < 0$ , and all diode conduction current ceases to flow. Because a reverse current flows during the period  $t_p < t < 3t_p/2$ , we expect the stored charge to be only 75% of that found in the fast diode case, and the charge contributing to readout is

$$Q_R^{pn} = 0.75 Q_R^{fast} \quad . \quad (II-22)$$

This rapid response is due to the drift of holes across the depletion layer from the  $p^+$  region to the  $n$  region. Not all this charge is stored because insufficient time has elapsed to allow the holes to diffuse into the neutral region. The holes near the edge of the neutral region drift back to the  $p^+$  region when the diode current changes sign, at time  $t = t_p$ . This reverse current, during the interval  $t_p < t < 3t_p/2$ , causes the loss of 25% of the original stored charge. For times beyond  $3t_p/2$ , essentially no conduction current flows, so that 75% of the original stored charge is retained. Note that this process is transit time limited, and is essentially independent of the minority carrier lifetime and, hence, diode storage time.

This analysis may be inadequate for diodes with a very long minority carrier lifetime. In this case, it is possible that the minority carriers that have flowed across the junction during the charging peak do not recombine. A large number of these carriers might then diffuse to the junction and drift back across after the charging pulse turns off.



This would explain why others have experienced difficulty in charging long lifetime pn diodes with short pulses.<sup>19</sup>

However, it must be noted that for reasonably large charging pulses, the diodes are operating near or in the high level injection regime. This suggests that the minority carriers must in fact experience field aided drift in the neutral region, so that they would be pushed deep into the bulk and away from the junction. Except for the case of diodes with extremely long lifetime, most of these minority carriers would probably recombine before being able to diffuse back to the junction.

(c) Writing into Fast Diodes with Low Level RF Signals

Plate-acoustic writing,  $V_{p0} \ll V_{a0}$ . This case is physically analogous to single pulse writing, except that the diode is never strongly forward biased. Thus, the diode forward current is low and a long train of pulses are required to completely charge the circuit. The stored charge and diode voltage are found, as before, with the differential Eq. (II-10), except that the source voltage is given by

$$V_s(t) = \frac{C_a V_{a0}}{C} \sin(\omega t - \beta z) + \frac{C_p V_{p0}}{C} \sin \omega t \quad (\text{II-23})$$

with the assumptions that  $e^{qV_{a0}/kT} \gg e^{qV_{p0}/kT}$  and  $V_{a0}$  is of sufficiently low amplitude so that the diode displacement current greatly exceeds its conduction current.

Because the diode is weakly forward biased, a constant zero bias diode capacitance  $C_D = C_{D0}$  is assumed. By integration of Eq. (II-12), the stored charge is then given by the relation

$$Q_s = \frac{kT}{q} C_T \ln \left\{ 1 + \frac{qI_s}{kTC_T} \int_0^t \exp \left[ \frac{q}{kTC_T} (C_a V_{a0} \sin(\omega t - \beta z) + C_p V_{p0} \sin \omega t) \right] dt \right\} \quad (II-24)$$

The argument of the integral in Eq. (II-24) is sharply peaked when  $\omega t - \beta z = \pi/2$ . Thus, the integral is rewritten as

$$\frac{2\pi}{\omega} \exp \left[ \frac{q}{kT} \frac{C_p}{C_T} V_{p0} \cos \beta z \right] \left\{ \frac{N_c}{2\pi} \int_0^{2\pi} \exp \left( \frac{q}{kT} \frac{C_a}{C_T} V_{a0} \sin(\omega t - \beta z) \right) d(\omega t) \right\}$$

where  $N_c$  is the number of rf cycles used for charging,  $N_c = \omega t/2\pi$ .

The integral yields a Bessel function  $I_0(qV_{a0}C_a/kTC_T)$ , so that Eq. (II-24) reduces to

$$Q_s(t) = \frac{kT}{q} C_T \ln \left[ 1 + \frac{qI_s t}{kTC_T} I_0 \left( \frac{q}{kT} \frac{C_a}{C_T} V_{a0} \right) \exp \left( \frac{q}{kT} \frac{C_p}{C_T} V_{p0} \cos \beta z \right) \right] \quad (II-25)$$

The readout charge is the component of the stored  $Q_s$  with periodicity  $\cos \beta z$ . This is found by Fourier expansion of Eq. (II-25) to be

$$Q_R = \frac{kT}{\pi q} C_T \int_0^{2\pi} \cos \theta \ln \left[ 1 + \frac{qI_s t}{kTC_T} I_0 \left( \frac{q}{kT} \frac{C_a}{C_T} V_{a0} \right) \times \exp \left( \frac{q}{kT} \frac{C_p}{C_T} V_{p0} \cos \theta \right) \right] d\theta \quad (II-26)$$

The integral in Eq. (II-26) is not easily tractable. For large  $t$ , it has an asymptotic form of

$$C_R = C_p V_{p0} \quad (II-27)$$

For shorter times, the readout charge  $Q_R$  is of the form

$$Q_R \approx 2I_s t I_0 \left( \frac{q}{kT} V_{a0} \frac{C}{C_T} \right) I_1 \left( \frac{q}{kT} V_{p0} \frac{C}{C_T} \right) \quad (II-28)$$

where  $I_1(x) = d/dx I_0(x)$ .

Acoustic-acoustic writing ( $V_{a1} \gg V_{a2}$ ). For the case of writing with two acoustic signals,  $V_{a1} e^{j(\omega t - \beta z)}$  and  $V_{a2} e^{j(\omega t + \beta z)}$ , with  $e^{qV_{a1}/kT} \gg e^{qV_{a2}/kT}$ , the above analysis follows with  $V_{a2}$  replacing  $V_{p0}$ . Now the readout charge  $Q_R$  is the component of the stored charge  $Q_s$  with spacial frequency  $2\beta z$ .

#### (d) Writing into p-n Diodes with Low Level RF Signals

This case is analogous to that of the fast diode and the source voltage  $V_s$  is again given by Eq. (II-23) with the previous assumptions applying. It will now be convenient to assume that the diode voltage is determined by the capacitive voltage divider of the coupling capacitor  $C$  and the diode capacitor  $C_D$ . Including the increasing diode bias due to the buildup of stored charge  $Q_s$  and assuming the diode capacity  $C_D$  remains essentially constant at its zero bias value  $C_{D0}$ , the diode voltage is



$$V_D(t) = \frac{C}{C_T} V_s - \frac{Q_s}{C_T} \quad (II-29)$$

We apply Eq. (B4), which allows calculation of the increment in minority carrier charge  $\Delta Q_p$ , during one rf cycle of the source voltage  $V_s$ . Since the current from the  $p^+$  to  $n$  regions is due to minority carriers, this yields the increment in stored charge. Substituting Eq. (II-29) into Eq. (B4) gives

$$\Delta Q_p = q p_{n0} \sqrt{\frac{D_p}{\pi}} \int_0^{2\pi} \frac{e^{(q/kTC_T)[CV_s(\tau) - Q_s]}}{(t - \tau)^{1/2}} d\tau \quad (II-30)$$

We note that this description is probably adequate for both long and short lifetime pn diodes. Here, the charging current is small, and minority carriers that have traversed the junction can easily recombine.

If the increment in charge  $\Delta Q_p$ , as given in Eq. (II-30), is small so that charging occurs over a large number of rf cycles, then Eq. (II-30) may be written in the form of a differential equation,

$$\frac{dQ_s}{dt} \approx \frac{\omega}{2\pi} \Delta Q_p = \frac{\omega q p_{n0}}{2\pi} \sqrt{\frac{D_p}{\pi}} e^{Q_s/kTC_T} \times \int_0^{2\pi} \frac{e^{(qC/kTC_T)V_s(\tau)}}{(t - \tau)^{1/2}} d\tau \quad (II-31)$$

Integration of Eq. (II-31) gives the stored charge  $Q_s$  as

$$Q_s(t) = \frac{kT}{q} C_T \ln \left[ 1 + \frac{q}{kTC_T} \left( \frac{q p_{n0}}{\pi} \sqrt{\frac{2\omega D_p}{3}} \right) t I_0 \left( \frac{q C_a V_{a0}}{kTC_T} \right) \exp \left( \frac{q}{kT} \frac{C_p}{C_T} V_{p0} \cos \beta z \right) \right]$$

(II-32)

By comparison to Eq. (II-25), this result is seen to be identical to that for a fast diode with a saturation current  $I_s$  of

$$I_s = \frac{q p_{n0}}{\pi} \sqrt{\frac{2\omega D_p}{3}} . \quad (II-33)$$

Thus, the fast diode model holds for the slow charging of p-n junction diodes, with  $I_s$  given by Eq. (II-33). For a typical value of  $N_D = 4.6 \times 10^{14}/\text{cm}^3$ ,  $p_{n0} = 5.6 \times 10^5/\text{cm}^3$  with  $\omega = 6.28 \times 10^8 \text{ sec}^{-1}$ ,  $D_p = 20 \text{ cm}^2/\text{sec}$ , we find  $I_s = 2.6 \times 10^{-9} \text{ amps/cm}^2$ . This is about 100 times smaller than the  $I_s$  for PtSi Schottky diode.

#### (e) The Effect of Conductive Overlays

An overlay may be modeled as a capacitance in parallel with the diode depletion layer capacitor. This will not change the qualitative form of the above results, since the overlay can only increase the diode capacity.

#### 4. Reading

The various modes for reading the stored charge pattern are now considered. In all cases, we find the device output power in terms of the readout signal amplitude and the readout charge  $Q_R$ . We first deal

with acoustic-to-plate reading, where the output appears at the plate in response to an acoustic readout signal. We then analyze plate-to-acoustic reading, where the output appears at one of the acoustic ports in response to an rf plate readout signal. Finally, the analysis of both readout modes is modified for the case of overlay diodes. The conduction current is assumed to be negligible, so that the analysis is equally valid for fast and pn junction diodes.

(a) Acoustic-to-plate Reading

Here the readout signal is a surface wave propagating under the diode array and the output power is measured across a load resistor connected to the plate. The circuit model used to calculate the coupling of the surface wave potential  $\phi_{ar}$  to the diode surface is exactly that used in the writing analysis, Fig. II-1. Now, however, we consider only diode displacement current. The charge stored during the writing process will reverse bias the diode, so that only a very strong readout potential  $\phi_{ar}$  will give rise to a flow of conduction current. We may parenthetically note that, since conduction current does not flow, the readout signal does not affect the stored charge, and the readout process is nondestructive.

By the voltage divider relation, the diode voltage  $V_D$  is

$$V_D = \frac{C_a}{C_a + C_D} \phi_{ar} \quad . \quad (II-34)$$

The total diode charge  $Q_S$  deposited during writing may be written as



$$Q_S = Q_0 + Q_R \sin(\omega t_p + \beta z) \quad (\text{II-35})$$

where the second term on the RHS is the spatially varying component of the stored charge, as found in the previous section, and  $Q_0$  is all remaining stored charge.  $Q_0$  will bias the diode, but lacks the spatial periodicity required to contribute to the readout.

Combining Eqs. (II-35) and (II-5), the diode capacitance  $C_D$  is written in terms of the charge  $Q_R$  as

$$C_D = \frac{Q_0 + Q_R \sin(\beta z + \omega t_p) - C_{D0} V_B}{(V_D - V_B)} \quad (\text{II-36})$$

Substituting Eq. (II-36) into (II-34) and expanding, assuming  $Q_R/(V_D - V_B)$  is small compared to the other terms, yields the component of diode voltage due to the product  $Q_R \sin(\beta z + \omega t_p) \times \phi_{ar}$ ,  $V_{Dr}$ , to be

$$V_{Dr} = \frac{C_a}{(C_a + C_D)^2} \frac{\phi_{ar} Q_R \sin(\beta z + \omega t_p)}{(V_D - V_B)} \quad (\text{II-37})$$

The acoustic reading signal potential  $\phi_{ar}$  varies as  $e^{j(\omega t - \beta z)}$ , so that a component of the diode reading voltage  $V_{Dr}$  appears as an rf potential with wavenumber  $\beta = 0$ .

The voltage developed across each diode couples to the external load resistor  $R_L$  through the plate circuit coupling capacitor  $C_p$ , as shown in Fig. II-4. The current through the  $n^{\text{th}}$  element of the diode array,  $I_n$ , is

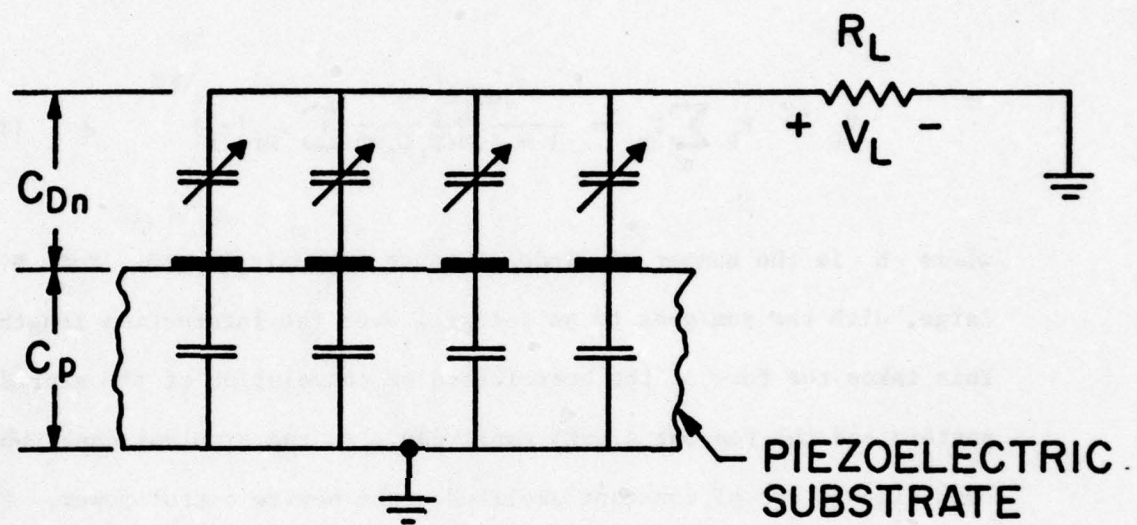


FIG. II-4. Acoustic-to-Plate Reading Circuit Model.

$$I_n = C_p \frac{d}{dt} (V_{Drn} - V_L) = j\omega C_p (V_{Drn} - V_L) \quad (\text{II-38})$$

where  $V_{Drn}$  is the voltage drop across the  $n^{\text{th}}$  diode and  $V_L$  is the voltage drop across the load resistor  $R_L$ . Thus,  $V_L$  is given by

$$V_L = R_L \sum_n I_n = \frac{j\omega R_L C_p w\delta}{1 + j\omega N R_L C_p w\delta} \sum V_{Dr}(z_n) \quad (\text{II-39})$$

where  $N$  is the number of diode elements per unit length. For  $N$  large, with the sum goes to an integral over the interaction length,  $L$ . This takes the form of the correlation or convolution of the stored charge pattern and the readout signal amplitude. In the simplest case, where both signals are of constant amplitude, the device output power,  $P_0$ , is

$$P_0 = \frac{V_0^2}{2R_L} = \frac{1}{4R_L} \left[ \frac{(\omega N L C_p R_L w\delta)^2}{1 + (\omega N L C_p R_L w\delta)^2} \right] \left[ \frac{C_a}{(C_a + C_D)^2} \frac{Q_R \phi_{ar}}{(V_B - V_D)} \right]^2 \quad (\text{II-40})$$

(b) Plate-to-acoustic Reading

Equation (II-9) gives the diode surface potential due to an applied plate reading signal of the form  $\phi_{pr} \sin \omega t$ . It is convenient to rewrite this equation in terms of the forward and backward propagating acoustic surface wave components,  $V_{Dr}^{\pm}$ , of form

$$V_{Dr}^{\pm} = \frac{C_p}{2C_{D0}^2 V_B} \phi_{pr} Q_R e^{j(\omega t + \beta z_n)} \quad (\text{II-41})$$



Here,  $Q_R$  is the modulation of the stored charge pattern, given by

$$Q_R = C_a V_{a0} \quad \text{for fully charged diodes, as in Eq. (II-9).}$$

The amplitude of the surface wave excited by the diode surface potential  $V_{Dr}^+$  is found using the normal mode theory of Kino and Auld.<sup>57</sup> From Eq. (II-31) of this reference it may be shown that

$$\frac{\partial a}{\partial z} + j\beta^* a = \frac{j\omega\rho_s\phi_1^* w}{4P_1} \quad (\text{II-42})$$

where  $w$  is the acoustic beam width,  $\rho_s$  is the semiconductor surface charge, and the rf potential due to the propagating acoustic wave is  $\phi_a = a\phi_1$  where  $P_1 = \phi_1^* \phi_1 / 2Z_a$ .  $P_1$  is the power per unit width of the surface wave and  $Z_a$ , the acoustic impedance, is defined in Eq. (A2).

The total rf potential is  $\phi = \phi_a + \phi_s$ , where  $\phi_s$  is the sum of the contributions other than the fundamental acoustic surface wave mode. Kino and Reeder<sup>58</sup> define the relationship between  $\phi_s$ ,  $\rho_s$ , and the acoustic coupling capacitor  $C_a$  as

$$\phi_s = \rho_s / C_a. \quad (\text{II-43})$$

Equation (II-42) now reduces to

$$\frac{\partial \phi_a}{\partial z} + j(\beta + \gamma)\phi_a = j\gamma\phi, \quad (\text{II-44})$$

where

$$\gamma = \frac{\omega w C_a Z_a}{2} \quad (\text{II-45})$$

represents the perturbation on the surface wave propagation constant  $\beta$  due to the presence of the diode array. Assuming a solution to Eq. (II-44) of the form

$$\phi_a(z') = \phi_a e^{-j(\beta + \gamma)(z' + z)} \quad (\text{II-46})$$

we see that Eq. (II-44) may be integrated to give the potential of the fundamental acoustic mode:

$$\phi_a(z, \omega) = j\gamma \int \phi_a e^{j(\beta + \gamma)(z' + z)} dz' \quad (\text{II-47})$$

By Fourier transforming Eq. (II-47) assuming the propagation constant perturbation  $\gamma$  is constant in frequency, the potential  $\phi_a$  as a function of time is seen to be of the form

$$\phi_a(z, t) = j\gamma e^{j\gamma z} \int \phi\left(z', t - \frac{z' + z}{z_a}\right) e^{j\gamma z'} dz' \quad (\text{II-48})$$

By direct substitution into Eq. (II-48), it is possible to show that the device output is either the correlation or convolution of the modulations of the stored charge pattern and the reading signal. This is done in Chapter IV.

The reading potential at the surface of each diode element,  $V_{Dr}^+$ , is not continuous. By Floquet's theorem,<sup>59</sup> the continuous form is

$$V_{Dr}^+(z_n) = e^{-j\beta z} V(z) \quad (\text{II-49})$$

where

$$V(z) = \left(\frac{\delta}{\ell}\right) V_{Dr0} \sum_{n=-\infty}^{\infty} \sin\left(\frac{\pi n \delta}{\ell}\right) e^{j(2\pi n/\ell)[z + \delta]} \quad (II-50)$$

$\delta/\ell$  is the ratio of diode element width to the periodicity of the diode array. Retaining only the  $n = 0$  term of Eq. (II-50) yields the result

$$V_{Dr}^{\pm}(z, t) \approx \phi(z, t) \approx \frac{\delta}{\ell} V_{Dr0} e^{-j\beta z} e^{\pm j\omega t} \quad (II-51)$$

If it is assumed that the original acoustic surface wave was perturbed by the presence of the semiconductor, so that its wavenumber was  $\beta + \gamma$  (cf. Appendix C), then Eq. (II-48) yields the potential of the excited acoustic surface wave to be

$$\phi_a = j\gamma e^{-j\gamma z} (\delta/\ell) \int V_{Dr0} e^{j(\omega t - \beta z)} dz = j\gamma (\delta/\ell) V_{Dr0} L e^{-j\gamma z} e^{j(\omega t - \beta z)} \quad (II-52)$$

The output power is  $\phi_a^* \phi_a / 2Z_a$ , so that by combining Eqs. (II-52) and (II-41), the device output power  $P_0$  for a constant amplitude rf plate readout signal  $\phi_{pr}$  and stored readout charge  $Q_R$ , with an interaction region length  $L$ , is found to be

$$P_0 = \frac{1}{2Z_a} \left[ \frac{\gamma L \delta}{\ell} \right]^2 \left[ \frac{C_p \phi_{pr} Q_R}{2C_{D0}^2 V_B} \operatorname{sinc} \frac{\beta \delta}{2} \right]^2 \quad (II-53)$$



(c) Reading With Overlay Diodes

Finally, we consider the effect of conductive overlays on the above results. Overlays are in general used to increase the effective area of the diodes by making ohmic contact to the diodes themselves while covering, and hence shielding, a large part of the adjacent semiconductor area. A thin insulating layer of  $\text{SiO}_2$  separates the overlap from the semiconductor surface, so that a large MOS capacitor appears in parallel with the diode capacity  $C_D$ . Thermally oxidized Si is often accumulated at the surface, and with typical flatband voltage shifts  $\sim 1.5$  volts, the MOS overlay capacitance will nearly equal the  $\text{SiO}_2$  capacitance for most levels of reading signals. If this is not the case, the overlay itself will contribute to the readout signal, and analytic results are not easily obtained.

Changes in the readout analysis arise because most of the stored charge resides in the static overlay capacitor, where it cannot contribute to the readout. In both cases,  $C_{ov} + C_D \gg C_p$  or  $C_a$  where  $C_{ov}$  is the overlay capacity, so that the diode voltage is

$$V_D \approx \frac{C_{a/p}}{C_{ov} + C_D} \phi(ar/pr) \approx \frac{C_{a/p}}{C_{ov}} \left( 1 + \frac{C_D}{C_{ov}} \right) \phi(ar/pr) . \quad (II-54)$$

The fraction of the readout charge  $Q_R$  residing in the diode capacity  $C_D$ ,  $Q_{RD}$ , is

$$Q_{RD} = \frac{A}{A_D} \left[ \frac{C_D(V_D - V_B) + C_{D0}V_B}{C_{ov}V_D} \right] Q_R , \quad (II-55)$$

where  $A$  is the overlay area and  $A_D$  is the diode area. Substituting the diode capacitance  $C_D$  in the form of Eq. (II-36) gives  $V_{Dr}$ , the component of diode voltage contributing to the readout

$$V_{Dr} = \frac{C_{(a/p)} [C_D (V_D - V_B) + C_{D0} V_B]}{C_{ov}^3 V_D (V_D - V_B)} Q_R \phi_{(ar/pr)} \quad (II-56)$$

Combining Eq. (II-56) with the earlier analysis, the output power for acoustic-to-plate reading is

$$P_0 = \frac{1}{4R_L} \left[ \frac{(\omega N L C_P R_L w \delta)^2}{1 + (\omega N L C_P R_L w \delta)^2} \right] \left[ \frac{C_a [C_D (V_D - V_B) + C_{D0} V_B]}{C_{ov}^3 V_D (V_D - V_B)} Q_R \phi_{ar} \right]^2 \quad (II-57)$$

The output power for plate-to-acoustic reading is:

$$P_0 = \frac{1}{2Z_a} \left[ \frac{\gamma L \delta}{\ell} \right]^2 \left[ \frac{C_P [C_D (V_D - V_B) + C_{D0} V_B]}{C_{ov}^3 V_D (V_D - V_B)} Q_R \phi_{pr} \operatorname{sinc} \frac{\beta \delta}{2} \right]^2 \quad (II-58)$$

## 5. Comparison to Experiment

We now consider experimental verification of the theory. Table II summarizes the various writing and reading modes and device structures used in the experiments. The  $p^+n$  junction diode results were obtained in our own laboratory. The Schottky diode results have been previously reported by Ingebrigtsen.<sup>13</sup>

Figure 2-5 shows the two diode structures; in both cases interactions from the interdiode region are minimized. In the mesa structure of

Fig.II-5(a), this region has simply been etched away. Such a structure also provides excellent isolation between adjacent diodes and is a good realization of an array of one-dimensional pn junctions.

The conductive overlays, shown in Fig.II-5(b), shield the interdiode region from surface wave fields. As discussed earlier, such overlays put a large MOS capacitor in parallel with the diode. When the silicon surface is accumulated, this capacitor is static and does not contribute to writing or reading. The flatband voltage shift for the particular device discussed here is  $\sim 1.5$  volts.<sup>6</sup> Thus, the overlay capacitor is always static in writing, and only contributes to readout for high levels of either the readout signal or reverse bias diode voltage due to the stored charge.

(a) p<sup>+</sup>n Junction Diodes, Acoustic-Plate Writing with a Single Pulse, Plate-to-Acoustic Reading

Figure 2-6 shows the output power as a function of plate pulse height for the device whose parameters are summarized in Table II, column 1. The theoretical output is also plotted with no adjustment of parameters, beginning at the theoretical turn-on voltage,  $V_{on}$ . The fast diode model was employed in conjunction with a - 2.5 dB correlation due to the use of p<sup>+</sup>n diodes, as follows from Eq. (II-22).

The output power climbs rapidly and then saturates near the predicted turn-on voltage,  $V_{on}$ . The theory accurately predicts both  $V_{on}$  and the output power.

We have also observed the turn-on voltage  $V_{on}$  to be independent of temperature.<sup>22</sup> This, too, is consistent with the predicted diode



## DIODE STRUCTURES

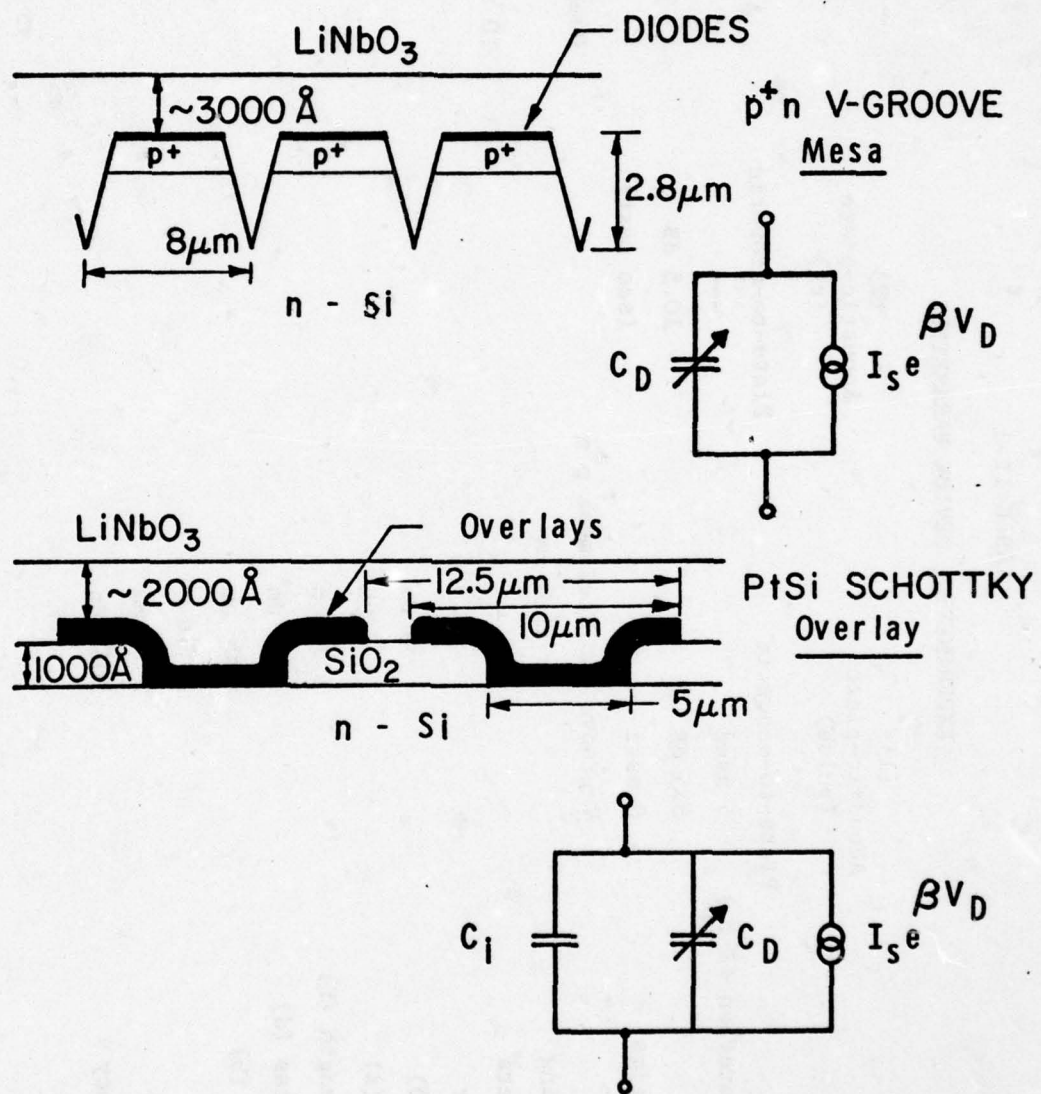


FIG. II-5 Diode Array Structures.

TABLE II-1

## EXPERIMENTAL DEVICE PARAMETERS

	(1) Acoustic-plate (pulse)	(2) Acoustic-plate (rf)	(3) Acoustic-plate (pulse)
Writing:			
Reading:			
Plate pulse duration ( $2 t_p$ )	5 nsec	---	5 nsec
One way loss	8.5 dB	10.5 dB	8 dB (assumed)
3 dB storage time	8 msec	(see text)	~ 20 msec
Diodes	V-groove isolated mesa $p^+n$		Overlay PtSi Schottky
Substrate doping	~ 11 $\Omega$ -cm		34 $\Omega$ -cm
Overlay contacts	---		10 $\times$ 10 $\mu$ m Cr/Au
Diode diameter	---		5 $\mu$ m
Diode width ( $\delta$ )	4 $\mu$ m		---
Diode period ( $\ell$ )	8 $\mu$ m		12.5 $\mu$ m
Interaction length (L)	1.57 cm		0.44 cm
LiNbO <sub>3</sub> thickness (d)	450 $\mu$ m		710 $\mu$ m
Airgap height (h)	300 nm		200 nm
Airgap spacer	rails		posts
Beam Width (w)	1 mm		2.75 mm
Center frequency	108 MHz		65 MHz

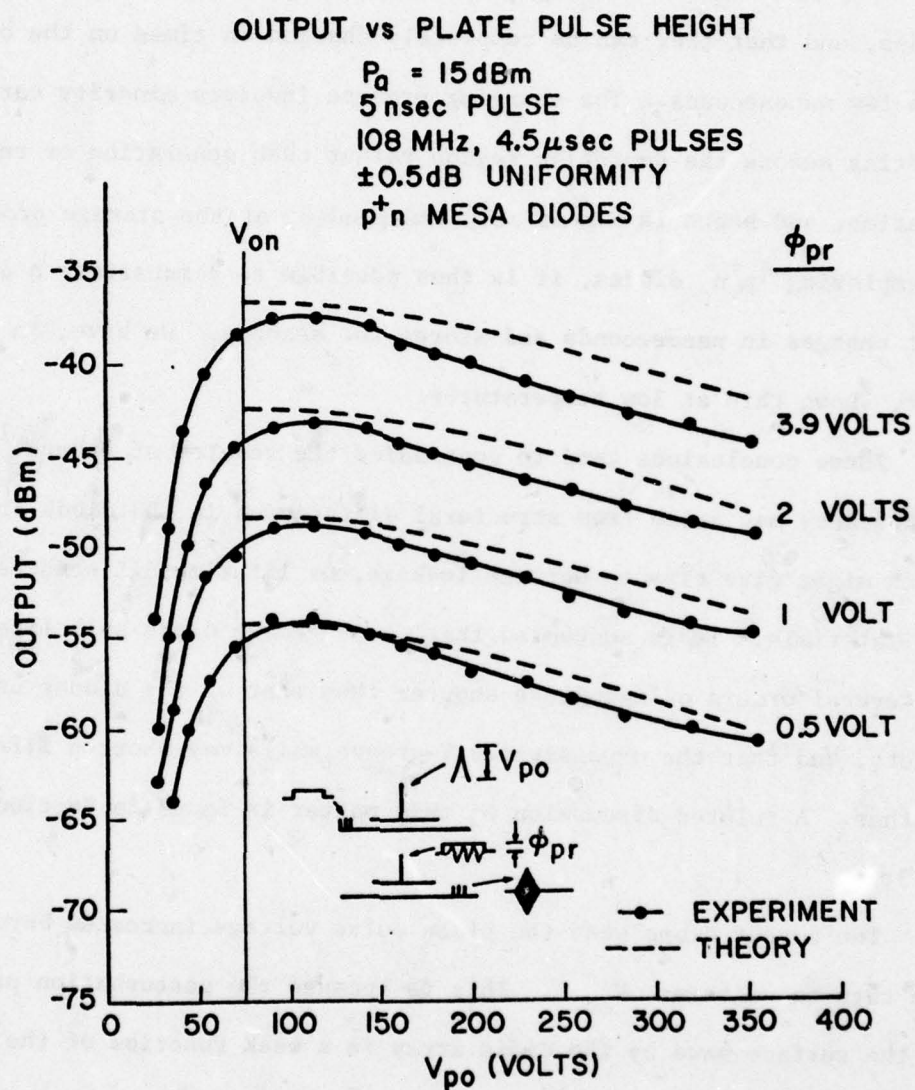


FIG. II-6 Device Output vs. Plate Pulse Height for  $p^+n$  Mesa Diode Structure, Experiment and Theory.



voltage  $V_D$  given in Eq. (II-21), since  $1/p_{n0} \sim n_i^2 \exp(E_g/kT)$ , where  $n_i$  is the intrinsic carrier concentration and  $E_g$  is the bandgap energy.

It thus appears that our  $p^+n$  diodes perform very much like fast diodes, and that they can be completely charged in times on the order of a few nanoseconds. The charging process involves minority carriers drifting across the depletion region rather than generation or recombination, and hence is essentially independent of the storage process. By employing  $p^+n$  diodes, it is thus possible to demonstrate a device that charges in nanoseconds and stores for seconds. We have, in fact, shown this at low temperatures.

These conclusions tend to contradict the results of others.<sup>19</sup> The discrepancy may arise from structural differences in the diode arrays, which might give rise to surface leakage, or lifetime differences in the materials. It is suspected that the V-groove diode bulk lifetime is several orders of magnitude shorter than that of the diodes used by others, and that the unpassivated V-groove walls may shorten lifetime further. A related discussion of this matter is found in Section II-3(b)

The output drops when the plate pulse voltage increases beyond the turn-on voltage  $V_{on}$ . This is because the perturbation presented to the surface wave by the diode array is a weak function of the diode capacity, and, hence, stored charge. Thus, the surface wave propagation constant differs for the writing and reading processes. The resultant phase mismatch reduces the correlation output. The effect

is discussed in more detail in Appendix C. Propagation loss is experimentally observed to increase slightly with respect to stored charge, accounting for about 1 dB additional loss for a plate pulse voltage  $V_{p0}$  of 350 volts. Both the calculated phase mismatch and empirically observed propagation loss effects have been added to the theoretical curves of Fig. II-6.

Figure II-7 shows the output power as a function of the readout signal voltage for various levels of the input acoustic power,  $P_a$ . Agreement is good until  $P_a$  reaches 25 dBm, when saturation effects occur. The thermal noise floor is  $\sim -90$  dBm, so that the predicted linear dynamic range at the output with respect to the readout signal is  $\sim 60$  dB. The experiment verifies  $\sim 35$  dB of this. The bottom 25 dB are lost due to amplifier feedthrough noise that could be gated out.

(b) Overlay PtSi Schottky Diodes, Acoustic-Plate Writing with a Single Pulse, Acoustic-to-Plate Reading

Figures II-8 and II-9 show the dependence of the output power on the writing and reading acoustic signal powers for the device whose parameters are summarized in Table II, column 3. Here, the fast diode model alone was used. The only adjustable parameter was the insertion loss, which had not been reported. A one-way loss of 8 dB was assumed.

The theory and experiment diverge for writing signal powers  $\geq 30$  dBm. At these levels, the acoustic potential becomes appreciable compared to the plate pulse amplitude and the small acoustic signal assumption breaks

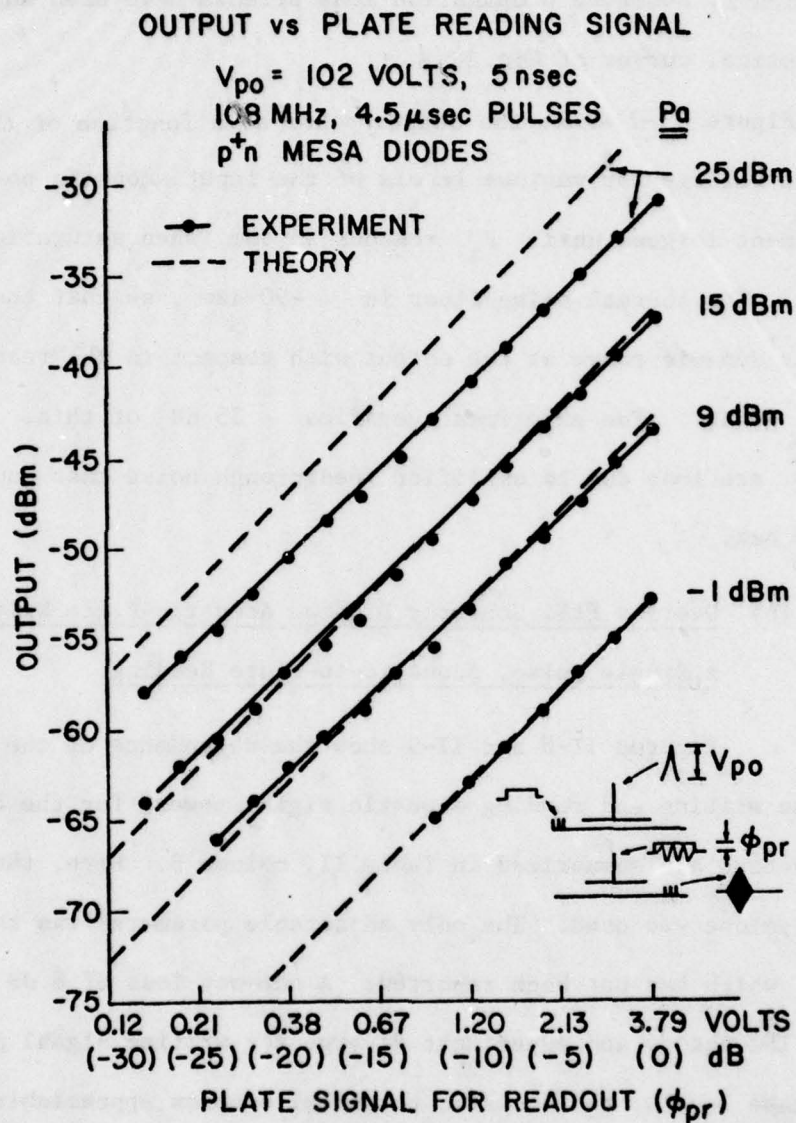


FIG. II-7 Device Output vs. Plate Reading Signal Amplitude for the  $p^+n$  Mesa Diode Structure with Pulse Writing, Theory and Experiment.



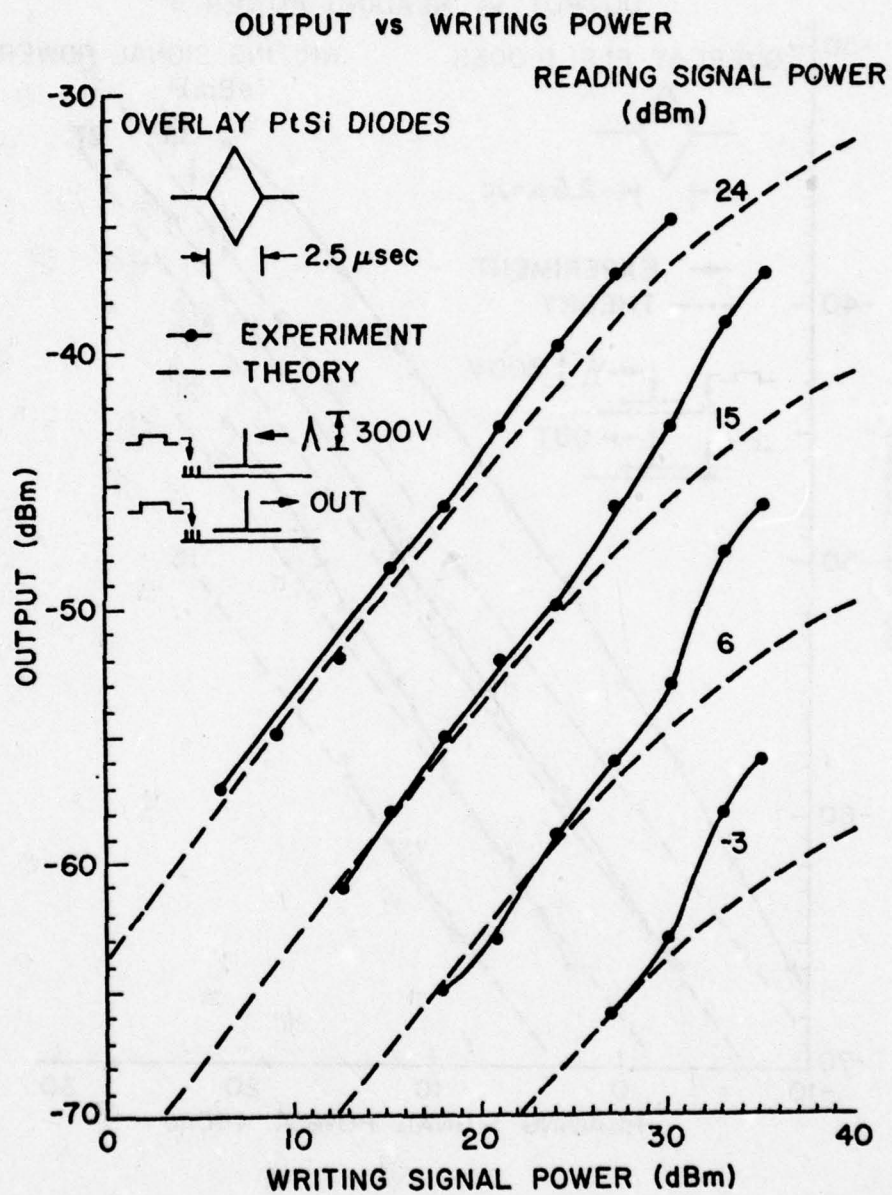


FIG. II-8 Device Output vs. Writing Power for the Overlay Schottky Diode Structure, Theory and Experiment.

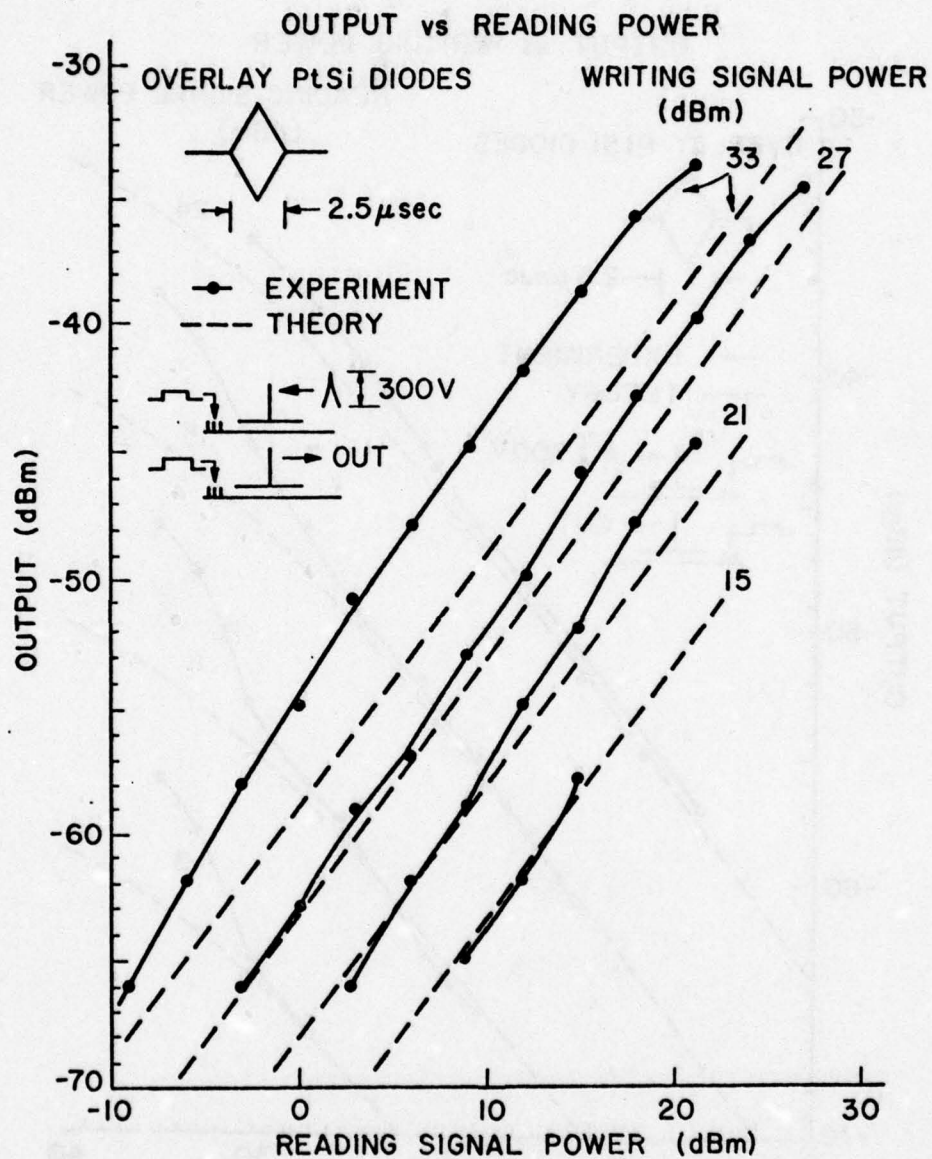


FIG. II-9 Device Output vs. Reading Power for the Overlay Schottky Diode Structure, Theory and Experiment.

down. Such large acoustic potentials may also give rise to interdiode currents. While the result of such effects is not easily predictable, we expect them to cause a breakdown of our theory.

The divergence of theory and experiment for reading signal powers  $\geq 10$  dBm may be due to output contributions from the MOS overlays. This would increase the output, as is observed.

(c) p<sup>+</sup>n Diodes, Acoustic-Plate Writing with rf Signals,  
Plate-to-Acoustic Reading

Figures II-10 and II-11 show the output power as a function of acoustic writing pulse length, and, hence, charging time, for devices whose parameters are summarized in Table II, column 2. The device used to obtain Fig. II-10 had an unpassivated V-groove mesa diode array with a relatively short 3 dB storage time of only 600  $\mu$ sec. This was probably due to surface contamination on the walls of the V-grooves. The presence of short lifetime surface recombination centers will also contribute to the diode charging currents.

Theoretical predictions with an assumed saturation current  $I_s = 1.7 \times 10^{-6}$  a/cm<sup>2</sup> give a good fit to the observed characteristics for acoustic powers  $\leq 17$  dBm. Above this power level, the assumptions of constant diode capacity and slow charging break down.

Also shown in the time when the linear approximation to the stored charge, given by Eq. (II-28), becomes inaccurate. This occurs at an output power  $P_0 \sim -55$  dBm, about 40 dBm above the thermal noise floor. Over this range, it would be possible to linearly correlate input signals during the writing process.<sup>16,60</sup>



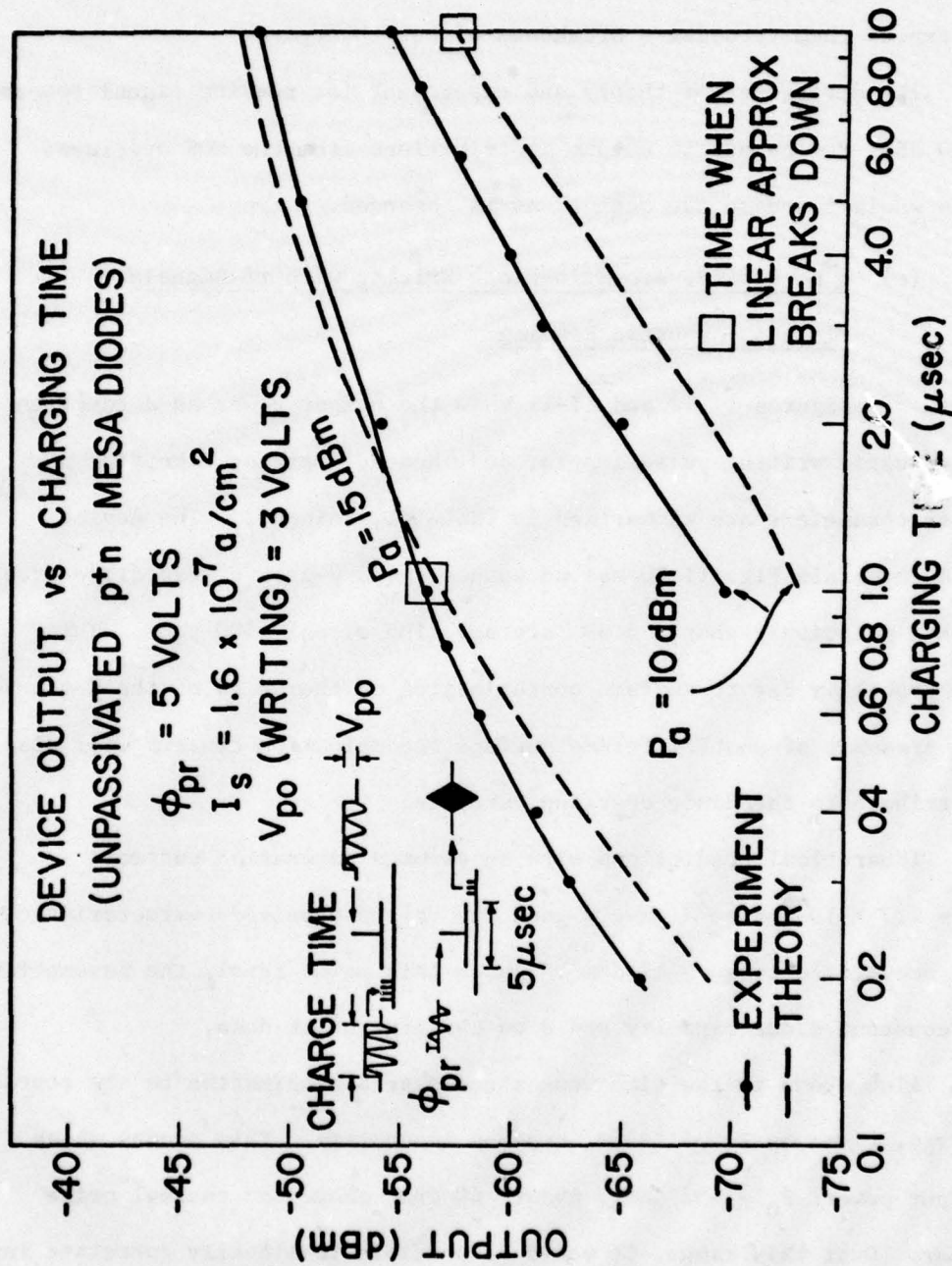


FIG. II-10 Device Output vs. Charging Time for Unpassivated p<sup>+</sup>n Mosa Diodes, Theory and Experiment.

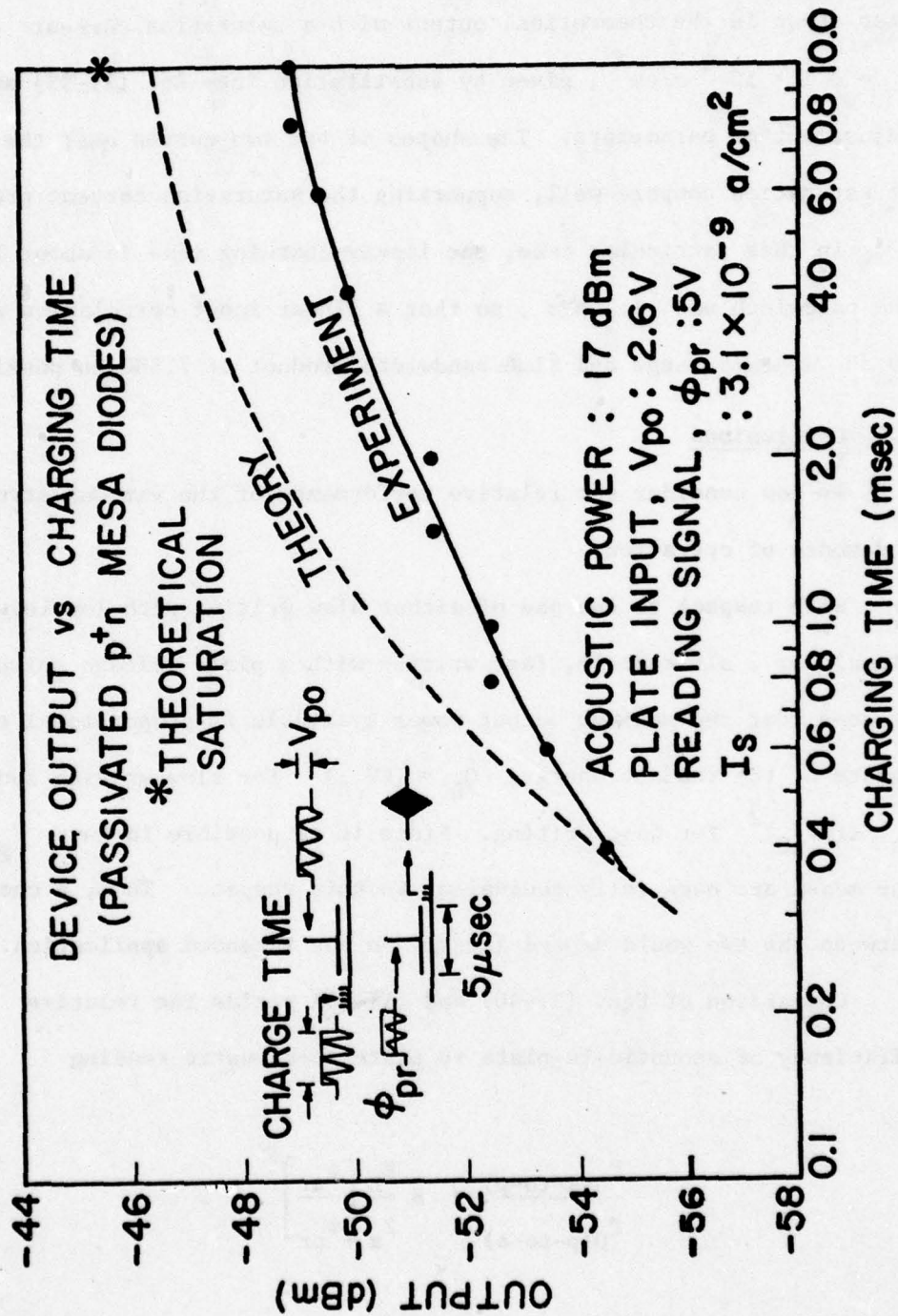


FIG. II-11 Device Output vs. Charging Time for Passivated p<sup>+</sup>n Mesa Diodes, Theory and Experiment.

The device used to obtain Fig. II-11 had a  $\text{SiO}_2$  passivated V-groove mesa diode array with a 3 dB storage time of 35 msec. Also shown in the theoretical output with a saturation current  $I_s = 3.1 \times 10^{-9} \text{ a/cm}^2$ , given by substitution into Eq. (II-33) and no adjustment of parameters. The shapes of the two curves near the onset of saturation compare well, supporting the saturation current prediction.

In this particular case, the linear charging time is about 1 msec. The bandwidth was 7.3 MHz, so that a linear input correlation with a 40 dB dynamic range and time-bandwidth product of 7,300 is possible.

## 6. Conclusions

We now consider the relative performance of the various structures and modes of operation.

With respect to the use of either slow writing with low level rf signals or, alternately, fast writing with a plate voltage spike, it is seen that the maximum output power available is proportional to the square of the readout charge,  $Q_D \propto (CV_{p0})^2$  for slow writing and  $Q_R \propto (CV_{a0})^2$  for fast writing. Since it is possible to have  $V_{p0} \approx V_{a0}$ , the modes are essentially equivalent in this respect. Thus, a choice between the two would depend largely on the intended application.

Comparison of Eqs. (II-40) and (II-53) yields the relative efficiency of acoustic-to-plate vs plate-to-acoustic reading

$$\frac{P_{0(a\text{-to-p})}}{P_{0(p\text{-to-a})}} = 8 \frac{R_L}{Z_a} \left[ \frac{\phi_{ar}}{\phi_{pr}} \right]^2 \quad (\text{II-59})$$



Comparison of Eqs. (II-57) and (II-58) yields the same result for overlay diodes.

Typically,  $Z_a > R_L$ . Because of the onset of nonlinear response both in the piezoelectric substrate and the semiconductor, the maximum acoustic reading signal amplitude  $\phi_{ar}$  is typically an order of magnitude lower than the maximum plate reading signal amplitude  $\phi_{pr}$ . Furthermore, the plate electrode presents a capacitive load. It is thus possible to obtain a large plate reading signal amplitude with external matching while retaining a bandwidth comparable to the transducer limited bandwidth of an acoustic reading signal. For these reasons, plate-to-acoustic reading is more efficient, although once again, specific design constraints may dictate the choice of reading mode.

Overlays increase the storage time by decreasing the leakage current per unit area. They also enhance efficiency by increasing the effective diode array area. However, a considerable reduction in reading efficiency arises because the readout charge stored in the static overlay capacity cannot contribute to readout. In practice, low leakage, high density p-n diode arrays can offer long storage times and good coverage of the array area without the need of large area overlays. Surface leakage and isolation problems may be averted either through the use of a mesa structure or small area junction shielding overlays.

The performance of p-n junction and Schottky diodes is seen to be essentially equivalent for writing with a plate voltage spike. The significantly lower reverse leakage current allows a p-n diode array to

store a signal for a far longer time. Thus, p-n diodes offer a larger ratio of storage to writing time. We have experimentally demonstrated and reported this elsewhere.<sup>13</sup>

With low level signals, p<sup>+</sup>n diodes can be charged over longer periods due to their lower saturation current  $I_s$ . This is of value in performing correlations during the writing process.<sup>16,60</sup>

Finally, we compare the storage correlator to the acoustoelectric convolver.<sup>27</sup> The convolver is essentially a storage correlator without storage. Both devices have the same structure; the convolver provides a real time convolution of two opposite traveling acoustic surface waves. It has been conjectured that the two devices have equivalent efficiencies. This may be confirmed by defining an efficiency  $\mathcal{M}_{sc}$  for acoustic-to-plate reading:

$$\mathcal{M}_{sc} = \frac{wV_L}{\sqrt{2P_{aw}P_{ar}}} = \frac{wZ_a}{\sqrt{2}} \left( \frac{C_a}{C_a + C_D} \right)^2 \frac{\text{sinc}^2(\beta\delta/2)}{(V_B - V_D)} \quad (\text{II-60})$$

where a value of the load resistor  $R_L$  is assumed that gives the peak output power,  $R_L = (\omega NLC_p w\delta)^{-1}$ , the readout charge is  $Q_R = C_a V_a$ , the acoustic writing potential  $V_a = \sqrt{2Z_a P_{aw}}$ , and the acoustic reading potential  $\phi_{ar} = \sqrt{2Z_a P_{ar}}$ , so that  $P_{aw}$  and  $P_{ar}$  are the powers of the acoustic writing and reading signals, respectively. An equivalent efficiency for the convolver,  $\mathcal{M}_c$ , has been shown by Joly<sup>27</sup> to be given by the relation

$$\mathcal{M}_c = \frac{wV_0}{\sqrt{2P_{a1}P_{a2}}} = \frac{wZ_a}{2\sqrt{2}} \cdot \frac{(C_a/C_{D0})^2}{\left[1 + (C_a/C_D)\right]^3} \cdot \frac{\text{sinc}^2(\beta\delta/2)}{V_B} \quad (\text{II-61})$$

where  $P_{a1}$  and  $P_{a2}$  are the powers of the two opposite propagating acoustic surface waves and  $V_0$  is the device output voltage. Equations (II-60) and (II-61) give

$$\frac{\mathcal{M}_{sc}}{\mathcal{M}_c} = 2 \left[ 1 + \frac{C_a}{C_D} \right] \quad (\text{II-62})$$

Usually,  $C_D \gg C_a$ , so the efficiency of the correlator is essentially 6 dB better than that of the convolver.



## CHAPTER III

### DESIGN AND FABRICATION

#### 1. Introduction

We now discuss the design and fabrication of a storage correlator. The device is physically identical to a diode acoustoelectric convolver, so that the convolver structure designed and built by Joly<sup>27</sup> served as a convenient starting point.

This structure is shown in Fig. III-1. On the bottom is a gold plated sapphire substrate. This serves as a ground plane. Its dimensions are 20 mils  $\times$  3.5 mm  $\times$  2.5 cm. The YZ-LiNbO<sub>3</sub> delay line rests directly above the sapphire substrate. Its dimensions are  $\leq$  20 mils  $\times$  3.5 mm  $\times$  3.5 cm. At each end, spaced by 3 cm, are interdigital transducers used to launch acoustic surface waves. A set of nine 4  $\mu$ m wide, 2.5 cm long spacer rails are sputter etched into the central region to maintain a uniform airgap between the diode array and the LiNbO<sub>3</sub> surface.

The diode array rests directly on the spacer rails. Its back side is gold coated to ensure good electrical contact. The output contact fits directly behind the diode array, and a silicone rubber spacer provides the pressure required to hold the structure tightly together.

The convolver is housed in a gold plated carrier box that screws into a larger aluminum box containing the transducer and plate matching networks. The entire assembly is shown in Fig. III-2.

The Stanford Integrated Circuit Laboratories' processing facilities were used to fabricate a number of alternate diode array structures.

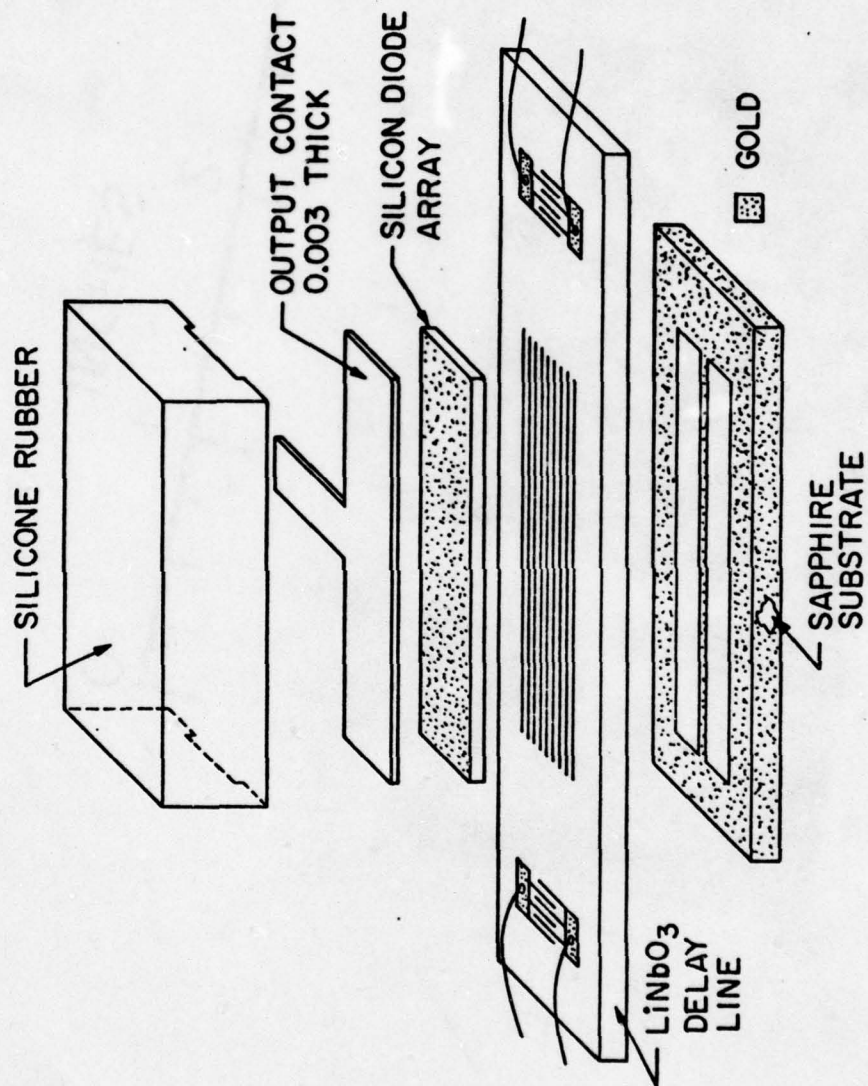


FIG. III-1 Correlator Packaging

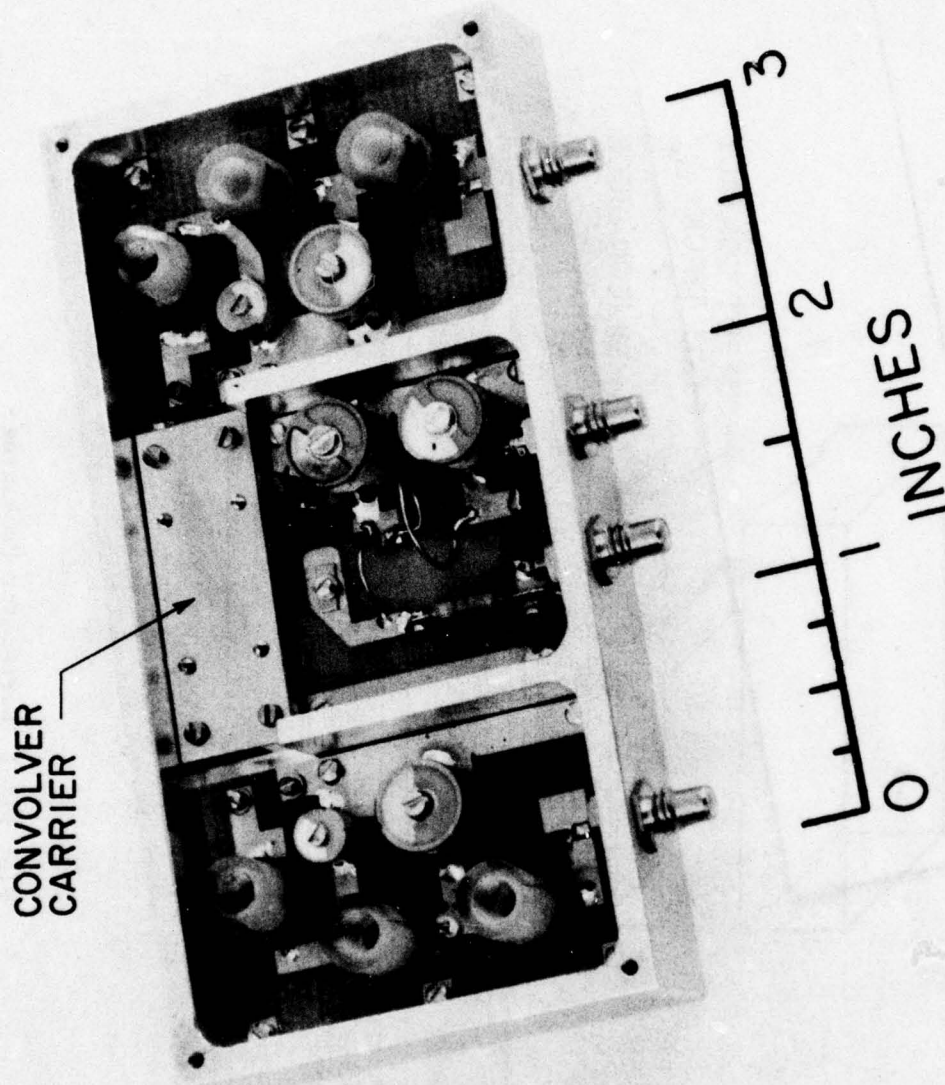


FIG. III-2. Device mounted in carrier box with matching networks.



These are described in Section 2 of this chapter. Their relative performance is evaluated from the standpoints of experimentally observed performance and the relative ease of fabrication and assembly into the Joly convolver structure.

During the reading process, the high level reading signal and low level output signal both appear at essentially the same frequency. Consequently, the storage correlator is particularly prone to spurious signal feedthrough. This is not the case with the acoustoelectric convolver, because of the different input and output frequencies; so that Joly's structure required major modification to reduce the problem.

Two feedthrough components are seen. A fast one is due to direct rf coupling of the reading signal to the readout port. A slow one is due to the generation of spurious acoustic waves during reading. Techniques for the reduction of both components are discussed in Section 3. Finally, some comments are made about processing of the spacer rail structure.

A broadband matching network and a high voltage pulser were required for many of the experiments described in Chapters II and IV. The design and performance of these circuits are discussed in Section 4.

## 2. Diode Arrays

This section first summarizes the diode array design criteria. The various arrays that have been constructed are then described and compared.

(a) Array Design Criteria

i. Density: The Nyquist sampling theorem places a constraint on the minimum diode density.<sup>46</sup> Specifically, if the bandwidth of the modulation of the signal to be stored is B, then there must be at least two diodes in a length  $v_a B$ , where  $v_a$  is the acoustic propagation velocity. Additionally, because the device output is proportional to the ratio of the diode width to period, diodes should cover the largest possible array surface area.

ii. Isolation: A stored charge pattern gives rise to interdiode potentials. Without adequate isolation, interdiode currents may destroy any spatially varying charge pattern.

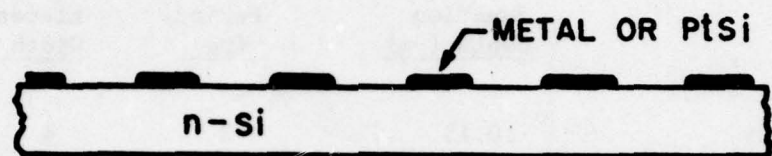
iii. Uniformity: For good signal processing performance, the array must be uniform over its full length, without macroscopic defects or variation in diode characteristics. The silicon wafer itself must be flat and undistorted. In practice, this necessitates low temperature processing.

iv. Storage Time: The storage time, as dictated by the reverse leakage current, must be adequate for the intended signal processing application. This is discussed in Chapter IV. In most cases, the maximum required storage time is in the 10 - 100 msec range.

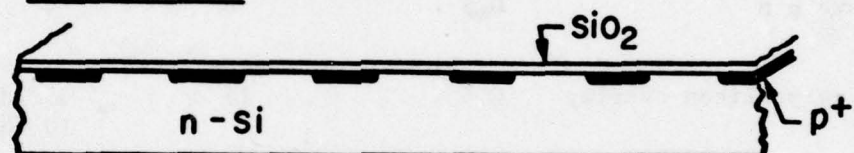
(b) Summary of Structures

The various diode array structures are summarized below and in Fig. III-3. Table III-1 summarizes the array dimensions. Appendix D gives the process schedules.

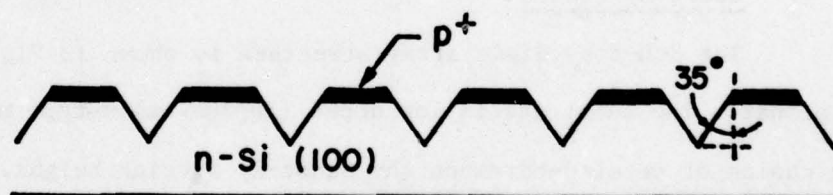
(a) SCHOTTKY



(b) PLANAR  $p^+n$



(c) V-GROOVE



(d) OVERLAY

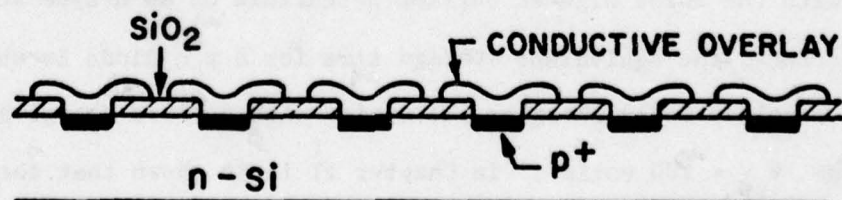


FIG. III-3 Diode Array Structures



TABLE III-1

## DIODE ARRAY DIMENSIONS

<u>Array</u>	<u>Junction Depth (<math>\mu\text{m}</math>)</u>	<u>Period (<math>\mu\text{m}</math>)</u>	<u>Element Width</u>
PtSi Schottky	0.15	8	4
$p^+n$ planar	0.5	8	4
V-groove $p^+n$	0.5	8	4
Doped polysilicon overlay	0.5	15	5 (diodes) 10 (overlays)

i. Schottky diodes

The Schottky diode array structure is shown in Fig. III-3(a).

It is a planar. The substrate is low doped ( $10\text{--}30\Omega\text{-cm}$ ) n-type material.

The choice of metal determines the Schottky barrier height, and hence, the reverse saturation current. Table III-2 shows the barrier height, reverse saturation current, and estimated storage time for the metals with the three highest barrier potentials on an n-type substrate. For reference, the equivalent storage time for a  $p^+n$  diode is shown. Here we consider fully charging the device with a plate charging pulse of amplitude  $V_{p0} = 100$  volts. In Chapter II it is shown that the stored charge is essentially  $C_p V_{p0}$ , where  $C_p$  is the plate coupling capacitance.

The leakage current is taken to be constant and equal to the Schottky barrier reverse saturation current. For the case of the  $p^+n$  diode, a constant reverse current due only to thermal generation of carriers in the depletion region, of the form  $qn_i w / \tau_p$  is assumed,<sup>40</sup> with values of  $C_p = 140 \text{ pf/cm}^2$ . An intrinsic carrier density of  $n_i = 1.6 \times 10^{10} / \text{cm}^2$ , a depletion layer width of  $w = 1 \text{ } \mu\text{m}$ , and a minority carrier time constant of  $\tau_p = 3 \text{ } \mu\text{sec}$ .

TABLE III-2

THEORETICAL LEAKAGE CURRENTS AND STORAGE TIMES

<u>Metal</u>	<u>Al</u>	<u>Au</u>	<u>PtSi</u>	<u><math>p^+n</math></u>
<u>Barrier height</u> 39(volts):	0.67	0.80	0.82	-
<u>Sat. current</u> (a/cm <sup>2</sup> , 298° K):	$6.2 \times 10^{-5}$	$4 \times 10^{-7}$	$2 \times 10^{-7}$	$3 \times 10^{-8}$
<u>Storage time</u> (msec):	0.23	34	70	162

As seen in Table III-2, the storage for Schottky diodes on silicon will in general be worse than that of  $p^+n$  junction diodes, and only sufficient for most purposes with either PtSi or Au.\*

\* Si doped Al Schottky diodes have been reported to yield barrier heights  $\geq 0.90$  volts.<sup>66</sup> This corresponds to saturated currents  $\sim 10^{-8} \text{ a/cm}$ , roughly equivalent to the  $p^+n$  diode.

Processes have been developed to fabricate Al , Au and PtSi on silicon Schottky diodes. These are summarized in Appendix D. The best observed forward and reverse characteristics for discrete devices fabricated in this manner as part of this work are shown in Fig. III-4 and Table III-3.

TABLE III-3

EXPERIMENTAL SCHOTTKY DIODE CHARACTERISTICS

	<u>Al/Si</u>	<u>Au/Si</u>	<u>PtSi/Si</u>
n:	1.07	1.08	1.07
$J_s$ (a/cm <sup>2</sup> ):	$2.4 \times 10^{-5}$	$2.2 \times 10^{-7}$	$1.8 \times 10^{-7}$
$\phi_{Bn}$ (V):	0.69	0.82	0.82

Key: n: The current is observed to vary as  $J_s (\exp(qV/nkT) - 1)$

$J_s$ :  $J_s = A^{**} T^2 \exp(-q\phi_{Bn}/kT)$  , with  $A^{**} = 120 \text{ a/cm}^2 \text{ } ^\circ\text{K}^2$  the <sup>39</sup> modified Richardson constant and a temperature  $T = 298^\circ \text{ K}$  .

$\phi_{Bn}$ : Barrier height, reproducible to within  $\phi_{Bn} = (\text{listed value} - 0.04\text{V})$

The fabrication process is extremely sensitive to contamination. Care must be taken to remove SiO<sub>2</sub> in the diode wells immediately before metallization. High quality junctions are readily fabricated with Pt on  $\geq 30 \Omega\text{-cm}$  material; results are less consistent for  $\leq 10 \Omega\text{-cm}$  substrates.

As part of this work PtSi diodes on  $\sim 30 \Omega\text{-cm}$  material with  $4 \mu\text{m}$  width and  $8 \mu\text{m}$  period. These exhibit  $\sim 100 \text{ msec}$  storage times in



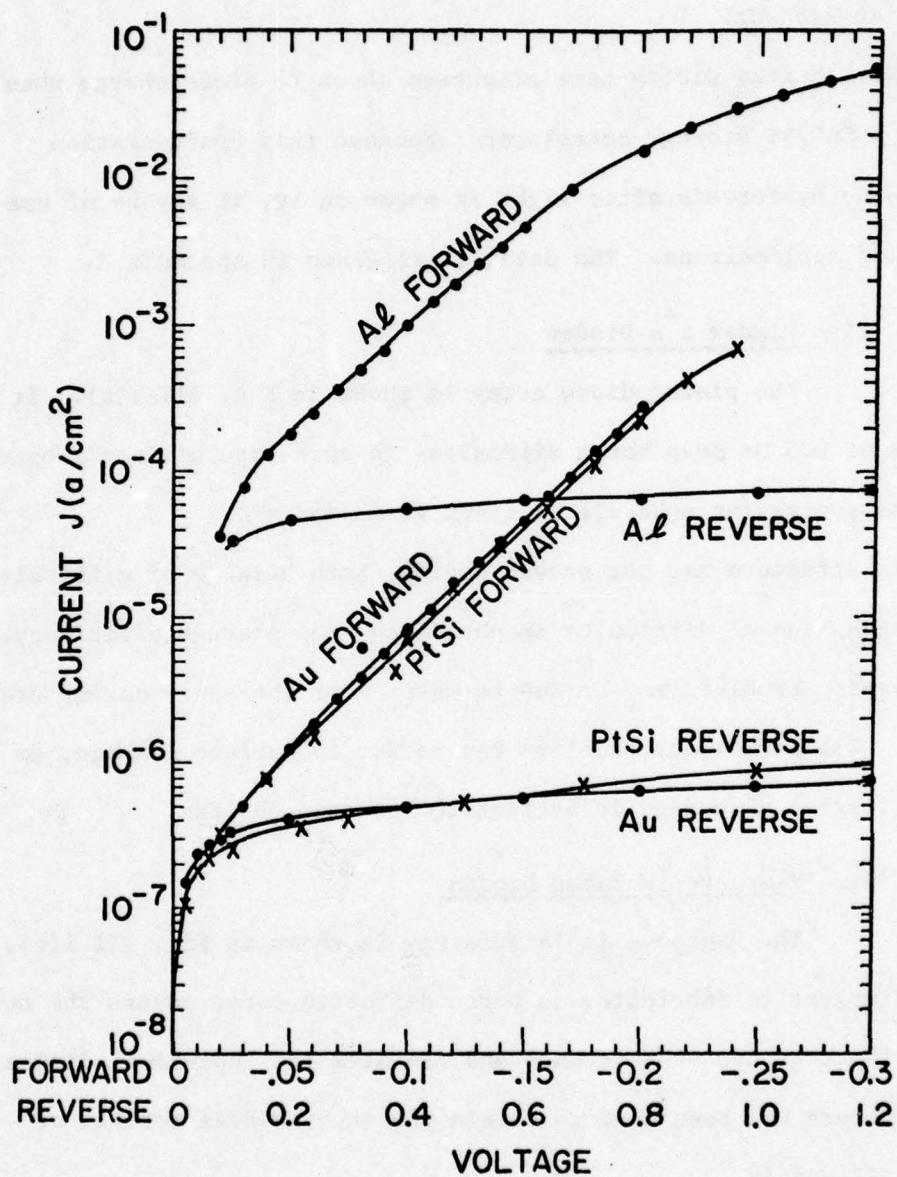


FIG. III-4. Experimentally Obtained Forward and Reverse Schottky Diode I-V Characteristics for Al, Au, and PtSi Diodes.

the pulsed acoustic-plate writing mode at a frequency of 100 MHz. A ~ 5 msec half-height storage time has been observed with similar diodes used in the acoustic-acoustic writing mode, with writing at 108 MHz and reading at 216 MHz.

PtSi Schottky diodes have also been shown to store charge when used in a ZnO/Si storage correlator. Because this configuration exhibits no hysteresis after light is shown on it, it may be of use in imaging applications. The details are given in Appendix E.

#### ii. Planar $p^+n$ Diodes

The planar diode array is shown in Fig. III-1(b). It consists of 0.5  $\mu\text{m}$  deep boron diffusions in an n-type silicon substrate. A typical processing schedule is given in Appendix D.

This structure has not proven useful, both because of difficulty in packaging and of difficulty in obtaining good storage efficiency. The packaging problems may be due to warping of the array during processing. The efficiency problems may be due to surface leakage, as will be further discussed in Section 2(c) of this chapter.

#### iii. V-Groove Isolated Diodes

The V-groove isolated array is shown in Fig. III-1(c). It is the simplest to fabricate. A boron diffusion first covers the entire wafer. The V-groove etch defines and isolates the individual diodes. This structure has been used to obtain the experimental results of Chapters II and IV.

The reverse leakage current will typically be higher than in a planar structure, due to surface generation on the sides of the depletion layers

exposed by the V-groove etching. Nevertheless, the half-height storage time is typically better than 5 msec, which is quite adequate for many signal processing applications. Passivation with  $\text{SiO}_2$  provides longer storage time and better long term stability of the array characteristics.

#### iv. Conductive Overlay Diodes

The conductive overlay structure is shown in Fig. III-1(d). A typical process schedule for doped polysilicon overlays is given in Appendix D. This structure has been observed to have storage correlator performance comparable to that of the V-groove arrays. The storage time is improved due to the added overlay capacity and lower thermal generation current in the depletion layer.

#### (c) Comparative Evaluation of the Array Structures

To summarize the salient result of the array comparison: The Schottky, V-groove isolated, and overlay structures exhibit good storage correlator performance. The planar structure often does not. Two possible reasons were conjectured. One was edge leakage. The other was interdiode charge transfer.

To test these hypotheses, the three diode array structures shown in Fig. III-5 were fabricated on a single wafer of 11 - 20  $\Omega$ -cm n-type silicon. The first structure, Fig. III-5(a), was composed of V-groove isolated mesa diodes. The second, Fig. III-5(b), was composed of planar diodes with V-grooves etched in between, to inhibit interdiode charge transfer. The third, Fig. III-5(c), was a planar structure. The period was 24  $\mu\text{m}$  ; all diodes were 6  $\mu\text{m}$  wide.



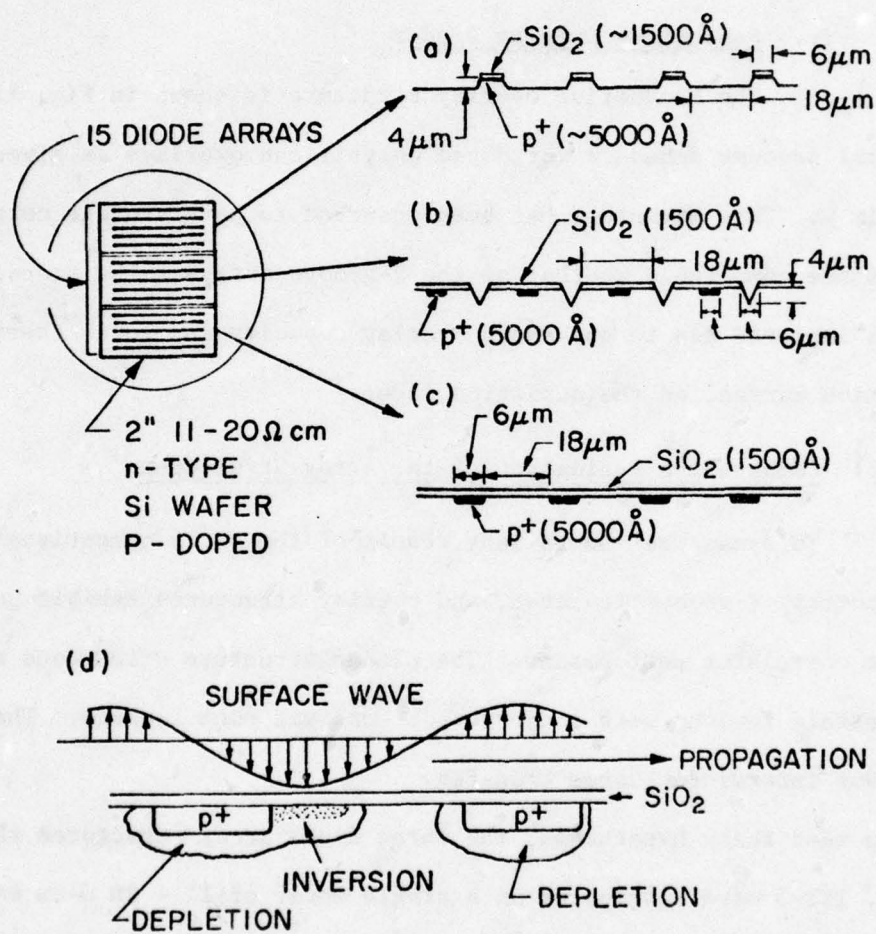


FIG. III-5 V-Groove and Planar  $\text{p}^+\text{n}$  Diode Comparison Experiment.

The V-groove structure, Fig. III-5(a), exhibited storage efficiency at 100 MHz in the rf acoustic-plate writing mode consistent with the low ratio of the diode width to period and low number of elements per wavelength. The other arrays exhibited no readout with the same charging signals. This indicates a problem with surface leakage at the junction edge, simply because the V-groove structure of Fig. III-5(a) is the only one of the three without a junction edge directly exposed to the acoustic and plate potentials. This result is consistent with the observed efficiency of the conductive overlay structure, since the overlay shields the surface near the junction edge.

It is thought that the poor performance of planar diodes is caused by surface inversion resulting from the presence of strong surface wave potentials. The inversion layer responds even at rf frequencies because the  $p^+$  region is a good source of holes.

The situation is shown in Fig. III-5(d). A negative traveling surface wave potential causes a transverse current of minority carriers to flow out of the  $p^+$  region, thereby transferring stored charge out of the diode. Others have investigated surface wave induced charge transfer of this sort and experimentally shown it to exist.<sup>67</sup> This phenomenon is, in fact, somewhat analagous to charge transfer in CCD's.

No such transverse current will flow in the V-groove structure because the material adjacent to the diode is physically removed. In the overlay structure, the junction is shielded, so that the junction boundary and nearby surface do not see the acoustic potentials. Since Schottky diodes are sources of majority carriers, the inversion layer is only supplied by thermal generation, which is too slow to respond

at rf frequencies. Thus, planar Schottky diode arrays exhibit good performance.

H. C. Tuan has recently fabricated planar diode arrays that exhibit good storage efficiency.<sup>17</sup> In his process, he added a phosphorus gettering layer to the back side of the wafer. It is possible that this and other process variations yield a different flatband voltage shift, resulting in a more accumulated surface. In this case, the surface wave potentials may never be strong enough to invert the surface and discharge the diodes.

(d) Summary

The V-groove isolated mesa structure has been employed in most of the experiments described here because of the following advantages over the other structures:

1. It is easiest to package uniformly. This is both because the grooves are good traps for microscopic dust particles, and because the serrated top surface releases flexing tension caused by high temperature processing, thermal oxide layers, and changes in the silicon due to the  $p^+$  diffusion.
2. It is most amenable to quantitative analysis. The vertical structure approximates a one-dimensional junction. Interactions due to interdiode material are minimized, and surface leakage effects are minimized.
3. It is extremely simple to fabricate. This yields good diode-to-diode uniformity.
4. It provides a good isolation between adjacent diodes, thereby allowing a high linear density of array elements.



### 3. Packaging

This section describes the various methods of reducing spurious signal feedthrough resulting from the high level reading signal. The suppression of rf feedthrough is considered first, followed by a discussion of acoustic feedthrough suppression techniques.

#### (a) RF Feedthrough Suppression

The suppression of rf feedthrough requires a systematic elimination of all radiation paths between the plate and acoustic ports. The required modifications of the Joly convolver structure are summarized in Fig. III-6. These changes have reduced the rf feedthrough to within 10 dB of the thermal noise floor, and about 10 dB below the acoustic feedthrough signals.

#### (b) Acoustic Feedthrough Suppression

Strong spurious acoustic signals, due to both surface and bulk waves, are generated during reading. These arise because most of the reading signal potential drops across the thickness of the piezoelectric delay line. Here, we catalog the various suppression techniques that have been examined, and describe the device as it was finally assembled.

##### 1. Phase Coded Transducers

Figure III-7 shows a 3 finger pair phase coded transducer. Because of the  $180^\circ$  phase shift introduced into each finger, such a transducer is insensitive to plane surface waves propagating to the fingers. This is discussed further in Appendix F.

One such transducer is used at each end of the delay line, and the diode array is broken into two sections, as shown at the bottom of Fig. III-7. The storage correlator then has two essentially identical parallel channels. The outputs from each sum in phase. In contrast,

# JOLY STRUCTURE MODIFICATIONS TO SUPPRESS RF FEEDTHROUGH

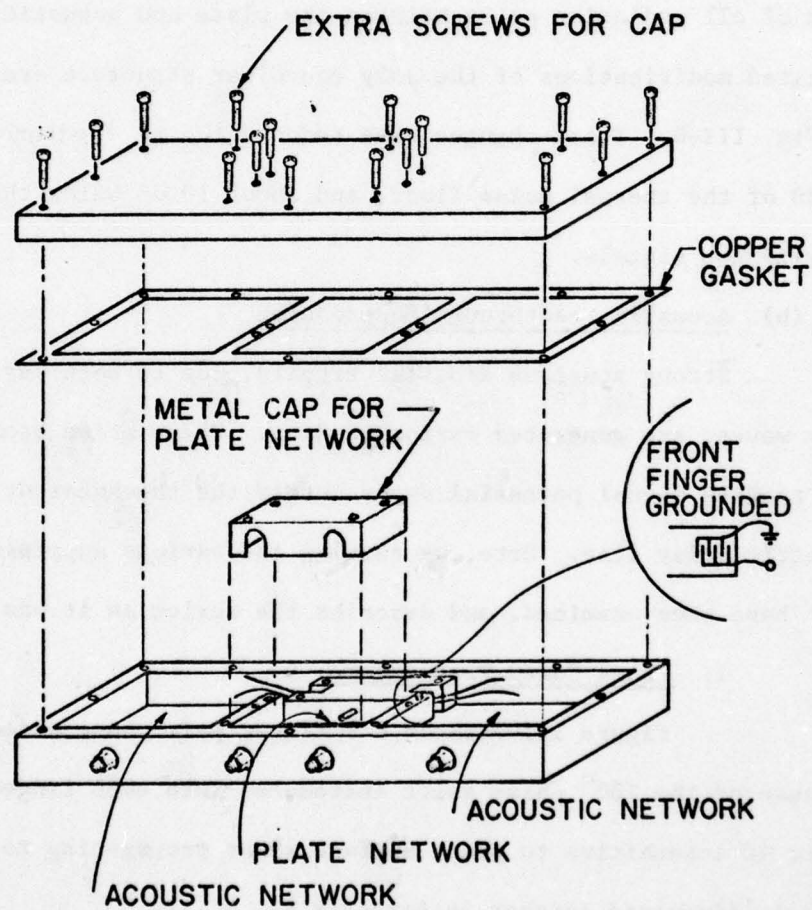


FIG. III-6 Modifications of the Joly Structure to Suppress rf Feedthrough.

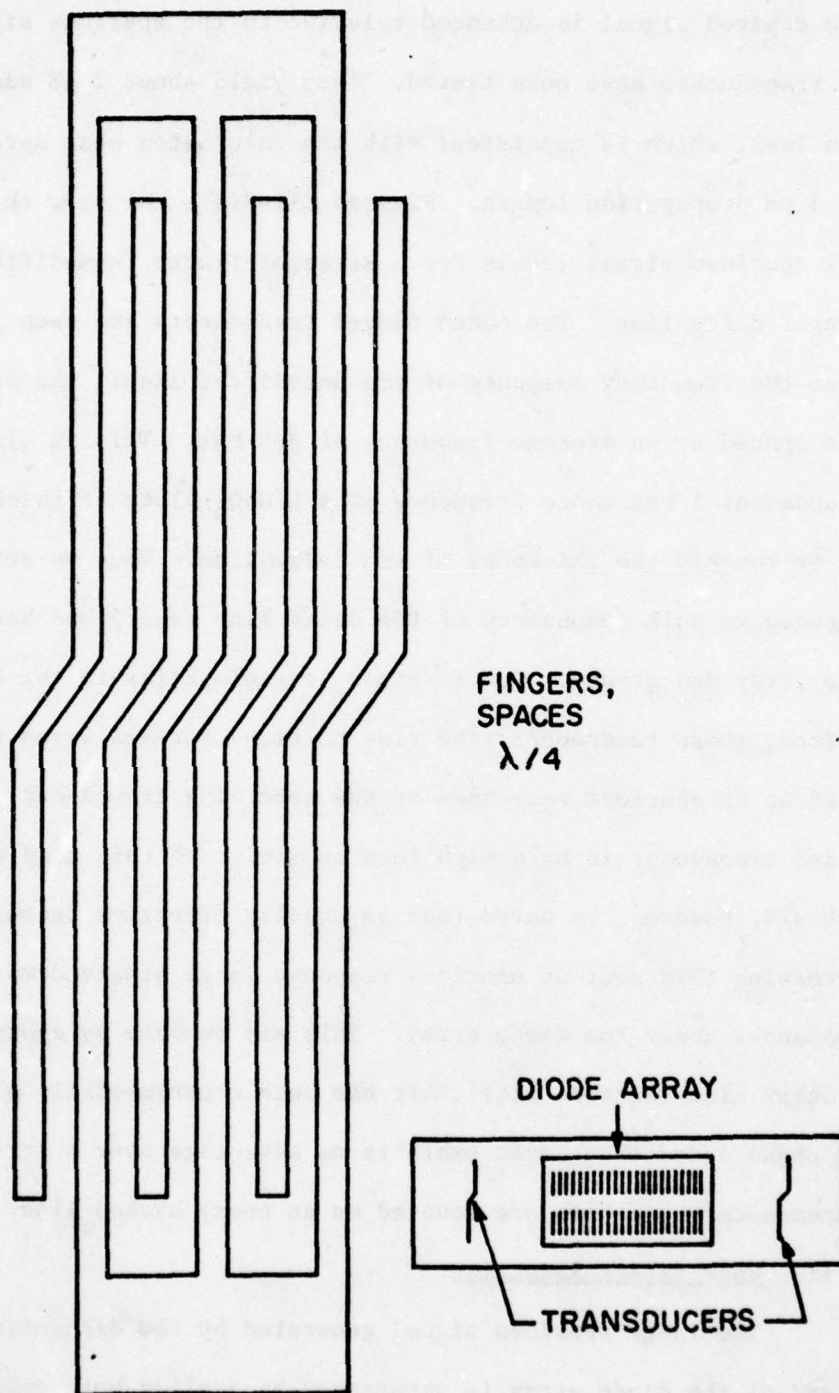


FIG. III-7 The Phase Coded Transducer and its Use in the Storage Correlator.



components of the output signal due to plane spurious surface acoustic waves tend to cancel over the length of the coded transducer fingers. Thus, the desired signal is enhanced relative to the spurious signals.

Such transducers have been tested. They yield about 2 dB additional insertion loss, which is consistent with the calculated beam spreading over the 3 cm propagation length. Figures III-8(a), (b) show the relative peak spurious signal levels for a straight finger (unmodified) and coded finger delay line. The coded finger transducers are seen to smooth out the frequency response of the unmodified line. The regular peaks are spaced by an average frequency of 3.5 MHz. This is close to the fundamental resonance frequency of a  $\text{LiNbO}_3$  plate of thickness 20 mils, or roughly the thickness of the delay line. Thus we attribute this response to bulk resonances of the delay line sandwiched between the diode array and ground. Due to minor irregularities in the delay line surface, these resonances give rise to plane surface waves that are picked up as spurious responses at the receiving transducer. The phase coded transducer is by design less sensitive to this kind of signal.

It should, however, be noted that an equally effective technique for suppressing this sort of spurious response is to simply damp the bulk resonances under the diode array. This may be done by epoxy backing the delay line (Section 3(c)). It has been experimentally observed that the phase coded transducer exhibits no advantage over a straight finger transducer when both are mounted on an epoxy backed line.

#### 11. Edge Effect Reduction

The large spurious signal generated by the discontinuity at each end of the diode array is suppressed by angling both ends about

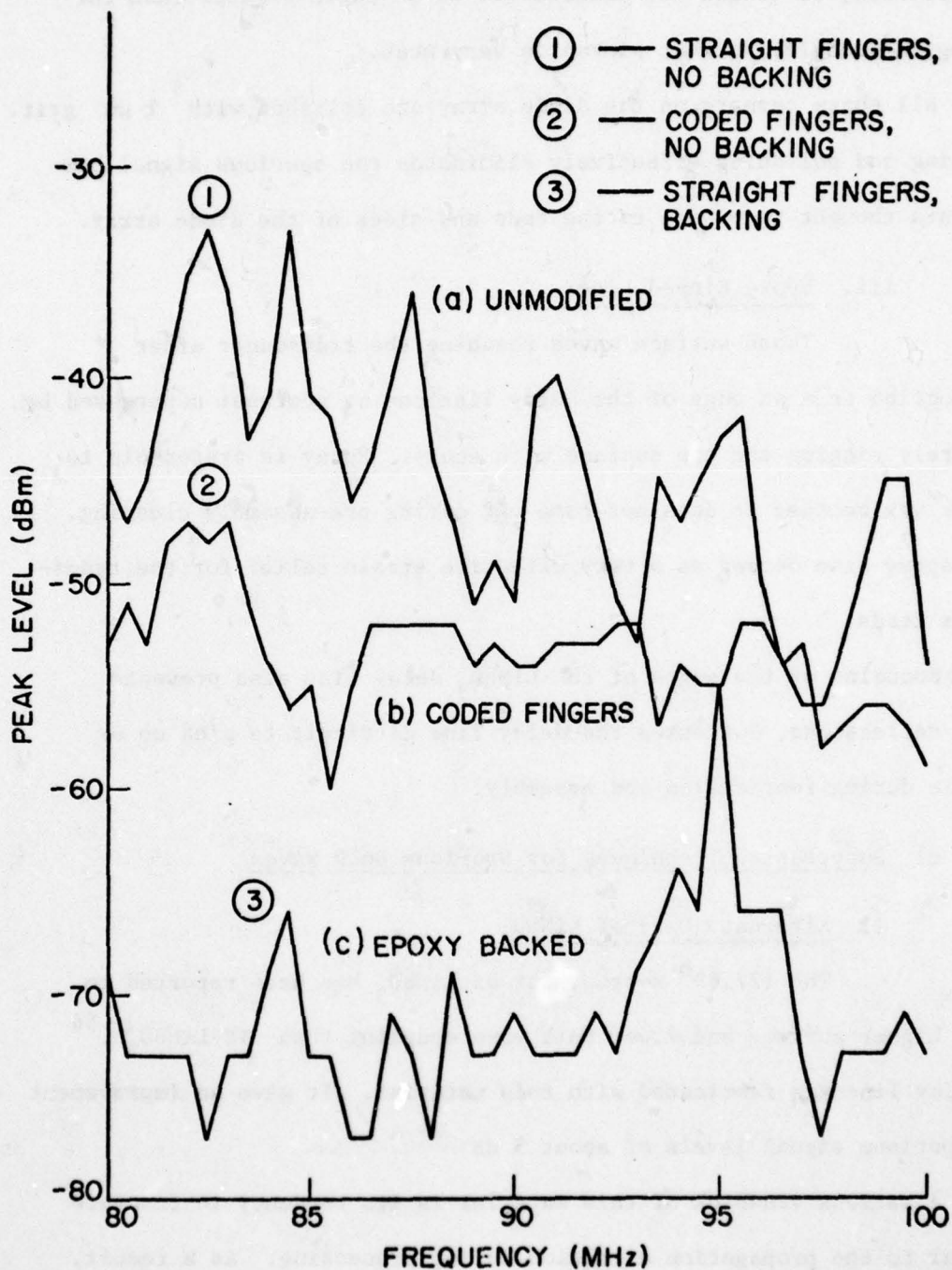


FIG. III-8 The Peak Spurious Signal Response vs. Frequency for Unmodified, Coded Transducer and Epoxy Devices.

45°. This directs all spurious signals from the ends away from the transducers, or toward the transducers at an angle greater than the acceptance angle, so that pickup is very weak.

All sharp corners on the diode array are polished with 1  $\mu$ m grit. Angling and polishing effectively eliminates the spurious signal components thought to be due to the ends and sides of the diode array.

iii. Epoxy Ringed Line

Those surface waves reaching the transducer after reflection from an edge of the delay line can be somewhat suppressed by entirely ringing the top surface with epoxy. Epoxy is preferable to black wax because it does not come off during pre-assembly cleaning. The epoxy also serves as a very effective strain relief for the transducer leads.

Rounding of the edges of the  $\text{LiNbO}_3$  delay line also prevents edge reflections, but makes the delay line difficult to pick up or handle during fabrication and assembly.

c) Suppression Techniques for Spurious Bulk Waves

i. Alternate Cuts of  $\text{LiNbO}_3$

The 127.89° x-prop. cut of  $\text{LiNbO}_3$  has been reported to have higher surface and lower bulk wave coupling than YZ- $\text{LiNbO}_3$ .<sup>54</sup> A delay line was fabricated with this material. It gave an improvement in spurious signal levels of about 5 dB.

A serious drawback of this material is its tendency to fracture normal to the propagation direction during processing. As a result, the yield of good delay lines is extremely low.



Another material of interest that has not been tried, but may be useful, is the  $45^\circ$  x-prop. cut of  $\text{LiNbO}_3$ .<sup>55</sup> Minimum diffraction cut (MDC)  $\text{LiTaO}_3$ <sup>56</sup> is also promising, but is not at present available in lengths as long as 3.5 cm.

#### ii. Top Grounds

Reducing the required reading signal amplitude will proportionately reduce the spurious signal generation while leaving the output level constant. This is possible with the top ground configuration shown in Fig. III-9(a). The ground plane is brought to the top of the delay line by sputtering a metal film around the edge. The diodes are long bars that overlap both the acoustic beam and the top ground strips.

The series capacity of the plate circuit,  $C_{\text{SiO}_2}$  is now due to the thin sputtered  $\text{SiO}_2$  insulator film, rather than the thick  $\text{LiNbO}_3$ , as shown in the equivalent circuit model, Fig. III-9(b). As a result, it is possible to reduce the plate signal  $V_p$  required to produce a given voltage drop across the diode by about an order of magnitude.

In practice, the resistance between the top ground strips and the metal on the back of the delay line is a few ohms. As a result, the top ground strips couple a strong rf feedthrough signal to the nearby transducers. This is usually of greater strength than the spurious acoustic signals observed with other configurations.

#### iii. Deep Slots

Bulk wave propagation from the region under the diode array to the transducers can be physically impeded by cutting slots in

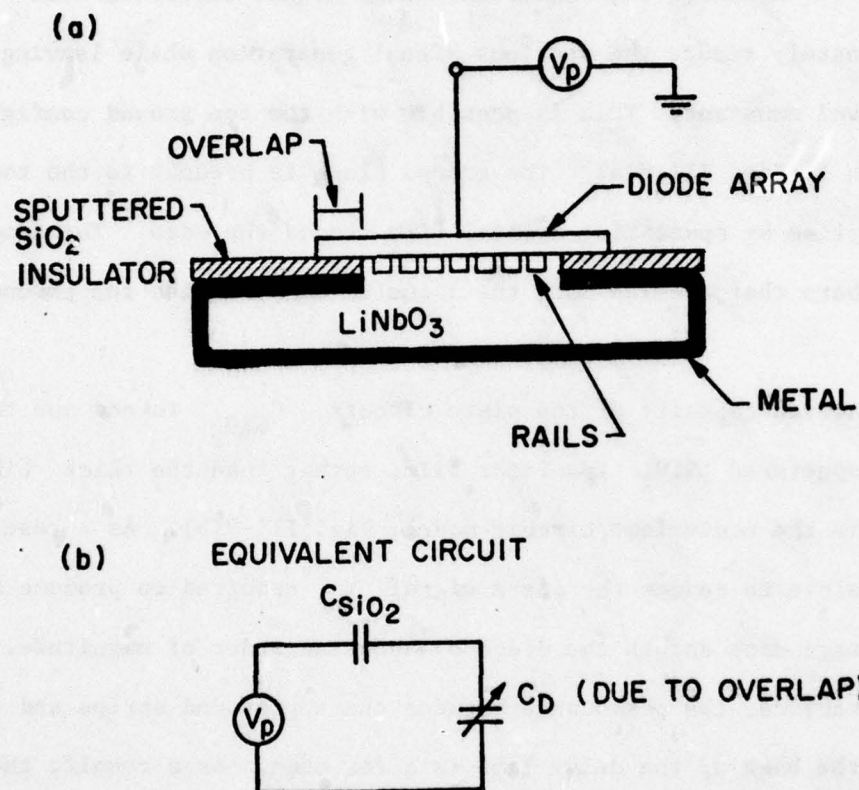


FIG. III-9 The Top Ground System and its Equivalent Circuit Model.

the back of the  $\text{LiNbO}_3$ . Such slots should not be closer than 3 to 4 wavelengths from the surface, lest they effect the surface wave propagation. In practice, it is extremely difficult to cut deep slots in the already thin  $\text{LiNbO}_3$  delay line without propagating defects to the surface. Furthermore, a large part of the spurious acoustic signal results from bulk-to-surface wave mode conversion in the region under the diode array. Slots will not hamper the propagation of such spurious components.

iv. Transducers with a Large Number of Finger Pairs

In applications where limited bandwidth is tolerable, transducers with a large number of finger pairs may be employed. These have higher coupling to surface waves and lower sensitivity to incident bulk waves. This is because a transducer with a large number  $N$  of finger pairs tends to have a narrow acceptance angle for incident bulk waves. It may be shown that for an interdigital transducer with narrow fingers center-to-center spaced  $\lambda/2$ , the magnitude of the response  $\phi$  to a plane wave of wavelength  $\lambda_B$  incident at an angle  $\theta$  ( $\theta = \pi/2$  for propagation parallel to the surface) varies as

$$|\phi| \sim \frac{\sin(N \pi \lambda / \lambda_B \sin \theta)}{\sin(\pi \lambda / \lambda_B \sin \theta)} \approx \frac{\sin(N \pi \lambda / \lambda_B \sin \theta)}{\pi \lambda / \lambda_B \sin \theta} .$$

It is seen that as the angle of incidence  $\theta$  moves away from the normal ( $\theta = 0$ ), for large numbers of finger pairs  $N$  the term in numerator fluctuates rapidly with small changes in angle of incidence  $\theta$ . For a 10 finger pair transducer with  $\lambda = \lambda_B$ , the first zero



in the response is at  $5.7^\circ$  from the surface. For 3 finger pairs, the first zero is at  $19.5^\circ$ . Thus, the acceptance angle for grazing angle waves is narrower for the  $N = 10$  transducer.

v. Continuous Grounds

The entire bottom of the delay line must be continuously and firmly grounded. Breaks in the bottom ground plane have been observed to cause spurious bulk wave generation. This results from higher field regions near such discontinuities.

vi. Backside Roughening and Conductive Epoxy Loading

The most effective spurious suppression technique has been a combination of roughening the back of the delay line and loading with a conductive epoxy layer  $\geq 5$  mils thick. Figure III-8(c) shows the spurious mode spectrum resulting from this technique.

The conductive epoxy layer functions as a lossy backing. As bulk waves reflect off the back side of the delay line, a portion of their energy leaks into the epoxy, where it is quickly dissipated. In addition, the rough bottom acts as a diffuse reflector for the energy that is not absorbed in the epoxy.

To be effective, the acoustic impedance of the epoxy should match that of the  $\text{LiNbO}_3$ . In practice, this is not possible because of the high impedance ( $35 \times 10^6 \text{ kg/s-m}^2$ ) of the  $\text{LiNbO}_3$ . Conductive epoxy probably has increased impedance due to the silver filling material. In practice, conductive epoxy must be used because it serves the dual function of lossy backing and high quality ground plane.

As was already noted, the spurious wave resonance structure is due to the excitation of high order plate modes. These can be described in terms of the superposition of bulk wave reflections from the upper and lower surfaces of the delay line. The delay line is very much longer than it is wide, so that most excited plate modes will be effectively damped with a low impedance backing before they reach the transducer.

It is of interest to note that the phase coded transducer exhibits no advantage over a straight finger transducer when both are mounted on an epoxy backed line. This is because the backing eliminates those bulk waves that undergo numerous internal reflections and give rise to the spurious surface wave signals to which the phase coded transducer is least sensitive.

(d) Actual Configuration

The assembly that achieved the best performance is shown in Fig. III-10. The diode array ends were angled and the edges polished smooth. The delay line was epoxy ringed and roughened on the bottom with 15  $\mu\text{m}$  grit. 10 finger pair, 108 MHz straight finger transducers were employed. The gold coated sapphire ground of the original Joly design was removed and the delay line rested against the cap of the carrier box. This provided a continuous ground plane.

The center region of the back of the delay line was only roughened after assembly. This allowed visual inspection of the interaction region during assembly, so that maximum uniformity could be attained. Afterwards, the remainder of the back of the  $\text{LiNbO}_3$  was roughened through a window in the carrier box cap. The window was then back-filled with silver epoxy.

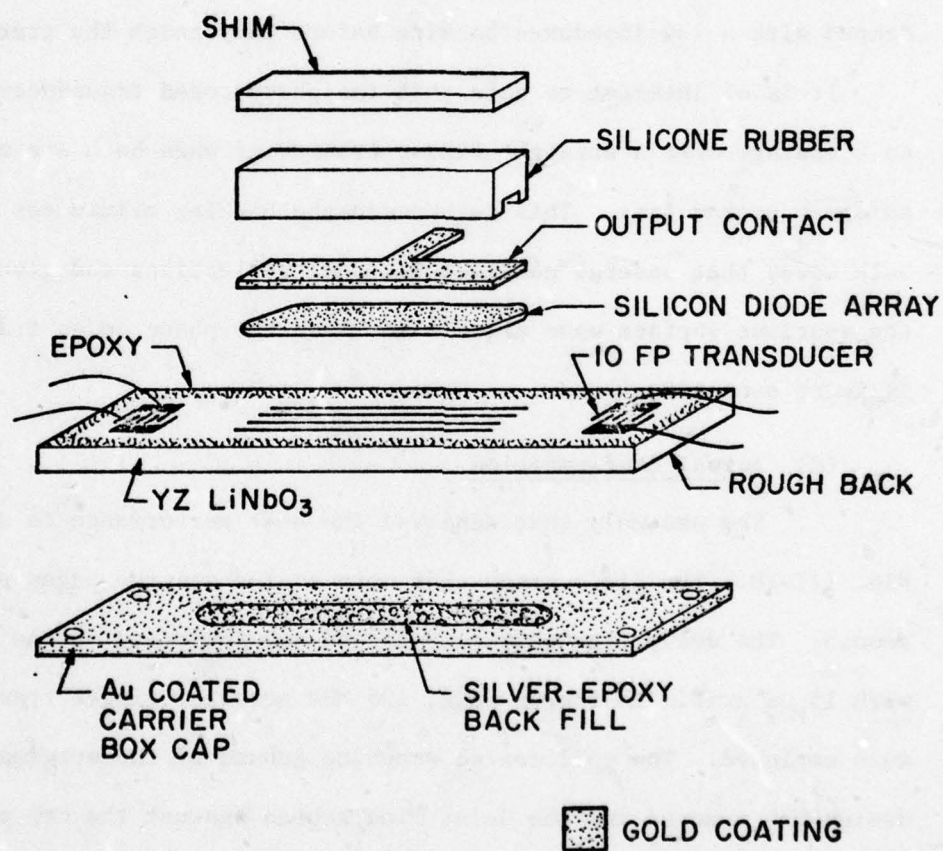


FIG. III-10 Device Assembly for Reduced Spurious Acoustic Responses.



This configuration yielded a peak spurious signal level 36 dB below the readout at 108 MHz. This is still about 20 dB above the thermal noise floor. Uniformity of the output signal was  $\pm 0.5$  dB over the full interaction length.

(e) Comments on the Spacer Rails

Joly has described a process for masking the spacer rails with positive photoresist (AZ1350J) prior to sputter etching.<sup>27</sup> It has been found that negative photoresist (Kodak 747) works equally well, and offers the following advantages:

1. The process requires a dark, rather than clear, field mask, providing insensitivity to dust and defects on the mask.
2. While overexposure of the positive resist pattern leads to washout, overexposure of the negative resist pattern causes the rails to become 1 to 2  $\mu\text{m}$  wider.

It has been found that these two features of a negative resist process both increases yield and shortens the processing time.

Extending the sputter etch time to 25 minutes while leaving all other parameters identical to Joly's results in 3000  $\text{\AA}$  rails. Deeper rails appear to provide a more uniform interaction region. In the best device, uniformity was  $\pm 0.5$  dB over the full interaction region.

4. Electrical Design

A broadband plate matching circuit has been designed. Figure III-11 shows the calculated real and imaginary part of the input impedance and the transfer function, all of which have been experimentally verified. Here, the storage correlator itself is modeled as a series

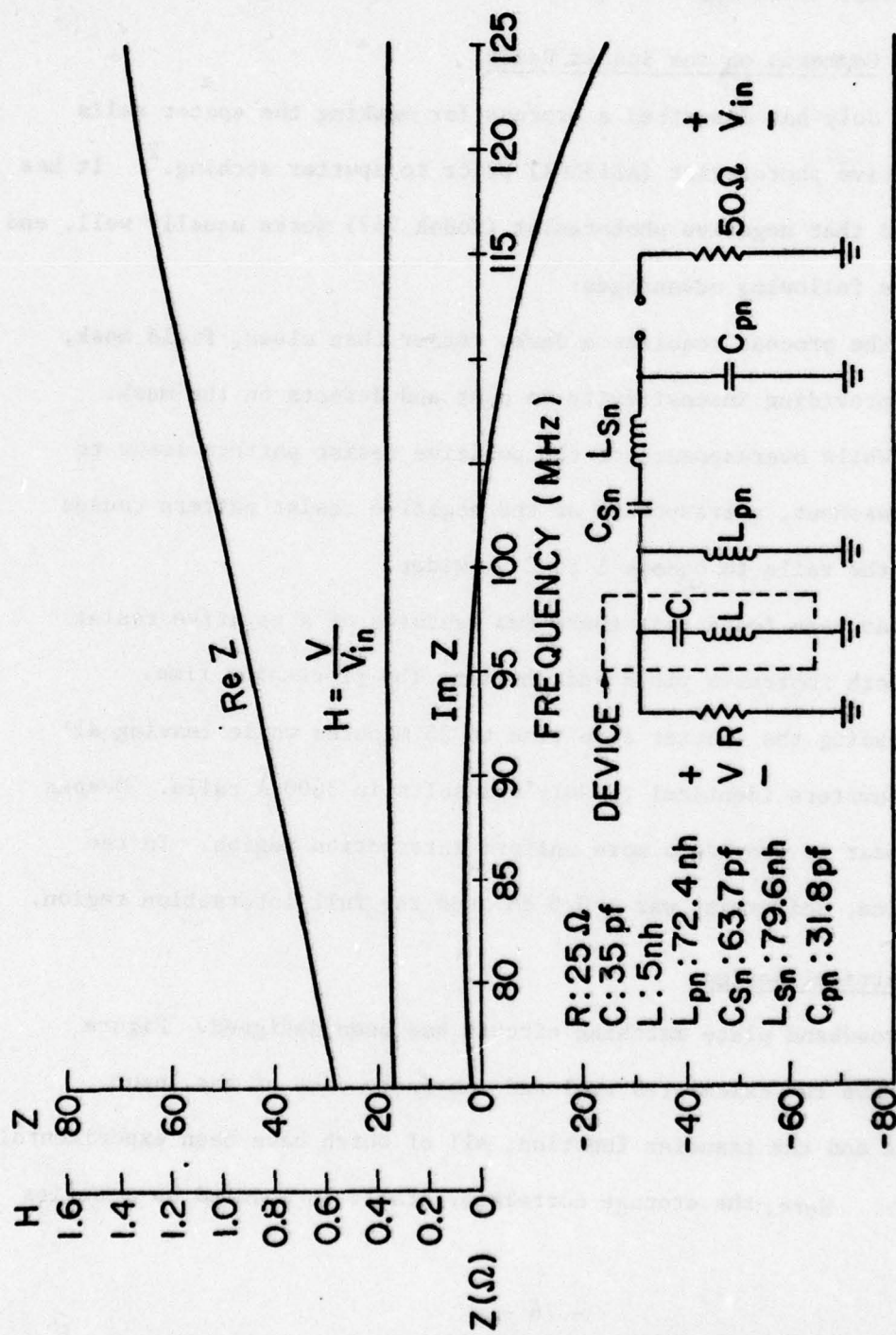


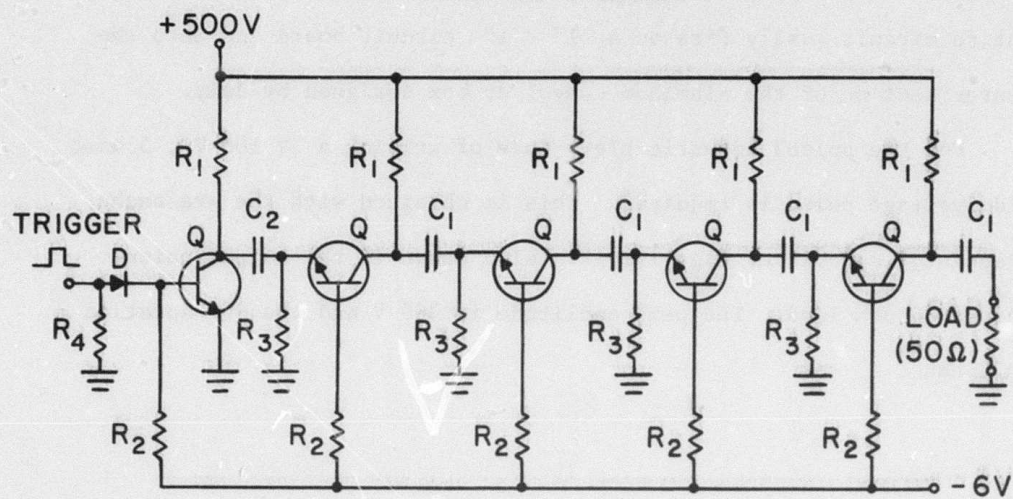
FIG. III-11 The Plate Matching Network and its Calculated Input Impedance and Transfer Characteristics.

LC circuit, with measured values of  $L = 5 \text{ nh}$  and  $C = 35 \text{ pf}$ . The entire circuit easily fits on a  $1" \times 1"$  circuit board and into the center section of the aluminum convolver box designed by Joly.

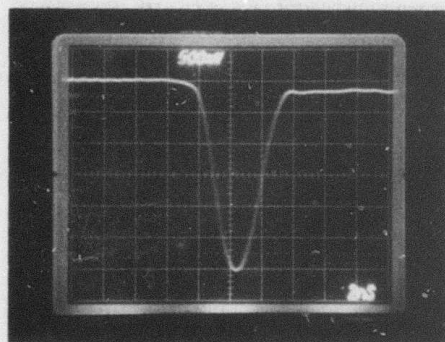
For the pulsed acoustic-plate mode of writing a  $\geq 100 \text{ V}$ ,  $5 \text{ nsec}$  wide voltage pulse is required. This is obtained with the avalanche transistor circuit of Fig. III-12. Also shown in the output pulse into a  $50 \text{ ohm}$  load. The peak amplitude is  $305 \text{ V}$  and the 90% duration is  $5 \text{ nsec}$ .



# HIGH VOLTAGE PULSER



$R_1$  : 470 k $\Omega$      $R_3$  : 5 k $\Omega$      $C_1$  : 200 pF    Q : 2N3019  
 $R$  : 10 k $\Omega$      $R$  : 2 k $\Omega$     C : 20 pF    D : 1N914



OUTPUT PULSE  
 INTO 50 $\Omega$  LOAD  
 (100V/div)

FIG. III-12 The High Voltage Pulser Circuit and  
 a Typical Output Pulse.

## CHAPTER IV

### SIGNAL PROCESSING APPLICATIONS

#### 1. Introduction

The storage correlator performs, in real time, either the convolution or correlation of the stored charge pattern and the reading signal. For all practical purposes, it is simply a filter whose impulse response is the stored charge pattern or its time inverse. Since this charge pattern is written into the device with externally applied signals, the storage correlator is a programmable filter.

This is precisely why the storage correlator is such a versatile signal processing device. Many signal processing functions are extremely difficult to perform economically with fixed filters, either because of complexity, or because the changing nature of the signal to be processed makes a fixed filter of little value.<sup>52</sup> As a programmable filter, the storage correlator is uniquely suited for many of these applications.

This chapter presents a comprehensive description of the storage correlator as a signal processor. To begin, the basic convolution and correlation processes are described, and the meaning of the term "dynamic range" is discussed.

Several special cases and applications are then considered. These include correlation with  $\delta$  functions, which allows direct or time inverted readout of the charge pattern, or use of the device as an electronically variable analog delay line. Next, the correlation of coded sequences, and, in particular, Barker codes, is discussed. Finally, various chirp correlation techniques are considered, with device applications as an optimum matched filter and as a transform processor.



Specifically, as an optimum matched filter, the device is used to improve the resolution of a pulse-echo system by filtering out phase distortions. As a transform processor, the device is used as an electronically variable pulse expander.

Correlation of input signals, a technique that greatly enhances the device's signal processing performance in certain applications, is discussed next.

Finally, various factors influencing the performance as a signal processor are considered. The connection between writing time and storage time is discussed, and an experiment is described which proves that it is possible to rapidly write signals into long storage time diodes. Various factors that degrade performance are also discussed, such as phase mismatches between the writing and reading signals, propagation loss, nonuniformities in the interaction region, and spurious signal generation.

## 2. General Description

### (a) Signal Processing Functions: Convolution and Correlation

In later sections, it will be convenient to consider the storage correlator as a programmable filter. In this section we justify this approach by demonstrating that the device either correlates or convolves the reading signal modulation with a reference signal stored during the writing process. In Chapter II, it was shown that there are two methods of writing (pulse and slow) and two methods of reading (plate-to-acoustic and acoustic-to-plate). Depending on the choice of transducers and methods for reading and writing, eight ways of operating



the device exist. These are summarized in Table IV-1. In the remainder of this section, a representative sample of the cases in this table will be described in detail.

We first consider the case of line 1 of Table IV-1, with pulse writing and acoustic-to-plate reading. One transducer is used to input the writing signal; the opposite transducer is used to input the reading signal. If the modulation of the signal stored during writing is  $F(t)$ , the component of stored charge contributing to readout has the form

$$Q = KF \left( \frac{z_n}{v_a} \right) \left( e^{j\beta z_n} + e^{-j\beta z_n} \right) \quad (\text{IV-1})$$

where  $K$  is a constant, and  $\beta$  and  $v_a$  are the surface wave propagation constant and velocity under the diode array.  $z_n$  is the position of the  $n^{\text{th}}$  diode array element.

The reading signal is an acoustic surface wave with an associated potential  $G(t - z/v_a) \left( e^{j(\omega t - \beta z)} + \text{c.c.} \right)$ . From Eqs. (II-37) and (II-39) the readout, appearing at the plate as an rf signal, has the form

$$V_0 \sim \sum_n \left[ KF \left( \frac{z_n}{v_a} \right) \left( e^{j\beta z_n} + \text{c.c.} \right) \times G \left( t - \frac{z_n}{v_a} \right) \left( e^{j(\beta z_n - \omega t)} + \text{c.c.} \right) \right] \quad (\text{IV-2})$$

TABLE IV-1

## STORAGE CORRELATOR OUTPUT FUNCTIONS

	<u>WRITE MODE</u>	<u>READ MODE</u>	<u>TRANSDUCERS</u>	<u>OUTPUT MODULATION</u>
1.	Pulse	AP	0	$\int F(\tau) G(t - \tau) d\tau$ (convolution)
2.	Slow	AP	S	
3.	Pulse	AP	S	$\int F(\tau - t) G(\tau) d\tau$ (correlation)
4.	Slow	AP	0	
5.	Pulse	PA	0	$\int F(\tau) G(t - \tau) d\tau$ (convolution)
6.	Slow	PA	S	
7.	Pulse	PA	S	$\int F(\tau - t) G(\tau) d\tau$ (correlation)
8.	Slow	PA	0	

Key: Pulse - Pulsed writing mode

Slow - Slow writing, acoustic pulse scans diode array as rf signal is applied to the plate

AP - Acoustic-to-plate reading

PA - Plate-to-acoustic reading

S - Same transducer employed for reading and writing

0 - Opposite transducers employed for reading and writing

F(t) - Modulation of the stored charge pattern

G(t) - Modulation of the reading signal

For a high density diode array, the sum becomes an integral over the integration region. The stored charge is zero outside of the interaction region, so the integration limits may be extended to  $\pm \infty$ . Then, taking the wave number  $\beta = 0$  with frequency  $\omega$  component of the output voltage, the output is of the form

$$V_0 \sim K \left( e^{j\omega t} + \text{c.c.} \right) \int_{-\infty}^{\infty} F\left(\frac{z}{v_a}\right) G\left(t - \frac{z}{v_a}\right) d\left(\frac{z}{v_a}\right) . \quad (\text{IV-3})$$

By substituting  $\tau = z/v_a$ , Eq. (IV-3) can be rewritten as

$$V_0 \sim K \left( e^{j\omega t} + \text{c.c.} \right) \int_{-\infty}^{\infty} F(\tau) G(t - \tau) d\tau . \quad (\text{IV-4})$$

The modulation of the output signal is seen to be the convolution of the stored reference signal  $F(t)$  and the reading signal  $G(t)$ .

Consider now the case of line 2 of Table IV-1, with acoustic-to-plate reading and the same transducer used to introduce the reading and writing signals. In this case, writing is accomplished by applying the input signal,  $F(t)e^{j\omega t}$ , to the plate while scanning with a short acoustic pulse with greater bandwidth than the input signal modulation,  $F(t)$ . A charge pattern corresponding to  $F(t = 0)$  is stored near the end of the diode array closest to the transducer used to input the acoustic scanning pulse. In the previous case, which differed only to the extent that pulse writing was used, a charge pattern corresponding to  $F(t = 0)$  was stored near the end of the diode array furthest from the transducer. used during writing. Thus, to obtain identical outputs for the two



cases, if the same transducer is used to input the writing signals in the two cases, opposite transducers must be employed to input the reading signal.

The analysis of the cases of lines 3 and 4 of Table IV-1 follows in an identical manner, with the results given in Table IV-1.

Finally, we consider the case of line 5 of Table IV-1. This is identical to the already analyzed case of line 1, except plate-to-acoustic reading is employed. The reading signal  $G(t) (e^{j\omega t} + \text{c.c.})$  is applied to the plate and the output appears as a propagating acoustic surface wave. From Eq. (II-48), the excited surface wave potential  $\phi_a(z, t)$  is of the form

$$\phi_a(z, t) = j\gamma e^{-j\gamma z} \int \phi\left(z', t - \frac{z' + z}{v_a}\right) e^{j\gamma z'} dz' \quad (\text{II-48})$$

where  $\gamma$  is the perturbation of the propagation constant due to the presence of the diode array. From Eq. (II-41), the total potential at the diode surface,  $\phi(z, t)$ , is proportional to the product of the stored charge pattern,  $F(z) (e^{j\beta z} + \text{c.c.})$ , and the reading signal amplitude,  $G(t) (e^{j\omega t} + \text{c.c.})$ . Upon substitution into Eq. (II-48), the excited forward traveling wave amplitude is found to be

$$\begin{aligned} \phi_a(z, t) &= K e^{-j(\omega t - \beta z)} \int_{-\infty}^{\infty} F\left(\frac{z'}{v_a}\right) G\left(t' - \frac{z'}{v_a}\right) d\left(\frac{z'}{v_a}\right) \\ &= K e^{-j(\omega t - \beta z)} \int_{-\infty}^{\infty} F(\tau) G(t' - \tau) d\tau \end{aligned} \quad (\text{IV-5})$$

with  $t' = t - z/v_a$  .  $K$  is a constant absorbing all factors independent of the position of the output transducer,  $z$  . The modulation of the output is the convolution of the modulations of the stored reference signal,  $F(t)$ , and the reading signal,  $G(t)$ .

In obtaining Eq. (IV-5), it has been assumed that the writing and readout surface waves experience the same propagation constant perturbation,  $\gamma$  . This is not strictly true, since  $\gamma$  is a weak function of the amount of stored charge. Consequently, the use of strong writing signals may severely degrade correlation performance. A detailed discussion of this problem is provided in Appendix C.

During plate-to-acoustic reading, both forward and backward traveling waves are excited. The amplitude of the backward wave is given by Eq. (IV-5) with the substitution  $F(z/v_a) \rightarrow F(-z/v_a)$  , which corresponds to a spatial inversion of the stored charge pattern. The acoustic potential seen at the output transducer is now of the form

$$\phi_a(z,t) = K e^{j(\omega t + \beta z)} \int_{-\infty}^{\infty} F(\tau - t') G(\tau) d\tau . \quad (IV-6)$$

This is the correlation of the modulations of the stored reference signal,  $F(t)$  , and the rf reading signal,  $G(t)$  . Equation (IV-6) corresponds to the case shown in line 7 of Table IV-1. Similar analyses apply to the cases shown in lines 6 and 8 of Table IV-1.

(b) Dynamic Range

The dynamic range is the useful linear range over which a signal may vary. The upper limit is usually due to saturation and high field effects causing a deviation from linearity. The lower limit is defined by either the thermal noise or the spurious signal level.

Two separate definitions of dynamic range are applied to the storage correlator. The first, called the input dynamic range, is the full range over which the output amplitude varies linearly with the amplitude of the writing signal whose modulation has been stored. The upper limit of this range is usually fixed by saturation and high field effects. The lower limit for present devices is reached when the output amplitude equals the amplitude of the spurious signals due to coupling from the readout signal.

The second definition of dynamic range, called the output dynamic range, is the full range over which the output varies linearly with the amplitude of the reading signal. The upper limit here is reached when diode conduction current begins to flow, thereby causing the readout to become nonlinear. Since the spurious signal amplitude decreases with the reading signal amplitude, the output dynamic range is limited at the low end by thermal noise.

Because spurious signals do not limit the output dynamic range, it is typically greater than the input dynamic range. For the device used to obtain the data in Figs. (II-6) and (II-7), the input dynamic range was about 35 dB at 108 MHz. The output dynamic range was about 55 dB, the 20 dB difference corresponding to the strength of the spurious signals introduced by coupling from the readout signal.



### 3. Special Cases and Experimental Results

#### (a) Delta Function Readout

##### i. Reproduction and Time Reversal of a Stored Signal

Applying a delta function reading signal,  $\delta(t)$ , excites an output whose modulation is a replica or time-reversed replica of the modulation of the stored charge pattern. In practice, a delta function reading signal may be a single pulse of duration less than one-half rf cycle, or an rf pulse with greater bandwidth than the stored signal. From Table IV-1, substituting a reading signal modulation of the form  $G(t) = \delta(t)$  gives the convolution outputs (lines 1, 3, 5 and 6)

$$\int F(\tau) \delta(t - \tau) d\tau = F(t) .$$

This corresponds to a direct readout of the stored charge pattern modulation,  $F(t)$  .

The correlation outputs (lines 3, 4, 7 and 8) yield

$$\int F(\tau - t) \delta(\tau) d\tau = F(-t) .$$

This corresponds to a time-reversal of the stored charge pattern modulation,  $F(t)$  .

##### ii. A Programmable Tapped Delay Line

Consider now the case of storing a short pulse approximating a delta function. We shall see that the device response is always a delayed replica of the reading signal. The delay is equal to the

propagation time between the transducer used for reading and the location of the stored delta function. The stored  $\delta(z)$  thereby functions as an output tap, and the storage correlator becomes a programmable tapped delay line.

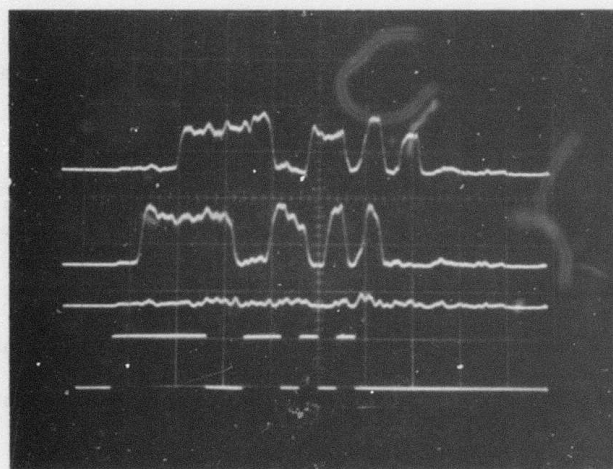
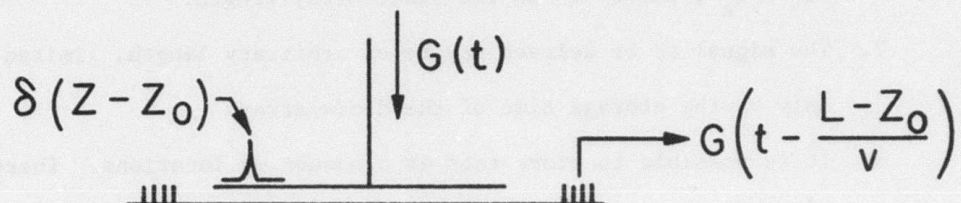
The physical situation is seen in Fig. IV-1. A short charge pattern, approximating a  $\delta(z)$ , is stored at a position  $z_0$ . In practice, this is accomplished by applying a short plate pulse when a short acoustic writing pulse has propagated to the position  $z_0$ . The principal constraint, which becomes the physical definition of a  $\delta(z)$  charge pattern, is that the bandwidth  $\Delta z/v_a$  of the charge pattern stored over the region of width  $\Delta z$  must be greater than the bandwidth of the reading signal modulation.

When the reading signal  $G(t)e^{j\omega t}$  is applied to the plate, an output surface wave will be excited only at the position of the stored charge pulse,  $z_0$ . This surface wave propagates a distance  $L - z_0$  before being received at the transducer located at the position  $z = L$ . Thus, the delay time is  $(L - z_0)/v_a$ , where  $v_a$  is the acoustic propagation velocity.

This result may be obtained directly by substituting a charge pattern modulation  $F(t) = \delta[(z - z_0)/v_a]$  into any of the output modulation forms shown in Table IV-1. In all cases, the output is simply a replica of the reading signal  $G(t)$  delayed by the propagation time between the position of the stored delta function,  $z_0$ , and the position of the transducer used for reading.

This technique offers the following unique features:

# ELECTRONICALLY VARIABLE DELAY WITH THE STORAGE CORRELATOR



4  $\mu$ sec DELAY

NO DELAY

NO INPUT

INPUT SIGNAL

$\rightarrow$  |  $\leftarrow$  5  $\mu$ sec

FIGURE IV-1



1. The storage correlator becomes an electronically programmable tapped delay line, with the delay time variable over a range of  $L/v_a$ , where  $L$  is the diode array length.
2. The signal to be delayed may be of arbitrary length, limited only by the storage time of the diode array.
3. It is possible to store taps at a number of locations. These taps may be weighted in both amplitude and sign by appropriate choice of the amplitude and phase of the writing signals. With multiple taps, the output signal will be the superposition of the outputs from the individual taps. This mode of operation is particularly suited to adaptive filtering applications, where a microprocessor is used to iterate tap weights and signs until the storage correlator simulates a desired filter function.<sup>47</sup>

It is important to note some of the drawbacks of using the storage correlator as an electronically variable tapped delay line. Foremost is the low signal-to-noise ratio. This is principally because there is no correlation gain, and only a small region of the diode array is used to excite the output. When long signals are delayed, additional problems may arise due to triple transit echoes. In many applications, the relatively short delay of a few microseconds might well present a serious limitation. This would be costly to overcome, since very long devices are difficult to fabricate.

Finally, we make note of the number of tap locations available, or, alternately, the number of taps that may be stored. This is limited

by the width of a tap and the length of the diode array and corresponds to the time bandwidth product of the device. In practice, the width of the stored delta function is approximately the inverse of its bandwidth, which is in turn usually constrained by the input transducer bandwidth. For a bandwidth of 30 MHz, an acoustic velocity of  $v_a = 3.5 \times 10^5$  cm/sec, and a diode array length of  $L = 2$  cm, the time bandwidth product is 171, so 171 taps can be stored.

An experimental demonstration of operation with a single tap is shown in Fig. IV-1. The diode array length of 2 cm allowed a maximum delay of 5.7  $\mu$ sec. The delta function was stored in the acoustic-plate writing mode with a 5 nsec plate pulse. The acoustic pulse had a 3 dB width of about 500 nsec. The delayed signal was the 25  $\mu$ sec, 13 bit code shown in the bottom trace. Note that  $v_a t = 8.7$  cm for this signal, or over four times the diode array length. The top trace shows a 4  $\mu$ sec delay; the second trace shows no delay. The third shows the output when no tap is stored.

As is clearly seen in Fig. IV-1, the most serious performance limitation is due to the generation of spurious signals during reading. The output amplitude increases linearly with the interaction length, which is here the width of the stored delta function and, hence, very short. Spurious signals are generated from the full diode array length, so the input dynamic range (cf. Section 2(b)) is low, about 10 dB in the present example. Complete elimination of spurious responses would increase this dynamic range to a more usable level of about 40 dB.

(b) Coded Sequences, Pulse Compression

The storage correlator may be used to correlate coded signals in order to obtain pulse compression. In particular, we consider the autocorrelation of two long phase coded sequences, resulting in an output waveform with a narrow, high peak and, ideally, low sidelobes.

Such techniques are of considerable interest in radar and sonar design. For reasons of limited transmitter power, the need to accurately determine target velocity, and the need to differentiate against interfering signals, it is desirable to employ long signals. Such signals yield poor time resolution unless they can be compressed in the receiver, which is precisely what phase coding and correlation makes possible.<sup>45</sup>

The correlation of long phase coded sequences provides the added advantage of improved signal-to-noise ratio (S/N). This is simply because white noise has a random phase, which tends to cancel over the long correlation time during which the coherent phase coded sequences add in phase. It can be shown that the improvement in signal to noise obtainable by such a process is approximately  $TB$  where  $T$  is the correlation time and  $B$  the bandwidth of the signals.

We consider two specific examples: Barker code autocorrelation and linear FM chirp autocorrelation.

1. Barker Code Autocorrelation

A major class of autocorrelation sequences are called phase reversal codes.<sup>45</sup> These are unit amplitude sequences of  $N$  pulses, each of which has a phase of either  $0$  or  $\pi$ . An example of such a sequence, called a Barker code, is seen in Fig. IV-2(a). Also shown



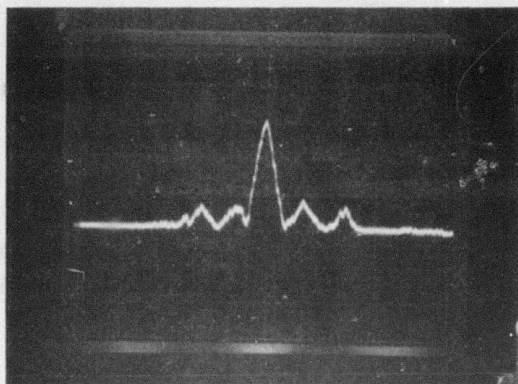


is the autocorrelation function of the Barker code and, for comparison the autocorrelation of a unit amplitude pulse of equal length. It is seen that the peak-to-sidelobe ratio and compression gain both equal the number of bits which in turn is close to the time bandwidth product of the code. Barker codes exist for lengths of 2, 3, 4, 5, 7, 11, and 13 bits.

Figure IV-3 and Table IV-2 give the result of Barker code autocorrelations for sequences of 5, 7, and 13 bits in length. The stored code was entered into the device as the modulation of a 101 MHz acoustic surface wave, and written into the diode array in the acoustic-plate mode with a  $\sim 5$  nsec plate pulse. Readout was obtained with a reversed code in the plate-to-acoustic mode.

Spurious responses are once again evident. It is also noted that the sidelobes tilt down in time. This is due to propagation loss and a perturbation in the propagation constant  $\beta$  due to the stored charge, as discussed in Appendix C.

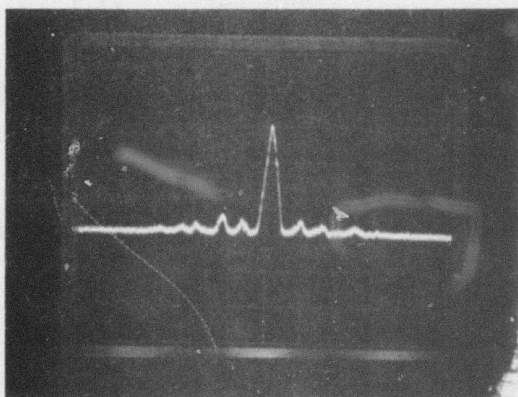
The experimentally observed peak/sidelobe ratios and correlation gains are close to the theoretical values, indicating that the device is capable of accurately storing the phase and amplitude of a 101 MHz signal and performing correlations with that signal.



BIPHASE BARKER  
CODE CORRELATION  
EXPERIMENTAL RESULTS

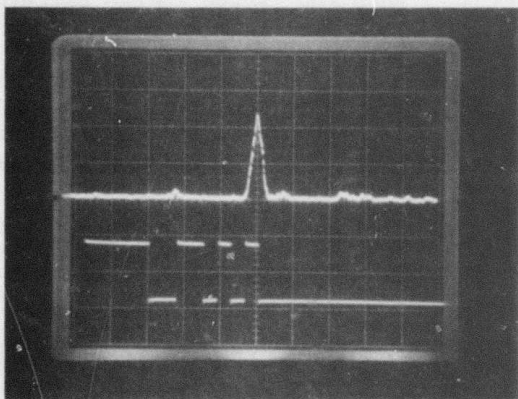
5 BITS: +++-+

( $2\mu\text{sec}/\text{div}$ )



7 BITS: +++--+-

( $2\mu\text{sec}/\text{div}$ )



13 BITS

+++++--++-+-

( $1\mu\text{sec}/\text{div}$ )

FIGURE IV-3



TABLE IV-2

## BARKER CODE CORRELATIONS

<u>Sequence</u>	<u>Peak/Sidelobe Theory</u>	<u>Ratio(dB) Experiment</u>	<u>Correlation gain <sup>*</sup>(dB)</u>	
			<u>Theory</u>	<u>Experiment</u>
5 bit(+++-+)	14.0	12	14	14
7 bit(+++--+)	16.9	15	16.9	16.9
13 bit(+++++-+++-+)	22.3	> 20(below spurious)	22.3	22

\* Defined as  $20 \times \log \left( \frac{\text{width of original sequence}}{\text{Full width @ 1/2 max. of autocorrelation output}} \right)$

#### ii. Linear FM Chirp Autocorrelation

We next consider the case when the stored charge pattern  $F(z)$  is a linear FM chirp of amplitude  $F_0$ , given by

$$F(z) = F_0(z) e^{j \left[ \frac{\omega z}{v_a} + \frac{\mu}{2} \left( \frac{z}{v_a} \right)^2 \right]} \quad (\text{IV-9})$$

The reading signal  $\phi_r(t)$  is also a linear FM chirp of amplitude  $\phi_{r0}$  with identical slope, so that it is given by

$$\phi_r(t) = \phi_{r0}(t) e^{j \left( \omega t + \frac{\mu t^2}{2} \right)} \quad (\text{IV-10})$$

The stored charge pattern and reading signal correlate, so that the output is given by substituting Eqs. (IV-9) and (IV-10) into Eq. (IV-6).

The result is

$$\phi_a(z, t) = Ke^{j\left[\omega(t - z/v_a) + (\mu/2)(t - z/v_a)^2\right]} \int_{-\frac{L}{2}}^{\frac{L}{2}} \phi_{ro}(\tau) F_o(\tau - t) e^{j\mu t \tau} d\tau \quad (IV-11)$$

where  $K$  is a constant. For the case when both  $\phi_{ro}$  and  $F_o$  are constant, so that neither the stored charge nor the reading signal is amplitude modulated, the integral in Eq. (IV-11) reduces to a sinc function. The ratio of the output  $\phi_a(z_t, t)$  to the peak output  $\phi_a(z_t, t = 0)$  seen with a transducer at position  $z_t$  is

$$\frac{\phi_a(z_t, t)}{\phi_a(z_t, t = 0)} = \text{sinc} \frac{utL}{2v_a} \quad (IV-12)$$

This is shown pictorially in Fig. IV-4.

Equation (IV-12) gives a measure of the width of the region on the diode array over which the frequency of the reading signal matches the frequency of the stored charge pattern. It is only in this region that a significant output signal is generated. This region moves down the diode array with a velocity  $v_a$ , equal to the acoustic velocity, as the reading chirp signal changes frequency. Thus, the excited surface wave readout signal builds up linearly under this region for the full readout time, giving rise to a sharply peaked output.

From Eq. (IV-12), the output is seen to be down from the peak by 4 dB when  $\mu t L / 2v_a = \pi/2$ . Thus, the full 4 dB width of the correlation output is

$$\Delta t = 2 t(4 \text{ dB}) = \frac{2\pi v_a}{\mu L} = \frac{1}{B} \quad (\text{IV-13})$$

where B is the chirp bandwidth, given by

$$B = \frac{\mu T}{2\pi} \quad (\text{IV-14})$$

where T is the chirp duration.

The compression ratio is

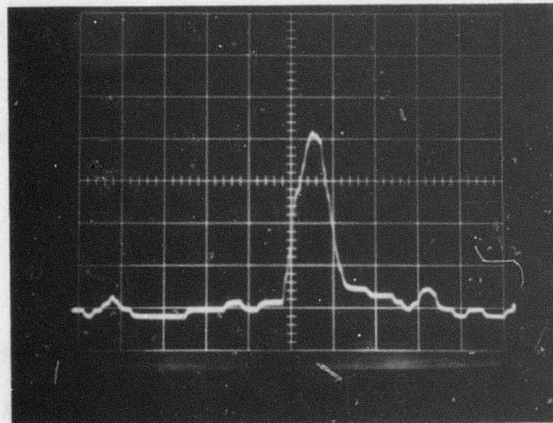
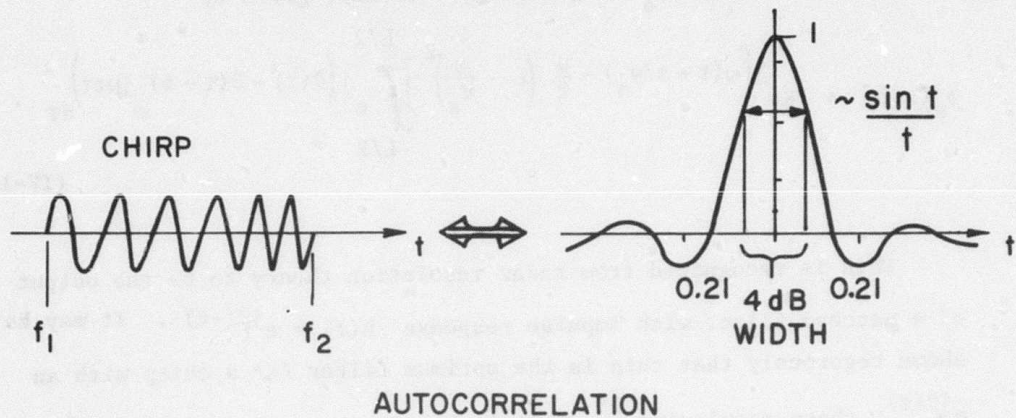
$$\frac{T}{\Delta t} = TB \quad (\text{IV-15})$$

The ratio of the original chirp length to the 4 dB width of the correlation peak is given by the time-bandwidth (TB) product. The TB product is seen to be a measure of the device's efficiency as a chirp compression filter.

Figure IV-4(b) shows the correlation of two 6  $\mu\text{sec}$  long,  $B = 15 \text{ MHz}$  linear fm chirps. The readout was obtained 1 msec after writing. The 4 dB width is about 70 nsec, so that the measured compression ratio corresponding to Eq. (IV-15) is  $6 \mu\text{sec}/70 \text{ nsec} = 86$ . The TB product is  $(6 \mu\text{sec}) \times (15 \text{ MHz}) = 90$ .



# CHIRP AUTOCORRELATION AND EXPERIMENTAL RESULT



100 nsec/div

CORRELATION OF  
TWO 15 MHz  
6  $\mu$ sec CHIRPS

(1 msec WRITING  
TO READING DELAY)

FIG. IV-4 FM Chirp Autocorrelation and  
Experimental Result.

### iii. Correlation of Phase Distorted Chirps

We now consider the correlation of two identical linear fm chirps which have been distorted by a phase modulation  $e^{j\theta(t)}$ . The acoustic output  $\phi_a$  is, from Eq. (IV-11), given by

$$\phi_a(z,t) = K e^{j\left[\omega(t - z/v_a) - \frac{\mu}{2} \left(t - \frac{z}{v_a}\right)^2\right]} \int_{-L/2}^{L/2} e^{j(\theta(\tau) - \theta(\tau - t))} e^{j\mu t \tau} d\tau \quad (IV-16)$$

This is recognized from radar resolution theory to be the output of a matched filter with impulse response  $h(t) = e^{j\theta(-t)}$ . It may be shown rigorously that this is the optimum filter for a chirp with an  $e^{j\theta(t)}$  phase modulation.<sup>45</sup> This is because at  $t = 0$ , as can be seen from Eq. (IV-16), the phase error  $\theta(\tau)$  is completely removed by the correlation process. So the peak amplitude of the correlation is not affected by phase distortion. In other words, the output S/N is maximized when the filter input is an fm chirp with a phase modulation  $e^{j\theta(t)}$ . This result holds as long as the modulation phase angle  $\theta(t)$  is slowly varying, so that the first derivative component is the principal term in its Taylor expansion.

This filtering performance is a consequence of the fact that the contribution to the total output from a particular region of the diode array is maximum when the reading signal frequency exactly matches the frequency of the readout charge stored in that region. A time varying phase modulation of the reading signal gives rise to frequency mismatches that reduce the readout efficiency. An identically phase modulated readout charge pattern will exactly compensate for this, thereby optimizing the correlation output.

It may be parenthetically noted that this process is essentially equivalent to one-dimensional holographic imaging and reconstruction, and has optical analogs. For example, Bloom and Bjorklund<sup>68</sup> have shown how interactions in a nonlinear optical medium may be employed to generate a phase grating matched to particular image aberrations. The resolution of distorted images reconstructed through interaction with the phase matched grating is nearly equal to that of reconstruction without distortions present.

Let us examine how the storage correlator can be employed as an ideal phase distortion filter to improve the resolution of a pulse echo system. By way of example, consider the ideal radar and sonar systems shown in Fig. IV-5. In either case, the echo from the target will have undergone phase distortion due to the propagating medium and either the transducer or antenna. Such distortion is not easily compensated for with a fixed filter due to difficulties in characterizing the distortion, and also because the distortion is a function of the operating environment, which is variable.

To compensate for phase distortion with the storage correlator, an identically distorted reference echo is stored in the device. This is obtained as a reflection from a reference plane in the case of a radar system, or from the end of a buffer rod in the sonar system. The storage correlator now becomes a filter matched to the system's particular phase distortion. A target echo signal passed through the storage correlator at any time after the reference signal is stored yields an optimum S/N correlation.



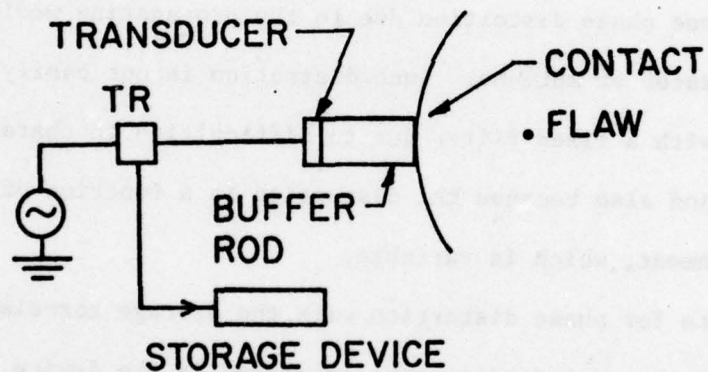
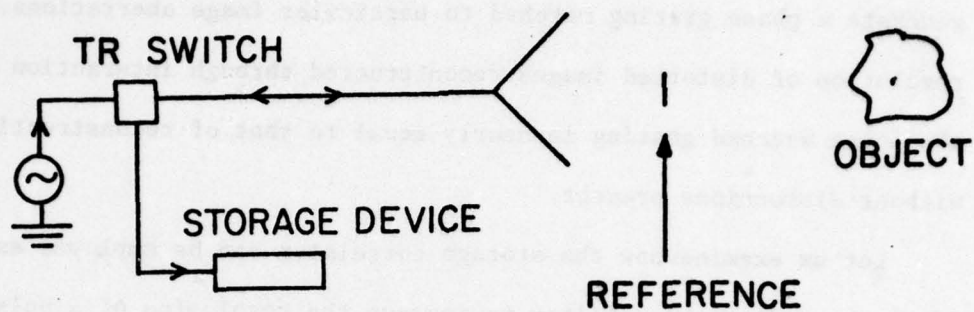


FIG. IV-5 Ideal Representations of Radar and Sonar Pulse-Echo Systems.

A practical application of this technique is the elimination of resolution deterioration due to poor transducer response in an acoustic pulse-echo system. To demonstrate this, a 3.25 MHz center frequency, 2.5 MHz bandwidth PZT transducer was placed 16 cm from a plastic block in a water tank, as illustrated in Fig. IV-6. The transducer was pulsed with a constant amplitude linear fm chirp. A 6  $\mu$ sec long, 2.5 MHz segment of the first reflected pulse from the plastic block was gated, mixed with 98 MHz, and stored in the storage correlator as a reference signal. A correlation was then obtained with the second echo pulse, which arrived 210  $\mu$ sec after the reference signal. The second echo was the triple transit echo that had reflected from the transducer face and then reflected a second time from the plastic block.

Figures IV-7(a),(b) show the correlation peak and, for comparison, the impulse response of the PZT transducer. The 4 dB full width of the correlation peak corresponds to a compression ratio of 13.5, compared with the TB product limit of 15.

The same experiment was tried a second time with a poor quality transducer that exhibited severe ringing in its impulse response. Figures IV-7(c),(d),(e) show the first reflected pulse, correlation peak, and transducer impulse response respectively. The correlation peak width is essentially the same as that obtained with the original high quality transducer. This indicates that the resolution of the pulse-echo system employing the storage correlator is much improved over that which could normally be obtained with a poor quality transducer that severely distorts the original input signal.

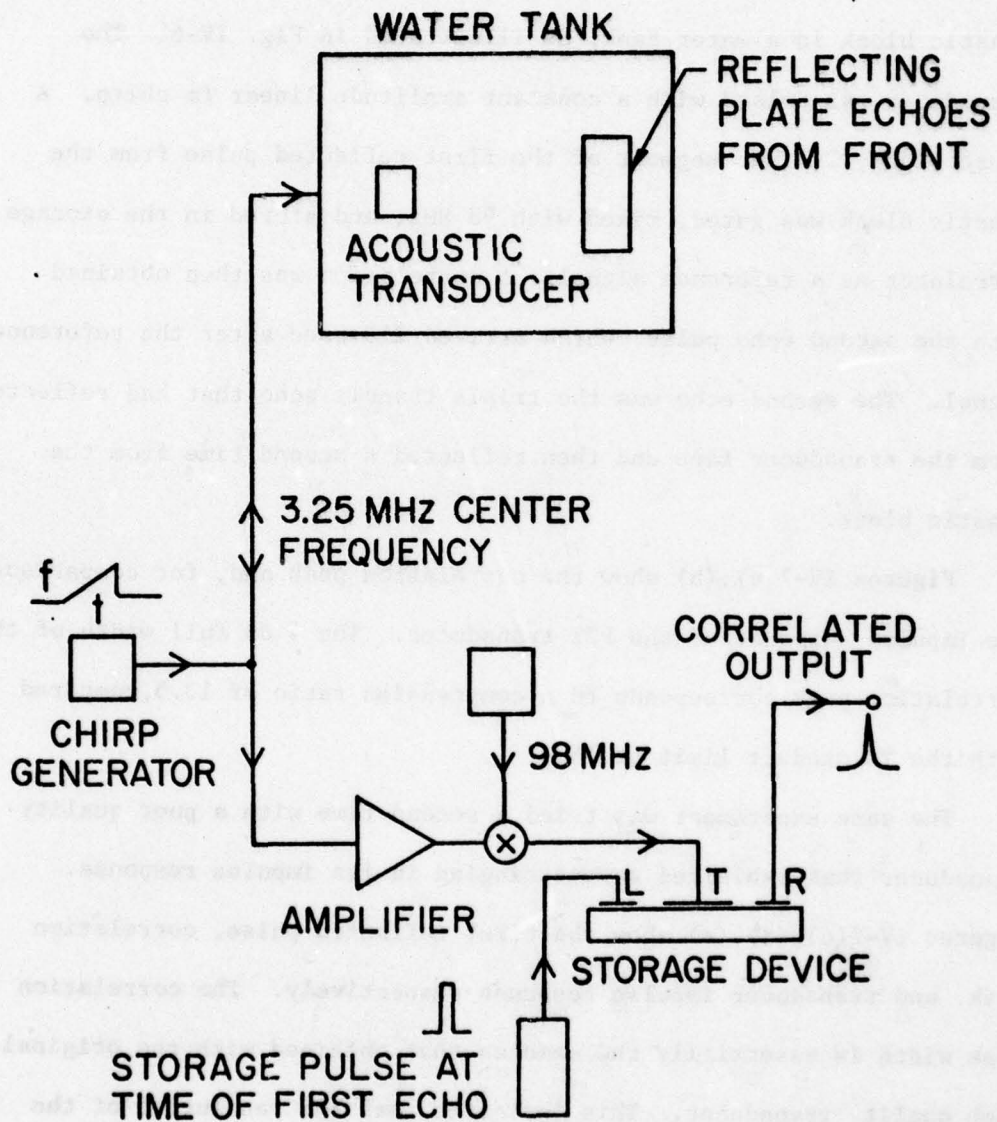
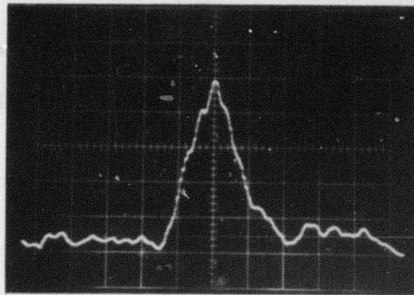


FIG IV-6 Schematic of the Acoustic Pulse-Echo System.



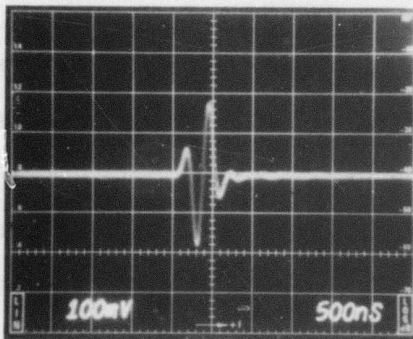
# GOOD TRANSDUCER

## (a) CORRELATION PEAK



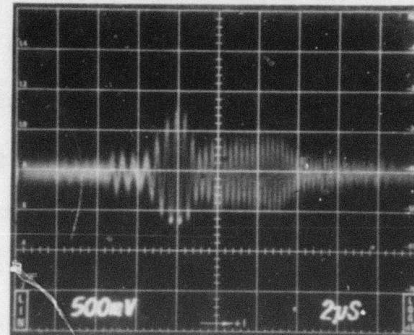
400 nsec/div → | ←

## (b) IMPULSE RESPONSE



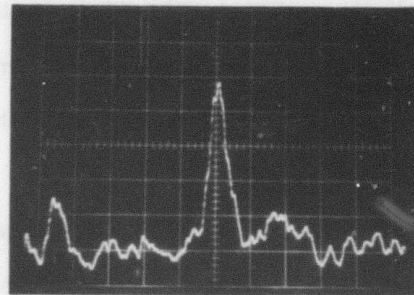
# POOR TRANSDUCER

## (c) FIRST REFLECTION



2 MHz 4.5 MHz

## (d) CORRELATION PEAK



1 μsec/div → | ←

## (e) IMPULSE RESPONSE

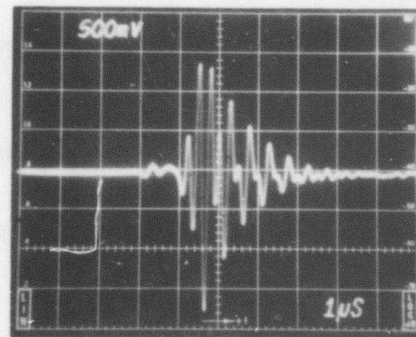


FIG. IV-7. Pulse-echo experiment results with both good and poor transducers.

The improvement in S/N is also significant. Figure IV-8 shows the sequence of reflections on the lower trace. The initial peak and ringing is due to the transmission of the original signal. The peak seen directly below the first gate pulse is the first reflection, which was stored as the reference signal. The second peak is the second reflection, used to obtain the correlation peak shown in Fig. IV-7(b). The peak below the second gate pulse is the third reflection. To demonstrate the system's ability to pick signals out of the noise, this third reflection signal was correlated with the stored reference, yielding the correlated peak shown in Fig. IV-8(b).

While the third reflection is buried in the transmitter feedthrough noise, with a  $S/N \leq 3$  dB, the correlation peak in Fig. IV-8(b) is clearly distinguished, and has a  $S/N > 10$ .

This sort of S/N enhancement is also seen in the results obtained with the poor transducer. Figure IV-8(c) shows the second reflection signal that was used to correlate with the stored reference signal, shown in Fig. IV-7(c), to produce the correlation peak of Fig. IV-7(d).

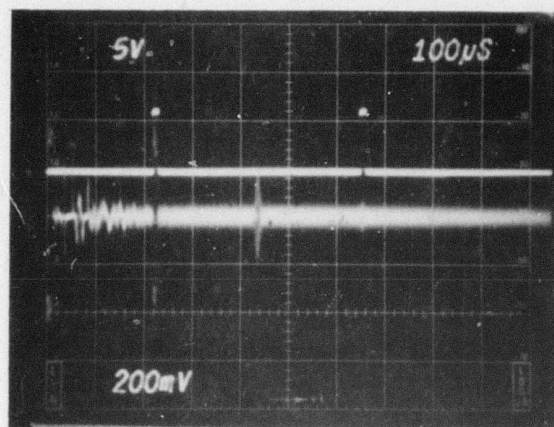
#### iv. Transform Processing

If the modulation of the stored charge pattern,  $F_o(z)$  is constant, then Eq. (IV-11) reduces to

$$\phi_a(z,t) = K F_o e^{j\left[\omega(t-z/v_a) - \mu/2(t-z/v_a)^2\right]} \int_{-L/2}^{L/2} \phi_{ro}(\tau) e^{j\mu t \tau} d\tau. \quad (IV-17)$$

The modulation of the output is now proportional to the Fourier transform of the modulation of the reading chirp signal,  $\phi_{ro}(t)$ . Thus, the storage correlator may be used as a real time Fourier transformer.



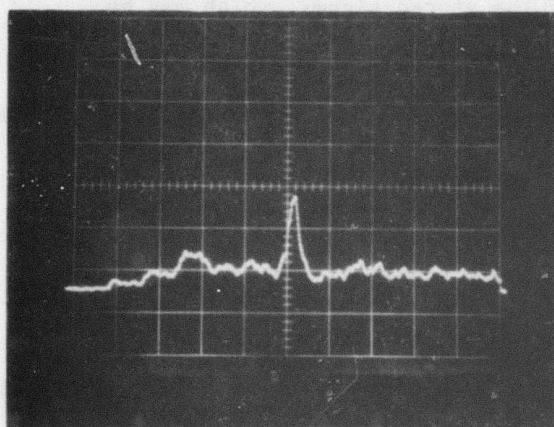


(a)

GATE SIGNAL

GOOD TRANSDUCER  
OUTPUT

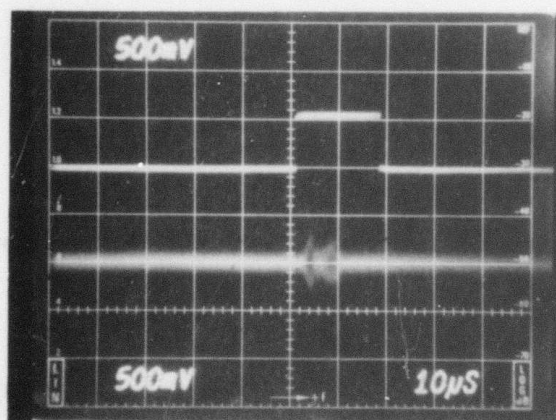
- (1) TRANSMITTED PULSE
- (2) REFERENCE ECHO
- (3) 2<sup>nd</sup> REFLECTION
- (4) 3<sup>rd</sup> REFLECTION



(b)

CORRELATION OF  
REFERENCE ECHO WITH  
THIRD REFLECTION

2  $\mu$ sec / div



(c)

GATE SIGNAL

POOR TRANSDUCER  
2<sup>nd</sup> REFLECTION  
CORRELATED WITH  
FIRST REFLECTION  
(FIG 4-7c) TO OBTAIN  
CORRELATION PEAK  
(FIG 4-7d)

FIG. IV-8. Pulse-Echo Experiment Results Showing S/N Gain of the System.



An example of transform processing: The analog pulse expander.

Consider transform processing when the reading chirp duration is not equal to the duration of the stored signal. As a particular example, we consider how the storage correlator may be used as an analog pulse expander.

We store the signal to be expanded and read this signal back out with a long chirp of slope  $\mu_R$ , as shown in Fig. IV-9(a). This yields the Fresnel transform of the stored signal, which may be retransformed with a dispersive delay line. Through the relation between the reading chirp slope  $\mu_R$  and the corresponding slope of the dispersive delay line impulse response, it is possible to expand the stored signal.

We assume a stored charge pattern  $F(z/v_a)$  of the form

$$F(z/v_a) = F_o(z/v_a) e^{-j\beta z} \quad (\text{IV-18})$$

and a reading signal of the form

$$\phi_{pr} = A e^{-j(\omega t + \mu_R t^2/2)},$$

where  $A$  is a constant. Substitution into Eq. (II-48) yields the signal seen at the output transducer to be

$$\phi_a(t) = K A E^{-j(\omega t + \mu_R t^2/2)} \int F_o(\tau) e^{-j[\mu t \tau + \mu_R \tau^2/2]} d\tau. \quad (\text{IV-19})$$

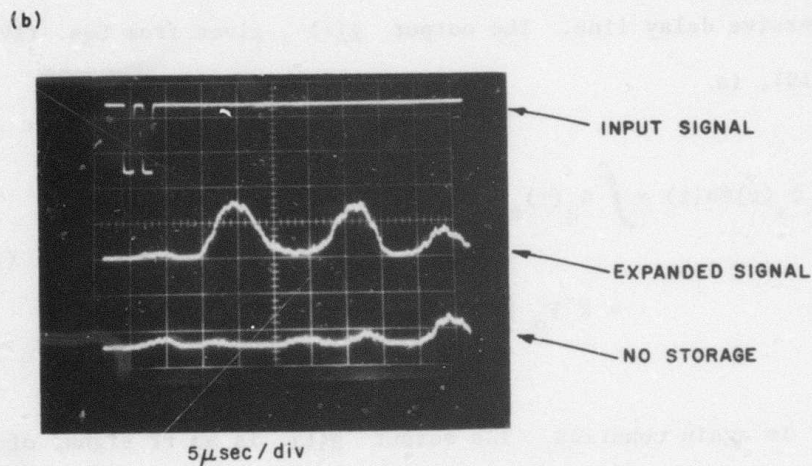
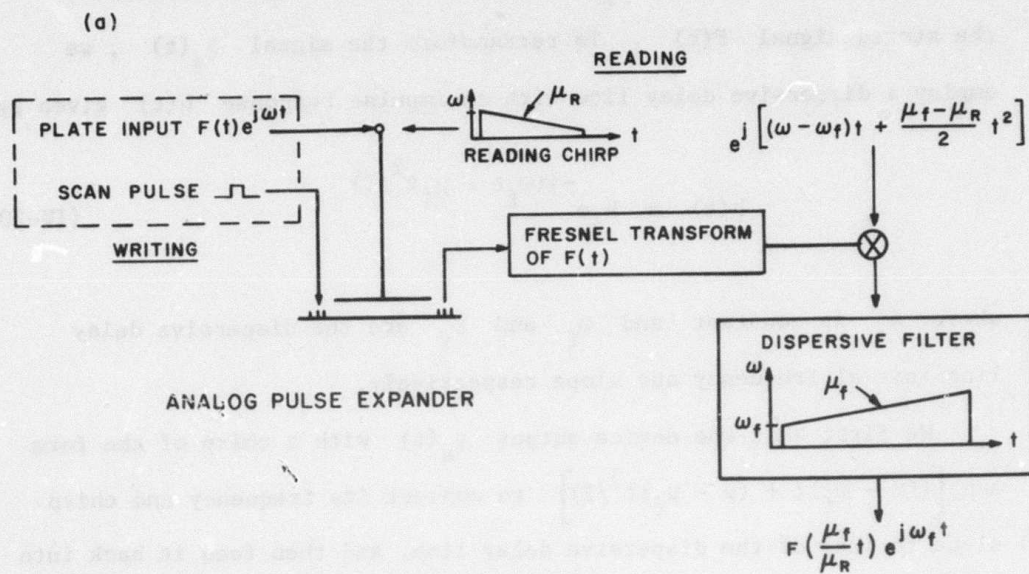


FIG. IV-9 The Analog Pulse Expander System and an Experimental Result.

This is a chirp of slope  $\mu_R$  modulated by the Fresnel transform of the stored signal  $F(t)$ . To retransform the signal  $\phi_a(t)$ , we employ a dispersive delay line with an impulse response  $h(t)$  given by

$$h(t) = h_0 e^{-j(\omega_f t - \mu_f t^2/2)} \quad (\text{IV-20})$$

where  $h_0$  is constant and  $\omega_f$  and  $\mu_f$  are the dispersive delay line initial frequency and slope respectively.

We first beat the device output  $\phi_a(t)$  with a chirp of the form  $\exp j[(\omega - \omega_f)t + (\mu - \mu_f)t^2/2]$  to convert its frequency and chirp slope to that of the dispersive delay line, and then feed it back into the dispersive delay line. The output  $g(t)$ , given from Eqs. (IV-20) and (IV-19), is

$$\begin{aligned} g(t) &= \phi_a(t) * h(t) = \int \phi_a(\tau) e^{j[(\omega - \omega_f)\tau - \frac{\mu - \mu_f}{2} \tau^2]} h(t - \tau) d\tau \\ &= K' F_0 \left( \frac{\mu_f}{\mu_R} t \right) e^{j\omega_f t} \end{aligned} \quad (\text{IV-21})$$

where  $K'$  is again constant. The output  $g(t)$  is an rf signal of frequency  $\omega_f$  with modulation proportional to the original signal  $F_0(t)$  scaled in time by the ratio of the dispersive delay line impulse response slope  $\mu_f$  to the reading chirp slope  $\mu_R$ . Note that for  $\mu_R > \mu_f$ , the signal  $F_0(t)$  is expanded and for  $\mu_R < \mu_f$ , the signal  $F_0(t)$  is contracted.

Figure IV-8(a) shows a schematic of the implementation of this scheme and an actual result. The reading chirp initial frequency was



$\omega_0 = 107.5$  MHz , the slope was  $\mu_R = 0.16$  MHz/ $\mu$ sec , and the bandwidth was 20 MHz, corresponding to a duration of 125  $\mu$ sec. The filter chirp slope was  $\mu_f = 0.02$  MHz/ $\mu$ sec, so that the theoretical expansion is  $\mu_R/\mu_f = 8$  . The observed expansion of the 4  $\mu$ sec long double pulse shown on the top trace of Fig. IV-9(b) is about 6.5. Also shown for comparison is the device output with no stored charge.

#### 4. Input Correlation

Until now, this discussion has focused on correlation during reading. It is also possible to correlate two input signals during writing, a process called input correlation.<sup>16,17,50,51</sup> Input correlation removes the constraint on the correlation signal duration imposed by the limited length of the interaction region. This is simply because the diode array is used to store only the compression peak, rather than the full correlation signal. Now, the storage time limits the duration of the signals, so that extremely high TB correlations can be performed with even short devices.

We consider acoustic-plate or, equivalently, acoustic-acoustic writing, where writing occurs through the interaction of two long duration rf signals. Chapter II gave both a qualitative and analytic description of this process. Here, we consider the situation where both input signals are phase modulated. For the case of acoustic-plate writing, the plate signal is of the form

$$v_p = v_{p0} e^{j(\omega t + \theta_p(t))} \quad (\text{IV-22})$$

and the acoustic signal is

$$V_a = V_{a0} e^{j(\omega t - \beta z + \theta_a(z,t))} \quad (\text{IV-23})$$

where  $\theta_p(t)$  and  $\theta_a(z,t)$  are the plate and acoustic signal phase modulation angles respectively. The assumptions here are identical to those of Chapter II for charging with low level rf signals. That is, the acoustic signal is assumed dominant, with successive peaks in its amplitude weakly turning on the diode. The diode conduction current near these peaks is due to both the acoustic and plate signal amplitudes; it is this current that gives rise to the stored charge.

Only the stored charge component with spatial period corresponding to the reading signal contributes to the observed readout. Such a component is stored only when the plate signal shifts phase by exactly  $2\pi$  in the interval between successive peaks of the acoustic signal. Thus, from Eqs. (IV-22) and (IV-23),

$$\omega t + \theta_p(t) = \omega t_{pm} - \beta z_n + \theta_a(z,t) + 2k\pi \quad (\text{IV-24})$$

$k = \text{integer},$

where  $z_n$  is the position of the  $n^{\text{th}}$  diode and  $t_{pm}$  is the time of the  $m^{\text{th}}$  acoustic amplitude peak.

If the plate and acoustic signals are constant in frequency, there is no phase modulation,  $\theta_a = \theta_p = 0$  and successive peaks of the acoustic signal occur at the intervals of  $2\pi/\omega$ . From Eqs. (IV-22)

and (IV-24), it is seen that the stored charge pattern has a spatial phase variation  $e^{j\beta z_n}$ . This was the case considered in Chapter II.

If the acoustic plate signals are linear fm chirps of initial frequency  $\omega_0$  and slope  $\mu$ , Eq. (IV-24) now becomes

$$\omega_0 t + \frac{\mu}{2} t^2 = \omega_0 \left( t_{pm} - \frac{z_n}{v_a} \right) + \frac{\mu}{2} \left( t_{pm} - \frac{z_n}{v_a} \right)^2 \quad (IV-25)$$

where  $v_a$  is the acoustic propagation velocity, so that  $\beta = \omega/v_a$ . We here ignore the insignificant  $2k\pi$  phase in Eq. (IV-24). At the position  $z_n = 0$ , Eq. (IV-25) reduces to equality with  $t = t_{pm}$ . It is at this position that the acoustic and plate signal frequencies exactly match during the entire charging interval; in the neighborhood of this position a correlation charge pattern is stored.

Moving away from this point, the sampling becomes out of phase by an amount

$$\Delta\phi = \frac{\mu}{2} \left( \frac{z_n}{v_a} \right)^2 - (\omega_0 + \mu t_{pm}) \left( \frac{z_n}{v_a} \right) \quad (IV-26)$$

Over the full charging time  $T$ , this phase shift causes the spatial variation of the stored charge to average out to zero for even small distances from  $z_n = 0$ . Thus, the correlation charge pattern will be sharply peaked.

The stored charge pattern is of the form



$$\begin{aligned}
Q_s(z) &= Q_o \int_{-\frac{T}{2}}^{\frac{T}{2}} e^{j\left[\omega_o(t_{pm} - z_n/v_a) + \mu/2(t_{pm} - z_n/v_a)^2\right]} e^{-j\left[\omega_o t_{pm} + \mu t_{pm}^2/2\right]} dt_{pm} + c.c. \\
&= Q_o e^{-j\left[\omega_o(z_n/v_a) - \mu/2(z_n/v_a)^2\right]} \int_{-\frac{T}{2}}^{\frac{T}{2}} e^{-j\mu(z_n/v_a)t_{pm}} dt_{pm} \quad (IV-27) \\
&= Q_o e^{-j\left[\omega_o(z_n/v_a) - \mu/2(z_n/v_a)^2\right]} \frac{\sin\left(\frac{\mu T z_n}{v_a}\right)}{\left(\frac{\mu T z_n}{2 v_a}\right)} + c.c.
\end{aligned}$$

where linear charging is assumed and  $Q_o$  is constant. The sinc  $(\mu T z_n / 2 v_a)$  shape of the stored charge pattern is exactly that observed with output chirp correlation. The compression ratio is again given by the TB product, as discussed in Section 3(a). Note that this can be quite large, since the chirp duration  $T$  can be a millisecond or longer. Its length is limited only by the storage time of the device, whereas the chirps employed for output correlation are only a few microseconds long.

The stored charge pattern may be directly read out by applying a plate pulse with center frequency  $\omega_o$  and a bandwidth greater than that of the stored charge pattern. The 4 dB halfwidth of this pattern is seen from Eq. (IV-27) to be given by the condition

$$\frac{\mu T z_n}{2 v_a} = \frac{\pi}{2}$$

so that the bandwidth of the reading pulse must be at least  $\mu T$  , which is simply the bandwidth of the input chirps.

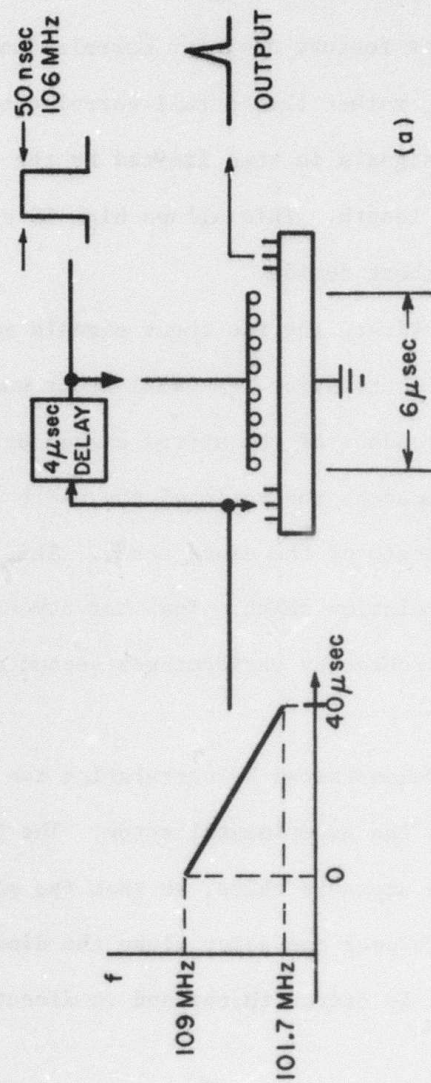
To summarize, the significant feature of input correlation is that only the narrow correlation peak, rather than a full correlation signal, is stored. The duration of the signals is thus limited by the storage time rather than the diode array length. This allows high TB correlations to be performed in even a short device.

The drawbacks are twofold. First, the two input signals must be synchronized in time so that the correlation peak will occur under the diode array. Second, in direct readout of the stored charge pattern, the signal-to-noise ratio is reduced by the ratio of the width of the stored correlation peak to the length of the diode array. This may result in low S/N for narrow correlation peaks. Tuan has demonstrated a technique for overcoming this problem by performing a second correlation during reading.<sup>17</sup>

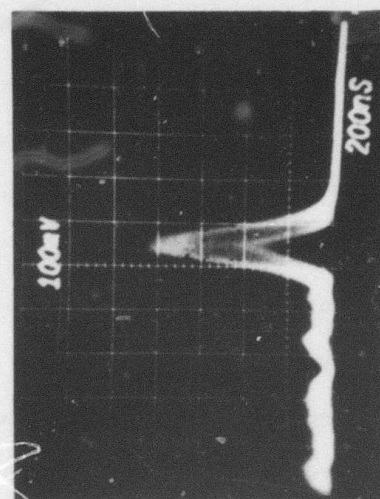
Input correlation has been demonstrated by correlating two linear fm chirps. Figure IV-10(a) shows the experimental setup. The plate chirp is a delayed replica of the acoustic chirp, so that the plate and surface wave frequencies match near one point along the diode array. The correlation peak will be stored there, and is directly read out later.

The device had a center frequency of 105.5 MHz and a 3 dB bandwidth of about 7 MHz. The mesa  $p^+n$  diode array length was 2 cm (about 6  $\mu$ sec). The acoustic and plate inputs were both 40  $\mu$ sec, 7.3 MHz linear fm chirps with a center frequency of 105.4 MHz .

FIG. IV-10 Input Correlation Setup and Experimental Result.



(a)



(b)



To obtain the plate delay, a linear FM chirp was generated and mixed up in frequency before being applied to the plate. The readout appeared at a surface wave transducer in response to a 50 nsec rf pulse applied to the plate after a 60  $\mu$ sec delay. Both plate signal amplitudes were 8 V 0-p . The acoustic signal power was 23.5 dBm and the minimum 2-port delay line loss was 18.5 dB at 106 MHz.

The correlation output is seen in Fig. IV-10(b). The 4 dB width, assuming a  $\text{sinc}(\mu T t/2)$  shape, is 160 nsec, corresponding to a compression ratio over the original 40  $\mu$ sec inputs of 250. The theoretical compression, corresponding to the TB product, is  $40 \mu\text{sec} \times 7.3 \text{ MHz} = 292$  . It should be noted that the output is actually the convolution of the 50 nsec readout pulse with the stored charge pattern, thus broadening the output about 10% over the true correlation charge pattern.

Nevertheless, the performance improvement is dramatic. In the output correlation mode, the peak compression obtainable is limited by the diode array length and transducer bandwidth to about  $6 \mu\text{sec} \times 7.3 \text{ MHz} = 44$  , or about 20% of that obtained through input correlation.

We finally consider some of the limitations of input correlation. Most obvious is that it is only usable for pulse compression, since the available storage length is often only a small fraction of the length of the full correlation.

The technique is not suited, in its present form, to amplitude dependent correlations. As was shown in Section 3 (b) and (c) of Chapter II, the charge buildup in time is a strong exponential function of the amplitudes of both input signals, so that linear correlation of

signals with even small amplitude variations is difficult. This amplitude nonlinearity is less critical in phase dependent correlations, since phase mismatches build up rapidly with distance from the correlation peak. These tend to cancel over sufficiently short times, so that the signal amplitude variations may only slightly broaden the correlation peak. The linear dynamic range for input correlation is expected to approximately correspond to that for charging with two rf signals. From the results of Chapter II, Section 3(c) and (d), the expected output dynamic range is about 40 dB. In practice, an even greater output dynamic range may be usable because phase cancellations can occur over short segments of the charging interval even as saturation is approached. Because of the nonlinear dependence on input signal amplitude, the input dynamic range is not meaningful in this case.

#### 5. Limitations Due to the Device Structure

This section discusses limitations on the use of the storage correlator as a signal processor imposed by intrinsic structural factors. These include charging and storage time limits, and degrading factors such as phase mismatches, losses, nonuniformities, and spurious signal excitation.

##### (a) Charging and Storage Time Limitations

Because separate design constraints may dictate the writing and storage time requirements for a given storage correlator application, it is important to discuss the relationship between the writing and storage times. In Chapter II, the theory of writing into  $p^n$

diodes was discussed in detail. It was shown that the charging mechanism is minority carrier drift across the depletion layer. This is independent of the generation and recombination processes that determine the storage time. As a result, it was concluded that  $p^+n$  diodes have the following properties:

1.  $p^+n$  diodes can be charged to 75% of the maximum value with a single pulse of sufficient amplitude and a duration less than  $1/2$  rf cycle.
2. For small amplitude pulses, the stored charge varies logarithmically with time. Thus, the charging rate can be very slow.

These properties were verified by the experimental results shown in Figs. II-6 and II-7 for single pulse charging and Figs. II-10 and II-11 for slow charging.

Here one more experiment is described, proving that a very long storage time diode can be charged with a very short pulse of sufficient amplitude. The device is the same as that used to obtain Fig. II-11, where it was charged in a period of about 10 msec. It employed a mesa  $p^+n$  diode array with a room temperature storage time of 35 msec. The frequency was 108 MHz and the charging pulse length was about 5 nsec. As shown in Fig. IV-11 while the storage time varied by more than three orders of magnitude, the charging characteristics remained almost constant over a  $64^\circ\text{C}$  temperature range. This is expected from Eq. (II-21), since the intrinsic carrier concentration  $P_{n0} = n_i^2 \propto T^3 \exp(E_g/kT)$ ,<sup>39</sup> where  $E_g$  is the bandgap energy, so that the diode voltage is virtually independent of the temperature  $T$ .



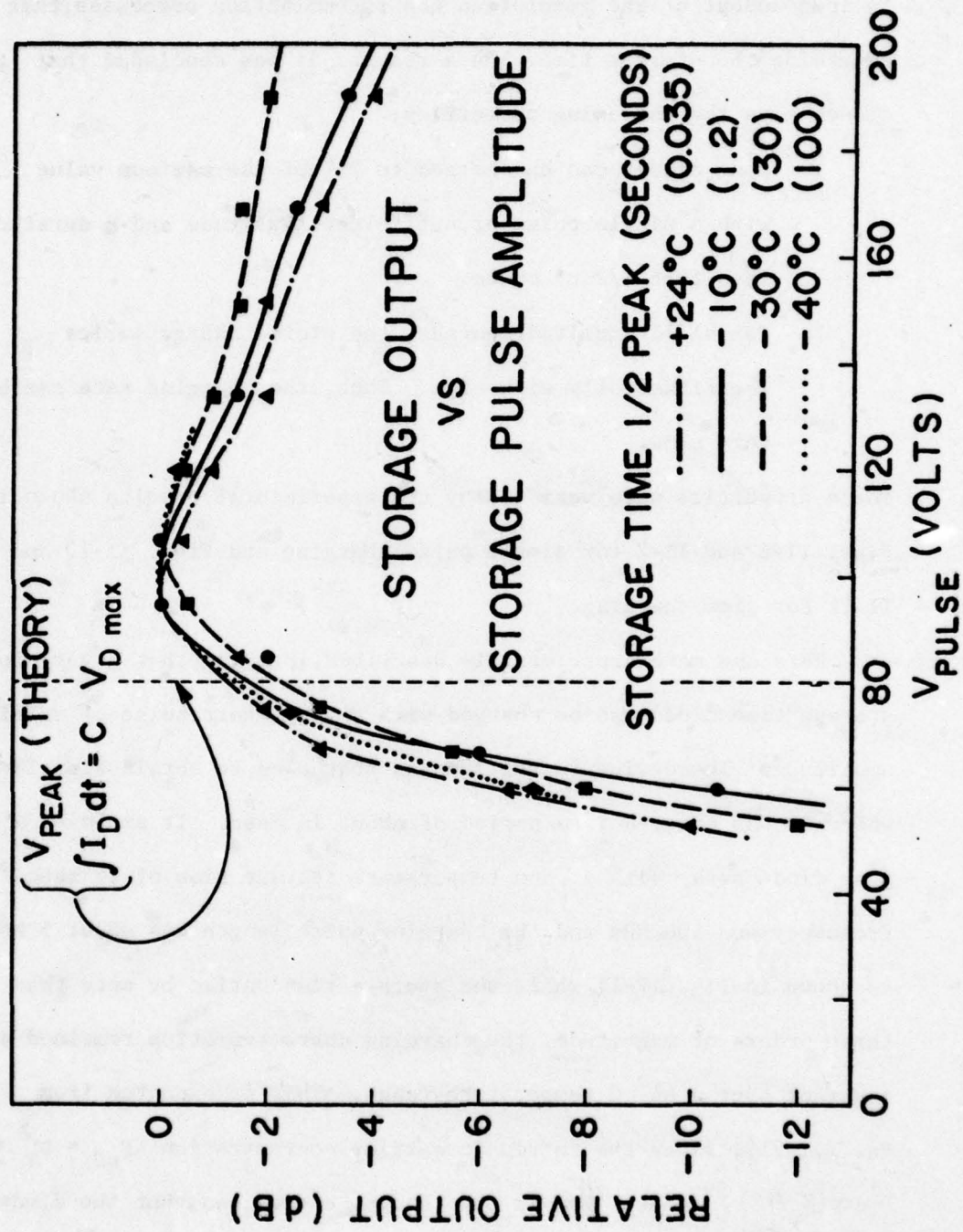


FIG. IV-11 Device Output as a Function of the Charging Pulse Amplitude for Various Temperatures.

It is important to note that fast charging behavior is seen only with writing signals of sufficient amplitude. Because of the low maximum power limits of interdigital surface wave transducers, the high amplitude charging signal must take the form of a short voltage spike of typically  $> 100$  volts amplitude. It is suggested that others have observed  $p^+n$  diodes to be slow devices simply because those results were due to the low levels of the charging signals, and not to any inherent physical limitations of the diodes.<sup>18</sup>

It should, of course, be asked whether a long storage time is necessarily desirable for signal processing applications. In radars and many sonars, propagation delay times are short, typically a few msec or less. In such cases, a long storage time is of no value, and can even be disadvantageous.

This is because the writing repetition rate must always be slower than the complete discharge time. Otherwise, residual charge will interfere with the writing of the new charge pattern, since successive writing cycles are usually unsynchronized in rf phase. Excessive writing repetition rates can cause jitter in the readout signal. In writing with long rf signals, residual charge will significantly shorten the charging time. This limits the dynamic range and correlation gain of an input correlation.

It is possible to increase the repetition rate when using long storage time diodes by erasing the residual charge with a flood of light. The light generates sufficient carrier pairs to short out the depletion regions, thereby discharging the diodes.<sup>53</sup>

A long storage time is of no advantage in performing long input correlations. This is because the saturation current governing the charging characteristics, as given by Eq. (II-38), is due to minority carrier drift across the depletion region. Thus, just as in the fast charging case, the charging and storage times are essentially independent.

An important application of long storage time diodes is in imaging. Here, high sensitivity is obtained by integrating photocurrents over long times. The leakage current must be much less than the lowest photocurrent in this application.<sup>18,53</sup>

#### (b) Degrading Factors

This section briefly summarizes some of the factors that can lead to deterioration in performance. These include phase mismatches due to the presence of the diode array, loss, nonuniformities, and spurious signal excitation.

Phase mismatch between writing and reading occurs because the stored charge perturbs the surface wave propagation, as discussed in Appendix C. This effect is usually weak, although it may be significant when the delay between writing and reading is short, or when the air-gap is small so that the diode array-to-surface wave coupling is strong.

We may evaluate the lumped effects of nonuniformities and insertion loss by assuming some spatial variation in the correlation integral due to these effects. Consider the case of plate-to-acoustic reading with the acoustic output potential  $\phi(z,t)$  given by Eq. (II-48). With a nonuniformity function  $F(z)$  Eq. (II-48) becomes



$$\phi_a(z,t) = j\gamma e^{-j\gamma z} \int F(z') \phi\left(z', t - \frac{z' + z}{v_a}\right) e^{j\gamma z'} dz' \quad (\text{IV-28})$$

Assuming a constant charge pattern and reading signal modulation, Eq. (IV-28) reduces to

$$\phi_a(z,t) = e^{-j(\omega t - \beta z)} \int_{\text{interaction region}} F(z') dz' \quad (\text{IV-29})$$

In this simplest case, the signal seen by the output transducer is a surface wave modulated by the integral of the nonuniformity function  $F(z)$ . For  $F(z) = 1$ , the case of a perfectly uniform interaction region and no loss, the output varies linearly with the interaction region length. For an exponential loss of the form  $F(z) = F_0 e^{-\alpha z}$ , where  $\alpha$  is the attenuation coefficient and  $F_0$  is a constant, the output would be reduced by a factor  $F_0(1 - e^{-\alpha z})/\alpha$ . In practice,  $\alpha$  is small and the distortion due to loss is tolerable. It could, however, be a significant factor for devices with very long diode arrays.

An important source of attenuation of the surface wave is the presence of the diode array. This takes the form of both mass loading and transverse current flow in response to the surface wave's electric fields that extend into the semiconductor. Joly has considered both of these effects.<sup>27</sup> It may be experimentally shown that with the Joly convolver configuration, mass loading can be reduced to insignificant levels. The electrical attenuation is not easy to quantify in

practice, since it is a function of interdiode coupling and the detailed properties of the diode array. In practice, devices have been demonstrated with  $\pm 1$  dB uniformity over a 2 cm interaction region (the airgap was  $3000 \text{ \AA}$ ). This high uniformity may in part be due to the fact that, when opposite transducers are used for reading and writing, losses incurred during writing tend to be compensated during reading. It is possible that losses of this sort could present a more serious problem in very long devices with narrow airgaps.

Nonuniformities are not generally characterizable since they vary from device to device. In practice, the current spacer rail or post<sup>7</sup> airgap technologies allow devices to be assembled with sufficient uniformity that airgap and diode array nonuniformities do not present a serious problem.

Spurious signal excitation during reading is by far the worst source of signal distortion in the airgap device as it exists today. This limits the low end of the input dynamic range and distorts the output signal, as seen in all the experimental results presented here. Techniques for its reduction are discussed at length in Chapter III.

## CHAPTER V

### CONCLUSIONS

This work had three principal objectives. First was the development of a complete analytic theory of the storage correlator, valid for all device structures and modes of operation. Second was the demonstration of a device with sufficient dynamic range to allow both verification of the theory and use as a signal processor. Third was the demonstration of a wide variety of signal processing applications. In total, these objectives are tantamount to developing the understanding and technology of the storage correlator, so that it will be an attractive candidate for the application in real signal processing systems.

The theory presented in Chapter II provides concise analytic results that compare well with experiment for a wide range of operational modes and structures. Most features of performance are predicted, and the physics of device operation is well understood.

The experimental device exhibits nearly theoretical signal processing performance in a number of diverse applications. Among these is the first true system application of a storage correlator as a phase distortion filter in an acoustic pulse-echo system. A technique for correlation of input signals has been demonstrated, allowing the correlation of very long signals to achieve extremely high time-bandwidth products.

In summary, the storage correlator is almost ready for use as a real signal processing device. Nevertheless, a number of serious problems still remain. The worst of these is acoustic spurious



signal generation during reading. As described in Chapter III, a number of suppression techniques were developed, ultimately yielding a spurious limited dynamic range of no better than 36 dB. This is at least 14 dB below the level needed for a good general purpose signal processor. To achieve the desired spurious suppression, it will probably be necessary to employ still more sophisticated techniques. These might include two channel devices coupled by multistrip couplers, or monolithic structures with very thin piezoelectric layers.

A second drawback is that high amplitude plate signals are required due to the voltage drop across the thick piezoelectric substrate. This problem is not always as serious as it appears, and may be alleviated with the use of appropriate plate matching networks and avalanche transistor pulsed. Thin  $\text{LiNbO}_3$  crystals are extremely fragile. A practical structural alternative appears to be a monolithic device with a thin piezoelectric film.

Such a device has, in fact, recently been demonstrated by Tuan.<sup>25</sup> This consists of a  $1.6 \mu\text{m}$  piezoelectric film sputtered over a planar  $\text{p}^+\text{n}$  diode array. Interdigital transducers are then fabricated at each end. The operation is essentially equivalent to that of the  $\text{LiNbO}_3/\text{Si}$  device. This monolithic device readily yields a spurious limited dynamic range in excess of 40 dB. The turn on voltage is less than 3 volts.

It is entirely likely that the storage correlator will find application in an area that has not so far been discussed; namely, imaging processing.<sup>26,53</sup> Here, depletion layer photocurrents are used to discharge illuminated diodes, thereby modulating a stored charge pattern with an image. The photocurrent may be integrated over the device storage time

to obtain high sensitivity. Furthermore, the image may be either directly read out, or processed by techniques similar to those discussed in Chapter IV.

Consider, for example, the case of a stored linear FM chirp. Light is now shined on the diode array, so that the charge pattern  $Q(z)$  is

$$Q(z) = (Q_0 - \rho(z,t)) \cos \left[ \frac{\omega_0 z}{v_a} - \frac{\mu}{2} \left( \frac{z}{v_a} \right)^2 \right]$$

$$Q_0 - \rho(z,t) \geq 0$$

where  $\rho(z,t)$  is the density of carriers generated by light. If the reading signal is a second chirp also of slope  $\mu$ , then the output voltage has a component

$$\int_{\text{array}} \rho(z,t) e^{j\mu t z/v_a} dz .$$

This is the Fourier transform of the image pattern  $\rho(z,t)$ .

The ability to obtain the real time Fourier transform of an image is of particular importance in narrow-band imaging systems, allowing image filtering in the frequency domain.

Another possible development is the two dimensional storage correlator. This would essentially square the storage density. One approach is to construct a device with a number of parallel channels, which may then be addressed serially. A second technique may be to write information into an area with two orthogonal surface waves. The stored charge pattern retains the vector sum of the propagation vectors of the two writing

surface waves. The readout surface wave will have the sum propagation constant. A third approach, employing phase coded transducers, has been demonstrated by Ingebrigtsen.<sup>12</sup> Here, a single device channel may be used to store multiple signals, each of which is orthogonal to the others. The orthogonality is obtained by phase coding the input and output transducers.

Evidently, the storage correlator is a device whose full potential is yet to be realized. Several groups are continuing development along many of the avenues discussed here. It is hoped that the theoretical and experimental results of this study will aid those who wish to develop or apply this device in the future.



# APPENDIX A

## CIRCUIT MODEL DEVELOPMENT

### 1. Charging Circuit

In this appendix we develop the charging circuit model. We shall consider first the electrical coupling of the surface wave to the diodes, and then the coupling of externally applied plate potentials to the diodes. These are finally combined into a complete circuit model that may be reduced with appropriate assumptions.

#### (a) The Acoustic Circuit.

Joly<sup>27</sup> has shown that the coupling of the fundamental propagating acoustic mode potential,  $\phi_a$ , exciting the semiconductor may be modeled as shown in Fig. A1. This model arises directly from Eqs. (9), (18), (19), (21) and (86) of reference 58 and Eq. (36) of reference 57 when it is assumed that the semiconductor surface is continuous and uniform. Here,  $\phi_a$  is given by the expression

$$\phi_a = \sqrt{2 Z_a P_a} \quad (A-1)$$

where  $P_a$  is the power of the surface wave and  $Z_a$ , the acoustic impedance, is

$$Z_a = \frac{2}{w\omega(\epsilon_{pa} + \epsilon_o)} \left| \frac{\Delta v}{v_a} \right| e^{-2\beta h} \quad (A-2)$$

where  $w$  is the acoustic beam width,  $\omega$  the frequency,  $\beta$  the propagation constant,  $h$  the airgap height, and  $\left| \frac{\Delta v}{v} \right|$  is the fractional

# THE ACOUSTIC CIRCUIT (FROM JULY<sup>27</sup>)

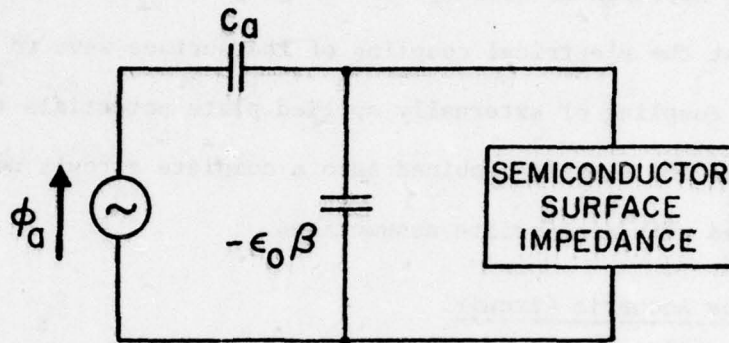


FIG A-1 The Acoustic Curcuit (from Joly) .

## THE PLATE CIRCUIT

(a) PHYSICAL SITUATION

(b) CIRCUIT MODEL FOR A SINGLE DIODE

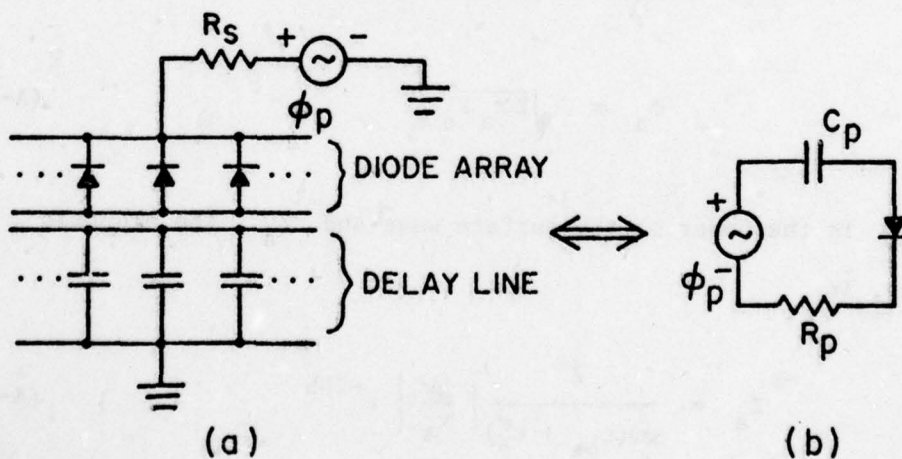


FIG. A-2 The Plate Circuit.

(a) Physical Situation and

(b) Circuit Model for a Single Diode.

surface wave velocity perturbation due to a shorted surface.

The coupling capacity  $C_a$  to an individual diode, normalized to a capacity per unit length, is given by the relation

$$C_a = \beta \epsilon_0 \left[ \frac{(\epsilon_0 + \epsilon_{pa})[1 + \tanh(\beta h)]}{\epsilon_0 + \epsilon_{pa} \tanh(\beta h)} \right] \left[ \frac{\sin \beta \frac{\delta}{2}}{\frac{\beta \delta}{2}} \right] \quad (A-3)$$

where  $\delta$  is the width of a diode and  $\ell$  the period spacing of the diodes and the last term takes account of the fact that the potential exciting a diode of width  $\delta$  is due to the total current flowing into it.  $\epsilon_0$  and  $\epsilon_{pa}$  are the dielectric constants of free space and the piezoelectric. For YZ -  $\text{LiNbO}_3$ ,  $\epsilon_{pa} = (\epsilon_{yy}\epsilon_{zz} - \epsilon_{yz}^2)^{1/2} = 50.2 \epsilon_0$ .

In reference 58 the semiconductor surface is modeled as a charge sheet a distance  $h$  above the piezoelectric. The negative capacitor of value  $-\epsilon_0 \beta$  is due to the admittance of the free space behind this charge sheet. We shall assume the impedance of the semiconductor surface to be that of any element of the diode array.

#### (b) The Plate Circuit

The plate circuit follows by inspection, as shown in Fig. (A-2).

$\phi_p$  is the externally applied plate potential. The capacitor  $C_p$  is due to the thickness of the piezoelectric, and is given by

$$C_p = \epsilon_p / d \quad (A-4)$$

where  $d$  is the piezoelectric substrate thickness and  $C_p$  the dielectric constant. For YZ- $\text{LiNbO}_3$ ,  $\epsilon_p = 70 \epsilon_0$ .  $R_p$  is the lumped resistance



due to both the series resistance of the source and the diode array substrate.

(c) Complete Circuit Model

The complete circuit model follows by noting that the plate and acoustic circuits are coupled only through the diode current. Thus, the circuit models of Figs. (A1) and (A2) are combined as shown in Fig. (A3). Here,  $I_a$  is the current through the acoustic circuit and  $I_p$  is the current through the plate circuit, with the diode current  $I_D = I_a + I_p$ .

For most cases, the diode depletion layer capacitor is large compared to  $-C_0 \beta$ . For device frequencies of the order of 100 MHz, time constants  $C_p R_p$  are short, and we may neglect  $R_p$ . These assumptions allow reduction of the circuit model (A3) to a form amenable for analysis. The diode current is written as

$$I_D = C_a \frac{d}{dt} (\phi_a - V_b) + C_p \frac{d}{dt} (\phi_p - V_D) = C \frac{d}{dt} (V_s - V_B) \quad (A-5)$$

with  $V_s = (C_a/C)\phi_a + (C_p/C)\phi_p$ , where  $C = C_a + C_p$ . Equation (A-5) is the I-V equation for the circuit of Fig. (A-4), the reduced equivalent circuit for the writing process.

### COMPLETE CIRCUIT MODEL

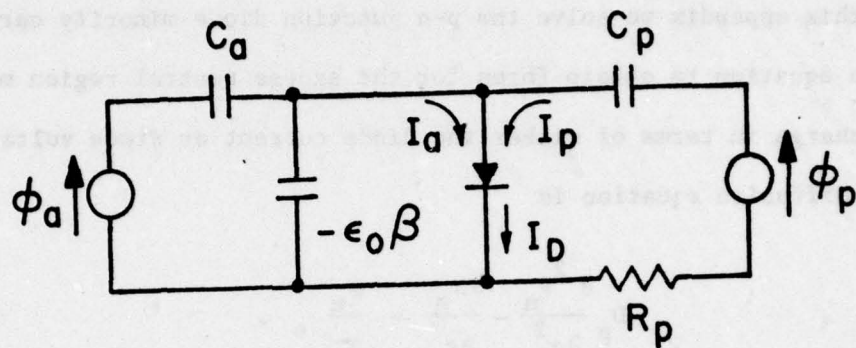


FIG. A-3. The complete device equivalent circuit model.

### REDUCED CIRCUIT MODEL FOR WRITING

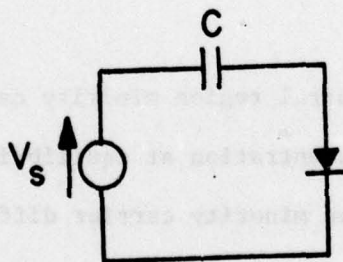


FIG. A-4. Reduced equivalent circuit model.

## APPENDIX B

### DIFFUSION EQUATION SOLUTIONS

In this appendix we solve the p-n junction diode minority carrier diffusion equation to obtain forms for the excess neutral region minority carrier charge in terms of either the diode current or diode voltage.

The diffusion equation is

$$D_p \frac{\partial^2 p_n}{\partial x^2} - \frac{\partial p_n}{\partial t} = \frac{p_n}{T_p}, \quad (B-1)$$

subject to the boundary conditions

$$p_n(0,t) = p_{n0} \left( e^{qV_D/kT} - 1 \right) \quad (B-2a)$$

$$p_n(x,0) = 0 \quad (B-2b)$$

$$p_n(\infty,t) = 0, \quad (B-2c)$$

where  $p(x,t)$  is the excess neutral region minority carrier charge,  $p_{n0}$  is the minority carrier concentration at equilibrium,  $V_D(t)$  is the junction voltage,  $D_p$  is the minority carrier diffusion constant, and  $T_p$  is the minority carrier lifetime.

The use of Laplace transforms allows the direct solution of (B1), yielding the result



$$p_n(x,t) = \frac{x}{2\sqrt{\pi D_p}} \int_0^t \frac{p_n(0,\tau) e^{-\frac{x^2}{4D_p(t-\tau)}} e^{-\frac{t-\tau}{\tau_p}}}{(t-\tau)^{3/2}} d\tau \quad (B-3)$$

The total minority carrier charge  $Q_p$  is

$$Q_p = \int_0^\infty p_n(x,t) dx = q\sqrt{D_p/\pi} \int_0^t \frac{p_n(0,\tau) e^{-(t-\tau)/\tau_p}}{(t-\tau)^{1/2}} d\tau \quad (B-4)$$

In most cases, these results will be applied for  $t \ll \tau_p$ . Assuming

$e^{qV_D/kT} \gg 1$ , (B-4) becomes

$$Q_p = qp_{n0} \sqrt{D_p/\pi} \int_0^t \frac{e^{qV_D(\tau)/kT}}{(t-\tau)^{1/2}} d\tau \quad (B-5)$$

Alternately, since the hole current is  $I_p(x) = -qD_p(dp/dx)$ ,

Laplace transforms may be used to find a solution to (B-1) of the form

$$p_n(x,t) = \frac{1}{q\sqrt{\pi D_p}} \int_0^t \frac{I_p(0,\tau) e^{-x^2/4D_p(t-\tau)}}{(t-\tau)^{1/2}} d\tau \quad (B-6)$$

Thus, since the total current is  $I(0,t) = I_p(0,t)$ , Eq. (B-6) takes the form

$$p_n(0,t) = \frac{1}{q\sqrt{\pi D_p}} \int_0^t \frac{I(0,\tau)}{(t-\tau)^{1/2}} d\tau \quad (B-7)$$

## APPENDIX C

### OUTPUT REDUCTION DUE TO PHASE MISMATCHING

It has been assumed that the propagation constant  $\beta + \gamma$  under the diode array is constant for both reading and writing. This is not strictly true, since the diode capacitance differs in each operation.

Consider, for example, acoustic-plate writing with a single plate pulse and acoustic-to-plate readout. As the writing surface propagates under the diode array, since no charge is stored, the capacity of each array element is the zero bias diode capacity  $C_{D0}$ . Due to stored charge, after writing the capacity of each diode array element has changed to  $C_D$ , with  $C_D \neq C_{D0}$ . The surface impedance of the charged and uncharged diode arrays differ; as a result, the propagation constants also differ.

Let us suppose the propagation constant for writing  $\beta + \gamma$  and for reading  $\beta + \gamma + \Delta\beta$ . The correlation integral over the full array length  $L$  takes the form

$$\int_{-L/2f}^{L/2f} e^{-j(\beta + \gamma)z} e^{j(\beta + \gamma + \Delta\beta)(z - v_a t)} dz \quad (C-1)$$

$$\sim \text{sinc} \frac{\Delta\beta L}{2f},$$

where  $v_a$  is the acoustic propagation velocity and  $f$  is a filling factor to account for the diodes covering less than the full diode array length.

We may explicitly calculate the change in propagation constant between writing and reading,  $\Delta\beta$ , from the Rayleigh wave amplifier theory of Kino and Reeder,<sup>58</sup> Eq. (21),

$$\frac{1}{Y^- - Y_0} = j \left[ \frac{M(\beta h)}{\beta \omega \epsilon_0} - \frac{\beta_a \omega Z_a(\beta h)}{\beta^2 - \beta_a^2} \right] \quad (C-2)$$

with

$$M(\beta h) = \frac{\epsilon_0 + \epsilon_{pa} \tanh \beta h}{(\epsilon_0 + \epsilon_{pa})(1 + \tanh \beta)} \quad , \quad (C-3)$$

where  $\beta$  and  $\beta_a$  are the perturbed and unperturbed acoustic surface wave propagation constants, respectively,  $Y^-$  is the semiconductor admittance,  $Y_0 = j\omega\epsilon_0\beta$  is the admittance of free space, and all other quantities have been defined previously.

We set

$$Y^- = j\omega C_D \gg Y_0 \quad . \quad (C-4)$$

Assuming small perturbations, (C-2) is rearranged to give

$$\frac{(\beta - \beta_a)}{\beta} = \frac{\omega \omega Z_a}{2\beta(1/C_a + 1/C_D)} \quad , \quad (C-5)$$

where we have set  $C_a = \epsilon_0 / M(\beta h)$ , essentially as in Eq. (A-3).



It is noted that when  $C_a \ll C_D$ , as is usually the case,  $\beta - \beta_a = \gamma$ , in agreement with Eq. (52).

We suppose a diode capacitance of  $C_{D0}$  for writing and  $C_D$  for reading, with  $C_D < C_{D0}$ . Then, from Eq. (C-5), the difference in propagation constant between writing and reading,  $\Delta\beta$ , is given by

$$\Delta\beta = \gamma \left[ \frac{1}{1 + (C_a/C_{D0})} - \frac{1}{1 + (C_a/C_D)} \right] . \quad (C-6)$$

We have experimentally observed the phase shift due to  $\Delta\beta$ . The device described in Table II, column 1, was pulsed with a 230 V, 5 nsec plate pulse and the change in propagation delay under the diode array was measured. Figure C-1 shows the observed 3.5 nsec delay of the 108 MHz rf signal that has propagated under the 5  $\mu$ sec long diode array. This delay is consistent with a factor  $f$  of 1.26.

The  $\text{sinc}^2(\Delta\beta L/2f)$  output power reduction due to phase mismatching is plotted as a function of plate pulse amplitude  $V_{p0}$  in Fig. C-1. Also shown in the experimentally observed drop in output power with respect to the plate pulse amplitude  $V_{p0}$ . This is copied directly from Fig. 6. Adding the experimentally observed increase in propagation loss with respect to  $V_{p0}$  accounts for most of the measured drop in output power with respect to the plate pulse amplitude  $V_{p0}$ .

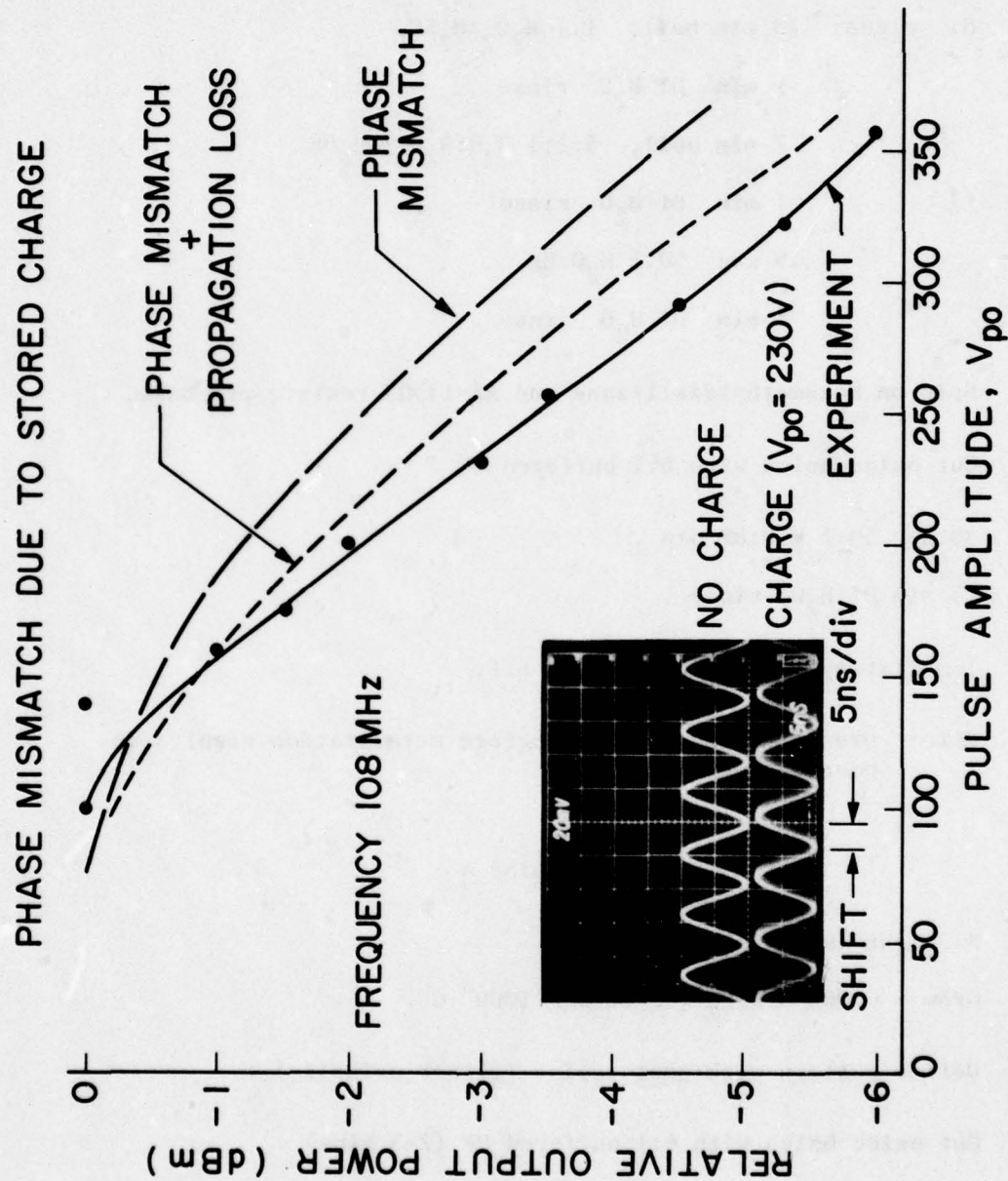


FIG. C-1 Output Reduction due to the Phase Mismatch of the Writing and Reading Signals, Experiment and Theory.

## APPENDIX D

### PROCESSING OF DIODE ARRAYS

#### Al/Si , Au/Si Schottky Diodes

1. Si clean: 10 min boil, 1:1  $H_2O_2:H_2SO_4$   
1 min DI  $H_2O$  rinse  
7 min boil, 5:1:1  $H_2O:H_2O_2:NH_4OH$   
1 min DI  $H_2O$  rinse  
45 sec 50:1  $H_2O:HF$   
5 min DI  $H_2O$  rinse .
2. Spin on Hexamethyldisilazane and AZ-1350J resist, pre-bake.
3. Cut oxide holes with 6:1 buffered HF .
4. 30 sec 50:1  $H_2O:HF$  dip ,  
5 min DI  $H_2O$  rinse .
5. Immediately metallize and lift off.

Note: presputtering to clean before metalization results in poor diodes.

#### PtSi Schottky Diodes

1. Si clean (see Al/Si process) .
2. Grow  $\sim 1000 \text{ \AA}$   $SiO_2$  , 5-12-5 @  $1000^\circ \text{ C}$  .
3. Define pattern with photoresist (either polarity) .
4. Cut oxide holes with 6:1 buffered HF (2-3 mins) .
5. Remove excess photoresist with a 5-10 min  $H_2SO_4$  dip, followed by a Si clean.



6. Coat with 500 Å Pt in E-beam system, immediately after 50:1 HF dip and 5 min DI H<sub>2</sub>O rinse to remove residual oxide.
7. Anneal for 5 min at 650° C in Ar or N<sub>2</sub> flow .
8. Etch off excess Pt in hot Aqua Regia (3HCL:1HNO<sub>3</sub>) for 5 mins.

#### Planar p<sup>+</sup>n Diodes

1. Si clean (see step 1, Al/Si diodes) .
2. Grow 2000 Å SiO<sub>2</sub> , 10-30-10 @ 1000° C .
3. Spin on negative resist, pre-bake.
4. Expose, develop, post-bake.
5. Etch front of arrays only in 6:1 buffered HF to make oxide cuts.
6. Soak in H<sub>2</sub>SO<sub>4</sub> 10 mins, followed by clean.
7. Boron predep ~ 20 mins @ 1000° C .
8. Drive in, 5-40-5 @ 925° C .

#### V-Groove Diodes

1. Si clean (see step 1, Al/Si diodes) .
2. Grow 2000 Å SiO<sub>2</sub> , 10-30-10 @ 1000° C .
3. Strip oxide on front of wafer in 6:1 buffered HF .
4. Boron predep, 20 mins @ 1000° C .
5. Drive in, 5-30-5 @ 1000° C . Grows ~ 2000 Å SiO<sub>2</sub> .
6. Define photoresist pattern and remove SiO<sub>2</sub> with 6:1 buffered HF everywhere except over diodes.

7. V-groove etch,  $2\frac{1}{2}$  mins in boiling 33% by weight KOH in  $H_2O$  .
8. A  $1000 \text{ \AA}$   $SiO_2$  passivation layer can be grown, 5-30-5 @  $925^\circ C$  .

#### Overlay Diodes (Doped Polysilicon)

1. Si clean (see step 1, Al/Si diodes).
2. Grow  $1000 \text{ \AA}$   $SiO_2$  , 5-12-5 @  $1000^\circ C$  .
3. Coat with negative resist and define diode wells.
4. Etch wells with 6:1 buffered HF .
5. Si clean.
6. Boron predep @  $1000^\circ C$  , 20 mins .
7. Drive in, 20 mins @  $925^\circ C$  in  $N_2$  ambient.
8. Si clean.
9. 2 mins etch in 50:1 HF to remove oxide over diodes.
10. Grow  $\sim 5000 \text{ \AA}$  Polysilicon .
11. Boron predep,  $950^\circ C$  for 15 mins .
12. Drive in, 5-20-5 @  $925^\circ C$  .
13. Coat with negative photoresist and define mask for overlays.
14. Etch  $\sim 3$  mins in 6:1 buffered HF .
15. Etch polysilicon  $\sim 1$  min in 50:1  $HNO_3:NH_4F$  .

## APPENDIX E

### ZnO/Si SCHOTTKY DIODE CORRELATOR

Two ZnO Silicon storage correlators were fabricated. These devices were essentially identical to those developed by B. T. Khuri-Yakub, except that a PtSi diode array was situated between the ZnO and Si, as shown in Fig. E-1.

The array had a period of  $6\text{ }\mu\text{m}$ , with  $3\text{ }\mu\text{m} \times 1\text{ mm}$  bar diodes crossing the full beam width. A  $1000\text{ }\text{\AA}$  sputtered  $\text{SiO}_2$  film covered the surface. A  $1.6\text{ }\mu\text{m}$  ZnO layer was then sputtered on the  $\text{SiO}_2$ . Two 10 finger pair, 125 MHz transducers were at each end of the line.

The best device had a 28 dB 2 port loss and a convolution efficiency of  $F_t = -80\text{ dBm}$ . A transducer failed before storage experiments could be attempted, and the second line had a 2 port loss of  $-48\text{ dB}$ , too high for good storage correlation operation.

Nevertheless, a convolution was observed, and this was affected by charge storage, as seen in Fig. E-1(a). The observed 3 dB drop in the convoltuon was due to a  $5\text{ }\mu\text{sec}$ , 12 V plate pulse. The 1/2 height storage time is  $\sim 10\text{ msec}$ . This corresponds to a reverse current about one order of magnitude worse than that observed for the discrete PtSi diodes described in Section 2(b) of Chapter III. This may be due to the small diode dimensions, which cause increased edge leakage.

Figures E-2(b), (c) show that the device is light sensitive and that there is no hysteresis, even after exposure to strong light. Hysteresis, thought to be due to charge trapping in the ZnO, has made the ZnO/Si convolver useless for most imaging applications. The present structure's immunity to this problem may be due to the relatively high



# ZnO/Si CONVOLVER WITH SCHOTTKY DIODE STORAGE

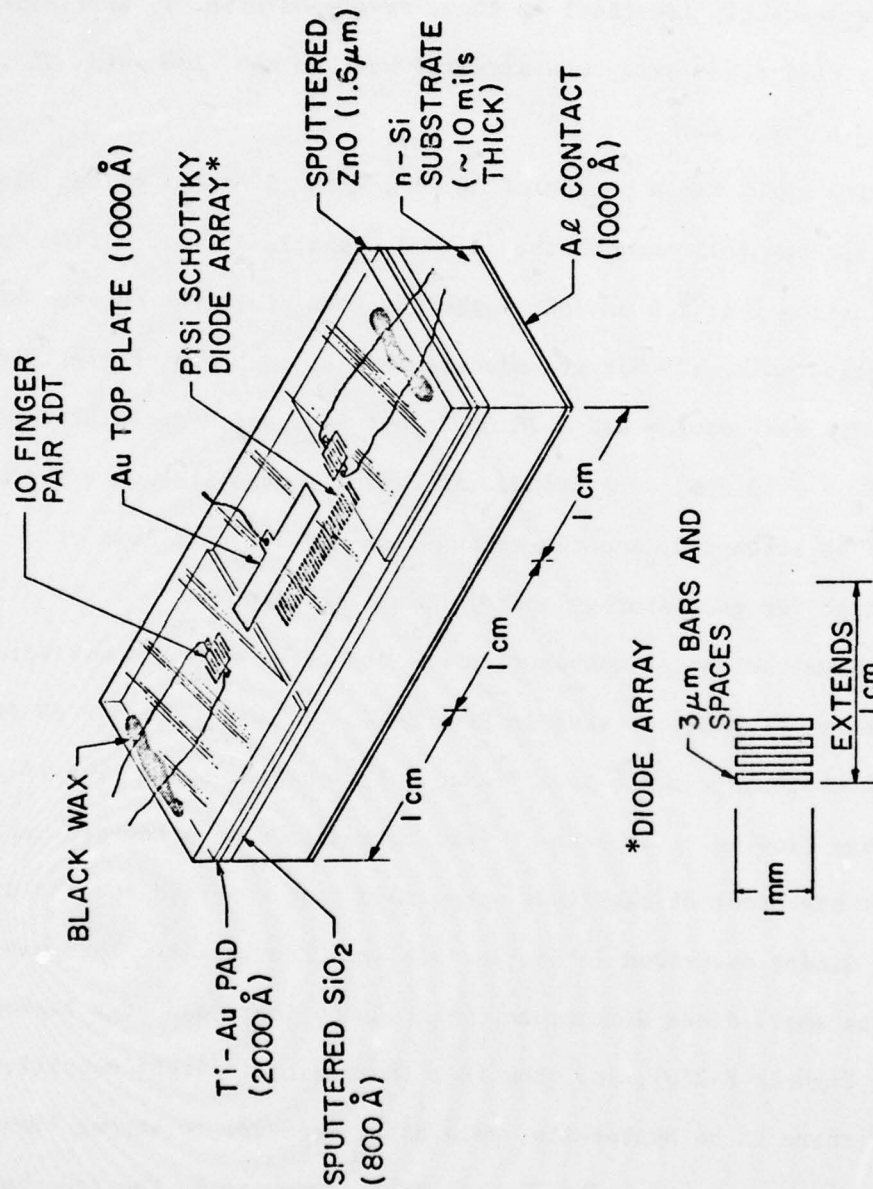
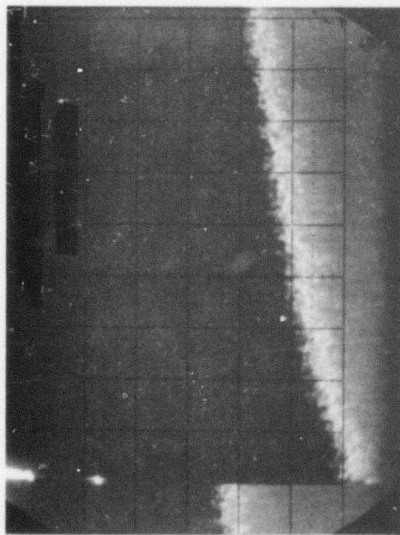
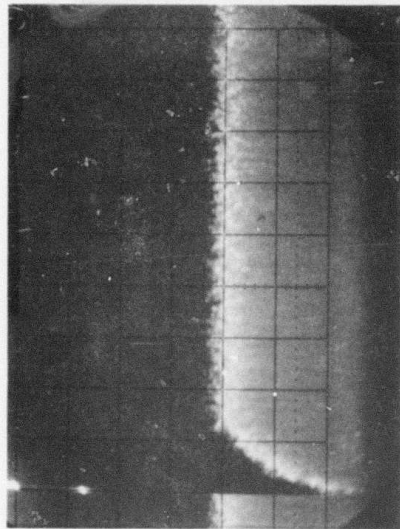


FIG. E-1 The ZnO/Si Convolver with Schottky Diode Storage.

No Light

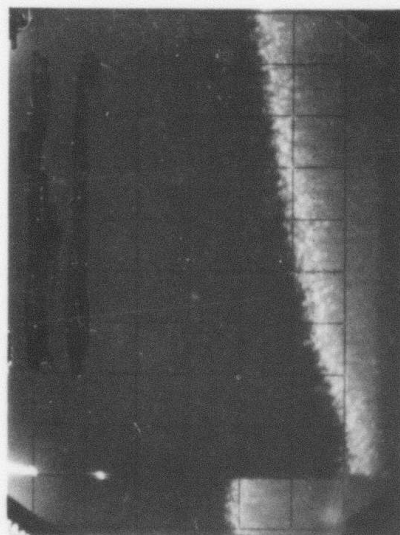


Light



Light Removed

(light for 15 seconds)



2 msec

FIG. E-2. Schottky Barrier Diode  
ZnO Convolver.

conductivity of sputtered  $\text{SiO}_2$ , as opposed to thermally grown  $\text{SiO}_2$ . The sputtered  $\text{SiO}_2$  allows a small but significant current to flow from the Schottky diodes to the  $\text{ZnO}$ , thereby discharging traps located near the  $\text{ZnO-SiO}_2$  interface.



## APPENDIX F

### THE PHASE CODED TRANSDUCER

The phase coded transducer was discussed in Section 3(b)1 of Chapter III and shown in Fig. III-7. Because each finger has a  $\pi$  phase shift over its length, the potential due to a normally incident plane surface wave will cancel over the finger length; such a transducer will only be sensitive to an incident plane surface wave broken into two halves, with the upper and lower halves shifted in phase by  $\pi$  with respect to each other. This is done in practice by breaking the diode array into two parallel channels and employing coded transducers at both ends of the device, as seen in Fig. III-7. Spurious signals generated during reading will not be coded so that a device with phase coded transducers yields improve S/N .

The figure phase shift of  $\lambda/2$  is chosen to maximize S/N normally incident plane waves. A problem with this scheme is that plane waves incident at angles off the normal may not be effectively rejected. To find the improvement in S/N with phase coded transducers in this case, we calculate the amplitude response for arbitrary angles of incident surface waves.

Consider a transducer with  $N$  fingers, each of length  $L$  and width  $W$  . A shift of distance  $D$  is introduced in the middle of each finger ( $D = 0$  for straight fingers,  $\lambda/2$  for coded fingers). A plane wave propagation vector  $\beta$  is incident at an angle  $\theta$  with respect to the  $z$  axis, which is normal to the fingers. We assume an incident wave potential of the form

$$\psi_1 = A e^{j[\omega t - \beta(y \sin \theta + z \cos \theta)]} \quad (F-1)$$

where A is constant amplitude.

Assuming the fingers to be perfectly conducting, we integrate the incident potential over the area of a single finger to obtain the variation of the amplitude response with respect to angle. This yields a variation of the form

$$\psi_s \sim \left[ \frac{\sin \frac{\beta L \sin \theta}{2}}{\frac{\beta L \sin \theta}{2}} \right] \left[ \frac{\sin \frac{\beta w \cos \theta}{2}}{\frac{\beta w \cos \theta}{2}} \right] \quad (F-2)$$

for the straight finger case ( $D = 0$ ), and a variation of the form

$$\psi_p \sim \frac{\cos \left[ \frac{\beta L \sin \theta}{4} + (\pi/2) \cos \theta \right]}{\cos \left( \frac{\beta L \sin \theta}{4} \right)} \times \psi_s \quad (F-3)$$

for the phased finger case ( $D = \lambda/2$ ). These responses are plotted in Fig. E-1 for a 100 MHz Rayleigh wave on YZ -  $\text{LiNbO}_3$ , with a finger length of 1 mm and width of 8  $\mu\text{m}$ .

For a transducer with N finger pairs, the amplitude responses  $\psi_s$  and  $\psi_p$  are multiplied by a factor

$$\frac{1 - e^{-j2N\pi \cos \theta}}{1 - e^{j2\pi \cos \theta}}$$

whose magnitude is  $\left| \frac{\sin(N\pi \cos \theta)}{\sin(\pi \cos \theta)} \right|$ . For  $\theta$  small, this becomes  $|\sin(N\pi \theta^2/2)/(\pi \theta^2/2)|$ . For small  $\theta$  this is essentially independent of

angle. Thus, the response shown in Fig. F-1 is valid for any number of finger pairs  $N$ .

The phase coded transducer indeed has a zero amplitude response for normally incident plane waves, while the straight finger transducer has a peak response. However, slightly off normal (between  $0.9$  and  $2.7^\circ$  for the case shown in Fig. F-1, the phase coded transducer has a higher response to an incident plane wave. This arises because the phase coded transducer fingers are effectively only half as long as the straight finger transducer fingers. The straight finger transducer has twice as many peaks and nulls in its angular response. Consequently, over a significant range of angles, the straight fingered transducer is less sensitive to incident plane waves. We see that the coded finger transducers offer a significant improvement in S/N only when the spurious surface waves are nearly normally incident.



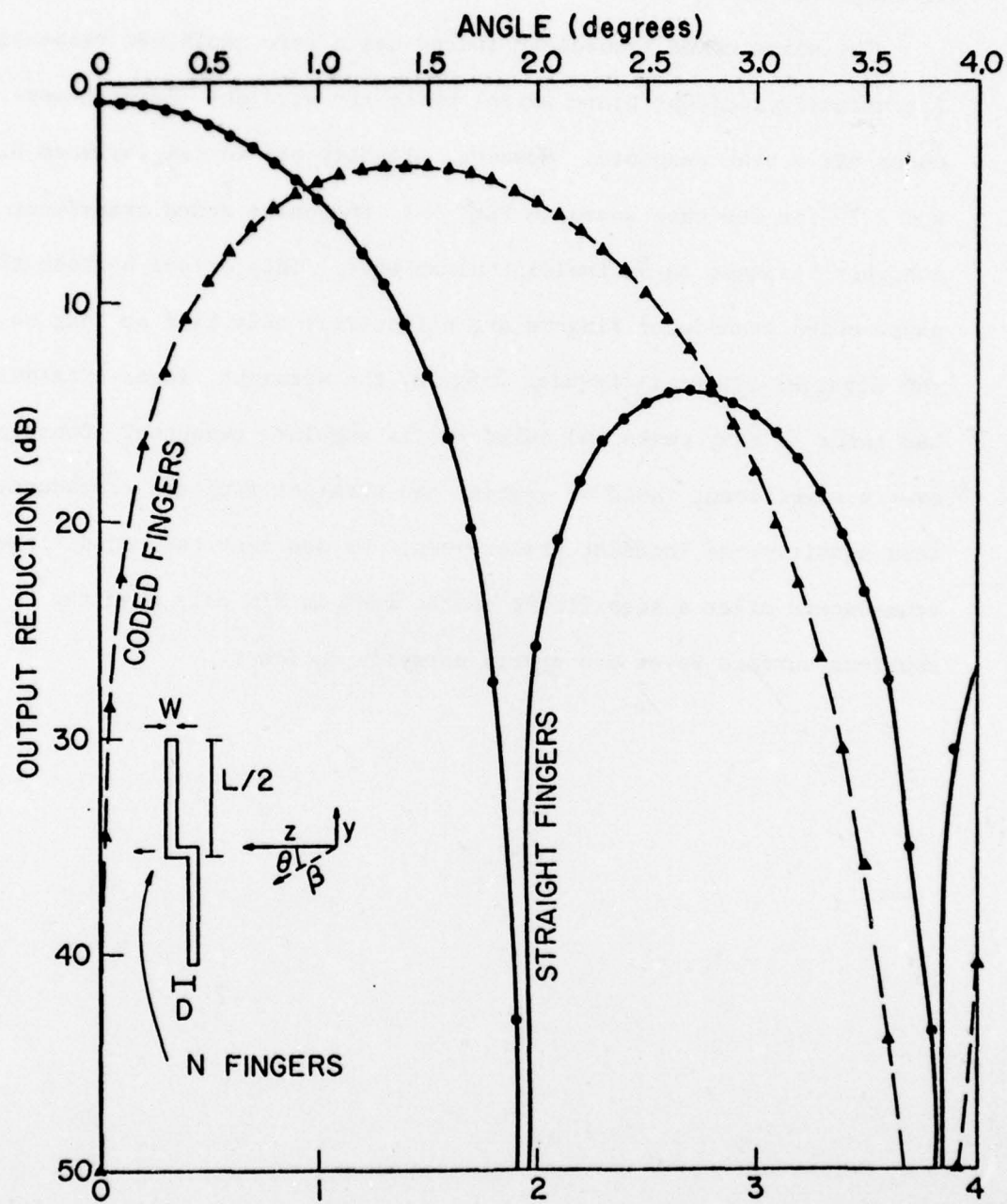


FIG. F-1. The phase coded transducer output vs angle of incidence.

# REFERENCES

1. A. G. Bert, B. Epsztein, G. Kantorowicz, "Charge Storage of Acoustic RF Signals," Appl. Phys. Letters 21, 50-52 (1972).
2. A. G. Bert, B. Epsztein, G. Kantorowicz, "Signal Processing by Electron Beam Interaction with Piezoelectric Surface Waves," IIII Trans. Sonics Ultras. SU-20, 173-181 (1973).
3. G. Kantorowicz French Patent Application 73.45234 (1973) and 74.19172 (1974).
4. A. Bers, J. H. Cafarella, "Surface State Memory in Acoustoelectric Correlator," Appl. Phys. Letters 25, 178-180 (1974).
5. A. Bers, J. H. Cafarella, "Surface Wave Correlator-Convolver with Memory," 1974 IEEE Ultras. Symp. Proc. 778 (1974).
6. H. Hayakawa, G. S. Kino, "Storage of Acoustic Signals in Surface States in Silicon," Appl. Phys. Letters 25, 178-180 (1974).
7. K. A. Ingebrigtsen, R. A. Cohen, R. W. Mountain, "A Schottky Diode Acoustic Memory and Correlation," Appl. Phys. Letters 26, 596-598 (1975).
8. A. Bert, G. Kantorowicz, "Phase and Amplitude Storage of an Acoustic Signal in a Schottky Diode Correlator," Elec. Letters 11, 523 (1975).
9. C. Maerfeld, Ph. Defranould, "A Surface Wave Memory Device Using pn Diodes," 1975 IEEE Ultras. Symp. Proc. 209 (1975).
10. C. Maerfeld, Ph. Defranould, P. Tournois, "Acoustic Storage and Processing Device Using pn Diodes," Appl. Phys. Letters 27, 11, 577-578 (1975).
11. K. A. Ingebrigtsen, E. Stern, "Coherent Integration and Correlation in a Modified Acoustoelectric Memory Correlator," Appl. Phys. Letters 27, 170-172 (1975).
12. K. A. Ingebrigtsen, "Simultaneous Storage of Spatially Orthogonal Acoustic Beam in a Schottky Diode Memory Correlator," Elec. Letters 11, 585-586 (1975).
13. K. A. Ingebrigtsen, "The Schottky Diode Acoustoelectric Memory and Correlator. A Novel Programmable Signal Processor," Proc. IEEE 64, 764-769 (1976).
14. P. G. Borden, G. S. Kino, "Correlation with the Storage Convolver," Appl. Phys. Letters 29, 527-529 (1976).

15. P. Borden, G. S. Kino, R. Joly, "Correlation with the Storage Correlator," 1976 IEEE Ultras. Symp. Proc., 348-351 (1976).
16. P. G. Borden, G. S. Kino, "Input Correlation with the Storage Correlator," Elect. Letters 13, 470-471 (1977).
17. H. C. Tuan, G. S. Kino, "Large-Time-Bandwidth-Product Correlation and Holographic Storage with an SAW Storage Correlator, Elect. Letters 13, 709-710 (1977).
18. Ph. Defranould, H. Gautier, C. Maerfeld, P. Tournois, "PN Diode Memory Correlator," 1976 IEEE Ultras. Symp. Proc., 336-347 (1976).
19. W. C. Wang, K. C. Whang, L. S. Rosenheck, "Optical Imaging and Memory Using a Silicon Diode Storage Correlator," 1976 IEEE Ultras. Symp. Proc., 352-356 (1976).
20. H. Gautier, Internal Report DASM 76/06/099 HG, Thomson-CSF (Feb. 1976).
21. W. C. Wang, "Physical processes of SAW-Schottky Diode Memory Correlator," Elec. Letters 12, 4, 105-106 (1976).
22. P. G. Borden, G. S. Kino, "The Charging Process in the Acoustic Surface Wave p-n Diode Storage Correlator," Appl. Phys. Letters 31, 488-490 (1977).
23. S. Takada, K. Hoh, H. Hayakawa, Y. Tokumaru, "Surface Wave Memory Correlator Using Light Pulse from a GaAs Laser Diode," 1976 IEEE Ultras. Symp. Proc., 361-364 (1976).
24. P. Borden, B. T. Khuri-Yakub, H. C. Tuan, G. S. Kino, "ZnO Convolver Development," 1976 IEEE Ultras. Symp. Proc., 171-173 (1976).
25. H. C. Tuan, G. S. Kino, "A Monolithic ZnO/Si Storage Correlator," Appl. Phys. Letters, to be published.
26. Ph. Defranould, H. Gautier, C. Maerfeld, "High Sensitivity Acoustically Scanned Optical Imaging Device Using Charge Storage Effect," Appl. Phys. Letters 29, 79-81 (1976).
27. R. Joly, "Design of a Convolver for Optical Imaging," Ph.D. Dissertation, Stanford University, Stanford, California (May 1976).
28. H. Gautier, "Acoustic Wave Semiconductor Convolver Applied to Electrical and Optical Signal Processing," Ph.D. Dissertation, Stanford University, Stanford, California (June 1975).



29. B. T. Khuri-Yakub, "The Application of Zinc Oxide on Silicon to Surface Acoustic Wave Devices," Ph.D. Dissertation, Stanford University, Stanford, California (December 1975).
30. T. W. Grudowski, "Active Acoustic Waves and Electrons in Gallium Arsenide," Ph.D. Dissertation, Stanford University, Stanford, California (May 1975).
31. N. J. Moll, O. W. Otto, C. F. Quate, J. De Physique 33, Colloque C-6, Supplement, 231-234 (November-December, 1972).
32. O. W. Otto and N. J. Moll, Elec. Letters 8, 600-602 (1972).
33. C. F. Quate and R. B. Thompson, Appl. Phys. Letters 16, 494-496 (1970).
34. G. S. Kino and H. Gautier, J. Appl. Phys. 44, 5219-5221 (December, 1973).
35. T. Grudkowski and C. F. Quate, Appl. Phys. Letters 25, 99-101 (1974).
36. B. T. Khuri-Yakub and G. S. Kino, Appl. Phys. Letters 25, 188-190 (1974).
37. M. V. Luukkala and G. S. Kino, Appl. Phys. Letters 18, 393-394 (1971).
38. H. Gautier, G. S. Kino, and H. J. Shaw, "Acoustic Transform Techniques Applied to Optical Imaging," 1974 IEEE Ultrasonics Symposium Proceedings, 99-103 (1974).
39. S. M. Sze, Physics of Semiconductor Devices (Wiley-Interscience, 1969).
40. J. L. Moll, Physics of Semiconductors (McGraw-Hill, 1964).
41. A. S. Grove, Physics and Technology of Semiconductor Devices (Wiley, 1967).
42. A. van der Ziel, Solid State Physical Electronics (Prentice-Hall, 1976).
43. S. K. Ghandhi, The Theory and Practice of Microelectronics (Wiley, 1968).
44. B. A. Auld, Acoustic Fields and Waves in Solids (Wiley, 1973).
45. A. W. Rihaczek, Principles of High Resolution Radar (McGraw-Hill, 1969).
46. R. Bracewell, The Fourier Transform and Its Applications (Mc-Graw-Hill, 1965).
47. D. Corl, Private Communication.
48. B. Auld, U. S. Patent 4,021,657 (May 3, 1977)..

49. B. J. Darby and J. D. Maines, "The Tapped Delay Line Active Correlator: A Neglected SAW Device," 1975 IEEE Ultras. Symp. Proc., 193-196 (1976).
50. C. Maerfield, Ph. Defranould, "A Surface Wave Memory Device Using pn Diodes," 1975 IEEE Ultras. Symp. Proc., 209 (1975).
51. R. Ralston, et.al., IEEE Device Research Conference (1977).
52. E. Stein, Invited Paper, 1975 IEEE Ultrasonics Symposium, (Unpublished).
53. F. J. Leonberger, J. H. Cafarella, R. W. Ralston, E. Stern, A. L. McWhorter, "Acoustoelectrically Scanned Gap-Coupled Si Diode Array/LiNbO<sub>3</sub> Imaging Devices," 1977 IEEE Ultrasonics Symposium (1977).
54. K. Shibayama, K. Yamanouchi, H. Sato and T. Meguro, "Optimum Cut for Rotated Y-Cut LiNbO<sub>3</sub> Crystal Used as the Substrate of Acoustic-Surface-Wave Filters," Proc. IEEE, 64, 595-597 (1976).
55. R. S. Wagers, "Spurious Acoustic Responses in SAW Devices," Proc. IEEE, 64, 699-702 (1976).
56. P. H. Carr, T. E. Fenstermacher, 1 Lt. J. M. Silva, W. J. Kearns, M. R. Stiglitz, "SAW Delay Line with all Spurious 70 dB Down." 1976 IEEE Ultrasonics Symposium Proceedings, 459-61 (1976).
57. B. A. Auld and G. S. Kino, "A Normal Mode Theory for Acoustic Surface Waves and its Application to the Interdigital Transducer," IEEE Trans. Elect. Dev. ED-18, 10, 898-908 (1971).
58. T. M. Reeder and G. S. Kino, "A Normal Mode Theory for the Rayleigh Wave Amplifier," IEEE Trans. Elect. Dev. ED-18, 10, 909-920 (1971).
59. P. M. Morse and H. Feschbach, Methods of Theoretical Physics, McGraw-Hill, p. 557 (1953).
60. R. W. Ralston, D. H. Hurlburt, F. J. Leonberger, J. M. Cafarella and E. Stern, "A New Signal-Processing Device, the Integrating Correlator," IEEE Sonics and Ultrasonics Symposium Proceedings, 623-628 (1977).
61. J. H. Cafarella, private communication.
62. O. Menager and B. Desormiere, "Surface Acoustic Wave Tapped Correlator Using Time Integration," Appl. Phys. Letters 27, 1-2 (1975).

63. K. L. Davis, "ZnO/Si Programmable Tapped Correlator, IEEE Sonics and Ultrasonics Symposium Proceedings, 456-458, (1976).
64. T. W. Grudkowski, "A Programmable Nondegenerate GaAs Convolver," IEEE Sonics and Ultrasonics Symposium (1976), Paper not submitted.
65. T. W. Grudkowski and T. M. Reeder, "Experiments with Large Time-Bandwidth, Programmable PSK Diode-Correlators, IEEE Sonics and Ultrasonics Symposium (1976), Paper not submitted.
66. T. M. Reith, "Aging Effects in Si-doped Al Schottky Barrier Diodes," Appl. Phys. Letters 28, 152-154 (1976).
67. R. J. Schwartz, S. D. Gaalema and R. L. Gunshor, "A Surface Wave Interaction Charge Coupled Device, IEEE Sonics and Ultrasonics Symposium Proceedings, 197 (1976).
68. D. M. Bloom and G. C. Bjorklund, "Conjugate Wave-Front Generation and Image Reconstruction by Four-Wave Mixing," Appl. Phys. Letters 31, 592-4 (1977).



DISTRIBUTION LIST

<u>Addressee</u>	<u>Number of Copies</u>
Director Advanced Research Projects Agency 1400 Wilson Boulevard Arlington, VA 22209 Attention: Program Management	1
Scientific Officer	3
Administrative Contracting Officer	1
Director Naval Research Laboratory Attention: Code 2627 Washington, DC 20375	6
Office of Naval Research Department of the Navy Arlington, VA 22217 Attention: Code 102IP	6
Defense Documentation Center Bldg. 5 Cameron Station Alexandria, VA 22314	12
Office of Naval Research Branch Office 1030 East Green Street Pasadena, CA 91101	1
Naval Research Laboratory Code 5250 Washington, DC 20375	1
RADC (ETEM) Attn: Dr. P. Carr Hanscom AFB, MA 01731	1
AGED ODDR&E 9th Floor 201 Varick Street New York, NY 10014	1
Dr. R. Damon Director, Applied Physics Lab. Sperry Research Center Sudbury, MA 01776	1